HIGH-SPEED HIGH-RESOLUTION VECTOR FIELD MEASUREMENTS AND ANALYSIS OF BOUNDARY LAYER FLOWS IN AN INTERNAL COMBUSTION ENGINE

by

Ali Alharbi

A dissertation submitted in partial fulfillment
of the requirements for the degree of
Doctor of Philosophy
(Mechanical Engineering)
in The University of Michigan
2010

Doctoral Committee:

Professor Volker Sick, Chair
Professor Steven L. Ceccio
Associate Professor Luis P. Bernal
Visiting Research Scientist David L. Reuss

DEDICATION

To my lovely family

ACKNOWLEDGEMENTS

This work would not have been possible without the help and support from a number of people. First I would like to thank my advisor, Professor Volker Sick, for introducing me to the fascinating world of experimental fluid mechanics. His guidance and support throughout my work have been indefinite, and his knowledge has been a great source of inspiration.

I would like to thank my committee members, Professor Steven Ceccio, Professor Luis Bernal, and Dr. David Reuss for being part of this work. It is an honor having you in my Doctoral committee. I would like to acknowledge Professor Matthias Ihme and Professor David Dowling for their valuable discussions and recommendations which added depth to my work and helped broaden my knowledge in turbulence.

I would like to thank my former and current colleagues from the quantitative laser diagnostics lab for their help with experiments and for being such a wonderful friends, Dr. James Smith, Western Michigan University Assistant Professor Claudia Fajardo, Dr. Rui Zhang, Brian Peterson, Mike Cundy, Kevin Peterson, Mike Mosburger, Preeti Abraham, Louise Lu, Omar Almagri, Hao Chen, Mike Litsey, Jessamyn Margoni, Mike Chin, Daniel Rimmelspacher, Patrick Nohe, and Jason Moscetti.

I would like to thank my mother and father for their unconditional love and support throughout the years, my two lovely sisters and my brothers for being so kind. I would like to thank my wife for her sacrifices. This is the second time you set your career aside so we can be together. I know if you had to, you would do this million times again.

Last, I would like to thank the Public Authority for Applied Education and Training (PAAET) for sponsoring me the past five years. And I would like to acknowledge my PAAET advisor at Kuwait embassy, Ms. Shoghig Sahakyan, for her support throughout my entire study period.

TABLE OF CONTENTS

LIST OF FIGURES

LIST OF TABLES

ABSTRACT

Heat transfer properties vary locally and temporally in internal combustion engines due to variations in the boundary layer flow. In order to characterize the dynamics in the boundary layer, crank-angle resolved high-speed Micro Particle Image Velocimetry (μPIV) and Particle Tracking Velocimetry (PTV) have been used for near-wall velocity measurements in a spark-ignition direct-injection single cylinder engine. A 527 nm dual cavity green Nd:YLF laser was used for velocity measurements near the cylinder head wall between the intake and exhaust valves in the tumble mean flow plane parallel to the cylinder axis. A long distance microscope was used to obtain a spatial resolution of 45 µm. Flow fields were determined from 180 to 490 CAD in the compression and expansion strokes. The accomplished experiment represents first-time two-dimensional and a time history velocity measurements in a boundary layer flow in internal combustion engine. The data shows significant variation in the flow during the compression and expansion strokes and from cycle to cycle. Flow deceleration was observed during the end of the compression which continued during the expansion stroke until 400 CAD when the flow direction reverses. Submillimeter sized vortical structures were observed within the boundary layer over extended periods of time. Inner length and velocity scales were determined from the experimental results and were used to construct the law of the wall velocity distribution in the viscous sublayer and in the log law region. Experimental velocity profiles show agreement with the law of the wall in the viscous

sublayer but they exhibit an early departure in the log law region due to the unique nature of the tumbling free stream flow in internal combustion engines. Reynolds stresses in the plane flow along with turbulent kinetic energy production and dissipation were determined.

CHAPTER 1

INTRODUCTION

In-cylinder convection heat transfer from the gas side to the walls of the combustion chamber of an IC engine plays an important role on the performance and design of engines. Since the 1920's, many experiments have been conducted producing a handful empirical correlations for the heat transfer coefficient. Many of these correlations once were widely used and then became obsolete with the introduction of other correlations that utilized a wider range of data and different approaches leading to more universal formulas. Almost all of the proposed correlations for the past eighty years give spatially averaged heat transfer coefficient; thus lack detailed description of local convection heat transfer. Another issue with the spatially averaged correlations is that they are experimentally determined based on heat flux and wall temperature measurements in single point on the combustion chamber. As will be seen on the literature review on the instantaneous local correlation section that wall temperature; and therefore heat flux, varies spatially at any instant during the cycle. Energy balance methods to determine the spatially averaged heat transfer coefficient should remedy this issue; however, it still does not give detailed local description of heat transfer.

With the vast developments of computing capabilities, multidimensional numerical simulations offer a great alternative that provides a comprehensive analysis of fluid flow and heat transfer process. However; the flow being unsteady and turbulent, modeling of the turbulent terms of the governing transport equations remains a challenging task. Experimental work is needed to provide modelers with the data to validate and improve current modeling methods. After detailed study of the status of heat transfer in IC engines, Borman and Nishiwaki (1) concluded that the fundamental problem in modeling is the lack of detailed data regarding the gas side velocity and temperature distribution, and vital questions concerning the turbulent boundary layer model need to be explored experimentally. They recommend that a fundamental work on convective heat transfer is needed applying modern optical methods to determine velocity, temperature, and turbulence profiles. Even though their study was carried out twenty three years ago, not much has been done to fulfill the recommended experimental work leaving the fundamental problem of convective heat transfer problem in internal combustion engines unaddressed and requiring more attention.

A number of in cylinder flow measurements have been conducted using methods like hot wire anemometry, laser Doppler velocimetry (LDV), and particle image velocimetry (PIV) studying instantaneous and bulk velocities, turbulence intensities, vorticity and strain rates, cycle-to-cycle variability, and mean flows, i.e. swirl and tumble. However, only few attempts have been made to measure near-wall velocity distribution. LDV was the only tool applied to those studies giving high temporal resolutions at one point in the flow. These experiments often used special designs for the cylinder head in

order to get closer to the wall. When a more realistic simple flat head was under study, the closest distance to the engine head was approximately four times the one for the specially designed cylinder head.

The purpose of the current research is to apply a more versatile method to resolve near-wall velocities in actual production engine design. PIV was applied to measure near-wall velocities at the cylinder head. Based on preliminary experiments, higher magnifications were required to zoom in the boundary layer region. A long distance microscope was used to resolve the hydrodynamic boundary layer near the cylinder head wall. Prior to that high resolution PIV experiment, a low resolution PIV experiment was conducted to obtain an overview of the flow behavior near the cylinder head wall in the region between the spark plug and the fuel injector of the optical spark ignited direct injection engine. Low seeding count in the high resolution μPIV experiment was rectified by applying a hybrid algorithm combining PIV as a "predictor" of the flow field and particle tracking velocimetry (PTV) as a "corrector" of the flow field by tracking individual particles. The PTV algorithm also helped increase the resolution of the measurement and reduce near wall bias. Another challenge was the drawback of conducting a PIV experiment near a wall, which is glare caused by laser reflection off the wall surface that may exceed the Mie scattering signal of the seeding particles. A flat black paint was used on the surface of interest, which helped reducing the intensity of the reflection drastically.

In this document, heat transfer in IC engines is discussed in Chapter two. It covers the importance and uniqueness of in cylinder heat transfer, cycle description of heat transfer, heat transfer mechanisms with an emphasis on convection heat transfer. It ends with a literature review on global and zonal heat transfer coefficient correlations, and one dimensional and three dimensional models. Chapter three goes over the major mean flow induced motions, i.e. swirl and tumble, mean velocity and turbulence characteristics, mean flow equations including boundary layer approximations and the universal law of the wall, experimental flow diagnostic techniques and their applications to IC engines, and a literature review on near-wall velocity measurements in IC engines. In chapter four, PIV parameters optimization and error analysis are discussed. In chapter five, experimental setup for both the low resolution and high resolution experiments is described, followed by data processing method applied to each experiment, and ending with results and discussion. Results and issues arose during both experiments are concluded in chapter 6 along with a discussion on suggested modifications to minimize those issues. At the end of chapter 6, a discussion of future work is presented and recommendations are suggested.

CHAPTER 2

INTERNAL COMBUSTION ENGINE HEAT TRANSFER

One of the main reasons this research is carried out is to help provide the means to understand and develop modeling heat transfer analysis in internal combustion engines. Internal combustion engines heat transfer is considered one of the most difficult, if not the most difficult, heat transfer problems. Due to its extreme importance on engines design and performance, researchers utilized different approaches for the past eighty years trying to come up with the ultimate solution for the combustion chamber heat transfer process. However, because of its complexity, no detailed solution (i.e., local and instantaneous) have been verified.

This chapter on IC engines heat transfer is intended to show during its course the importance of a major heat transfer mechanism in IC engines which is convective heat transfer. As will be seen in the literature review, different models have been proposed during the last eighty years; however, no experimental work has been done for the gas side convective heat transfer to predict the local and instantaneous heat transfer coefficient. With the advances of optical engines diagnostics, engine researches are one step closer to resolve hydrodynamic boundary layer on cylinder head and walls, which should give modelers a more accurate velocity profile to implement on their codes rather than the turbulent "law of the wall" which is often used in most models.

It is a common practice when studying the IC engine heat transfer to divide the engine into subsystems (1) and (2). Intake and exhaust are considered two subsystems. Coolant is the third subsystem and lubricating oil is the fourth subsystem. The fifth subsystem is the combustion chamber which is the most important part of the engine and the source of all difficulties. The sixth subsystem is the solid parts that the previous subsystems are made of. In this current research, only the combustion chamber subsystem is considered for boundary layer investigation. Other subsystems, even though they have significant impact on the engine heat transfer problem, are not considered here.

In this chapter, the importance of studying IC engines heat transfer is emphasized by first showing a brief description of its uniqueness and sources of difficultly followed by a step by step analysis of the heat transfer process during the IC engine cycle. Heat transfer mechanisms are then reviewed and then followed by background literature on the combustion chamber heat transfer.

2.1 Importance and Uniqueness of IC Engine Heat Transfer

During the combustion process in IC engines, burned gas temperature reach values in the neighborhood of 2500 K. Exhaust gas temperature is of order 1300 K. Knowing that Aluminum melting point is about 933 K and iron melting point is 1808 K, coolant system must be provided to ensure that piston, cylinder, and valves temperatures are kept below those critical temperatures. In fact, metal temperature must even stay much lower than those temperatures to insure that its strength does not degrade. Heat flux during combustion reaches a maximum of about 10 MW/m^2 in some parts of the engine and then drops to zero during another cycle stage. This heat flux fluctuation happens in a

matter of milliseconds causing a lot of thermal stresses on engine regions affected by such fluctuations; therefore, these regions must be thermally controlled by means of cooling systems to keep them at or below 673 K for iron and 573 K for aluminum alloys. In addition to temporal heat flux fluctuations during one cycle, spatial variation is another source of engine heat transfer difficulty, heat flux vary by as much as 5 MW/m^2 between two spots 1 cm apart. What makes heat flux issue even more complex is that this temporal and spatial pattern varies from cycle to cycle. To avoid lubricating oil deterioration, gas side wall temperatures must be kept below 450 K. Spark plug and exhaust valves, which are usually the hottest parts of the combustion chamber, must be kept cool to avoid pre-ignition problems. Cooling process must be optimized in a way to control the amount of heat transferred to the walls since higher heat transfer to the wall will lower the charge temperature and gas pressure, and therefore reduce the work output. So heat transfer also affects engine performance and efficiency. Another major effect of engine heat transfer is emissions where analysis of such problem must include, in addition to the combustion chamber, the exhaust system which is not the focus of the current research. (2) and (3).

2.2 Combustion Chamber Heat Transfer: Cycle Description

Whether the heat is transferred to or from the walls depends on the operating condition. In general, during the intake stroke, as charge enters the intake port, heat is transferred from the port walls and intake valves to the gas. More heat is transferred to the gas as the charge enters the cylinder drawing more energy from the combustion chamber walls. Even though this process helps vaporizing the fuel and also brings the energy back to the combustion chamber via the intake charge, it reduces the volumetric

efficiency of the engine. During compression, the charge temperature increases to temperatures higher than the combustion chamber walls. Heat is transferred from the gas side to cylinder walls. The importance of heat transfer during the compression stroke is in its effect on knock on SI engines and on ignition timing on CI engines. One-zone models, which will be discussed later, do not determine bulk gas temperature differences within the combustion chamber. The major drawback of one-zone models is that they do not take into account the boundary layer gas which contains a considerable amount of the cylinder mass approximated by 10-20 %. Two-zone model having the core gas as one zone and boundary layer gas as the other zone gives a gas core temperature that is 100-200ºC higher than the mass averaged one zone models (4). This huge discrepancy between the one-zone models and the two-zone models show that there is a need for accurate temperature distribution within the combustion chamber. Heat transfer rates to the walls are the highest during the combustion stage. Gas temperatures increase substantially and fluid motion also increases and continues to do so during the expansion stroke which results in an enhanced forced convection heat transfer to the walls. Higher pressures during combustion force the cylinder gas into crevices which also adds to the heat transfer to the combustion chamber walls. During the expansion stroke, heat transfer rates decrease due to drop in gas temperature and convection heat transfer coefficients which are reduced because of the decrease in gas density during expansion. During blowdown and exhaust, high velocities are generated causing an increase of heat transfer to the exhaust valves and exhaust port walls (1).

2.3 Heat Transfer Mechanisms

The three mechanisms of heat transfer are present in IC engines. Conduction through solids (the sixth subsystem), gas side convection, and radiation from combustion gases to the walls. Conduction and radiation heat transfer are not the focus of the current research; however, a brief description is given below for each of the three heat transfer modes.

2.3.1 Conduction in the Solid Parts

Heat transfer in the solid parts, previously categorized as the sixth subsystem, occurs by means conduction. Conduction heat transfer is described as heat transfer by molecular motion in solids and fluids at rest due to temperature gradient. It is governed by Fourier's law as follows:

$$\dot{q} = -k\nabla T \tag{2.1}$$

where k is the thermal conductivity. For steady one-dimensional temperature gradient

$$\dot{q}_x = -k\frac{dT}{dx}$$

2.3.2 Convection in the gas side

Convection heat transfer is a process of energy transfer between a fluid and a solid surface. Natural convection occurs when fluid motion is buoyancy driven. However,

in IC engines, forced convection is the dominant mode of heat transfer. Driven by forces other than gravity, fluid motions in the combustion chamber are turbulent.

Heat is transferred between the gas side of the combustion chamber and its wall, i.e. cylinder head, piston top, cylinder wall, by means of convection in either direction depending on the phase of the cycle as described previously. Convection is also the driving force of heat transfer on the coolant side, intake port, and exhaust system. It also happens between the engine and the atmosphere.

Convection heat transfer from the gas to the solid is given by Newton's law of cooling

$$\dot{q} = h(T_g - T_w) \tag{2.2}$$

where h is the heat transfer coefficient, T_g is the gas side temperature, and T_w is the solid wall temperature. In a thermal boundary layer, the local heat flux could be determined by applying Fourier's law (Equation (2.1)) to the fluid at the solid surface (y=0, Figure 2-1: flat plate for demonstration purposes):

$$\dot{q} = -k_f \left.\frac{\partial T}{\partial y}\right|_{y=0} \tag{2.3}$$

where k_f is the thermal conductivity of the fluid. The heat transfer coefficient is obtained by combining Equation (2.3) with Newton's law of cooling (Equation (2.2)),

$$h = \frac{-k_f \left. \partial T \middle/ \partial y \right|_{y=0}}{T_g - T_w} \tag{2.4}$$

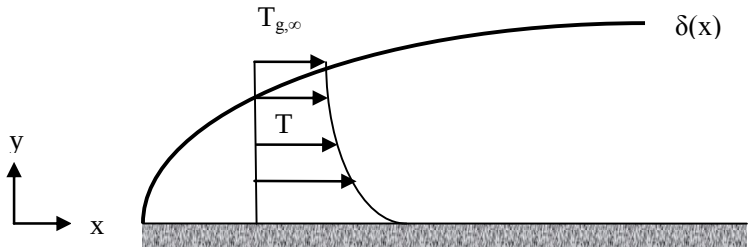

Figure 2-1: Thermal boundary layer

Knowing the temperature distribution in the thermal boundary layer is one way of determining the local heat flux and the local heat transfer coefficient by applying Equations (2.3) and (2.4). Although this method seems simple, the difficulty arises from solving the energy equation, which also requires the knowledge of the velocity profile by solving the momentum equation. With the great advances in computer speeds the past two decades, computational fluid dynamics (CFD) has become a reliable tool of solving the momentum and energy equations for any laminar flow problem; however, gas motion in IC engines is turbulent,

Statistical approach is applied to the transport equations by introducing Reynolds decompositions expressed in index notation as

$$u_i = \bar{u}_i + u_i' \tag{2.5}$$

where i =1, 2, and 3 correspond to x, y, and z Cartesian coordinates, u is the instantaneous velocity, u' is the fluctuation velocity about the mean velocity $\bar{u}$ which could be time, ensemble, or space average. If the time average, space average, and ensemble average are all the same, the flow is called *ergodic*; however, ergodic flows do not exist in IC engines due to cycle-to-cycle variability, and only time and ensemble averages are mainly used when studying cylinder flows in IC engines (see next chapter). Even if the engine has no cycle variability, spatial averages would result in a different representation of the mean that is obtained by either time or ensemble average. Therefore, the flow in engine is still not ergodic.

Scalar quantities also fluctuate and they are represented in terms of decomposition as

$$T = \bar{T} + T',\ p = \bar{p} + p',\ \rho = \bar{\rho} + \rho' \tag{2.6}$$

Reynolds averaged transport equations are obtained by substituting and manipulating the decompositions, shown in Equations (2.5) and (2.6), into the deterministic transport equations; this yields the following general forms of the continuity, momentum, and energy equations (for simplicity of demonstration, density is assumed constant. Next chapter takes density variation in time and space into account):

$$\frac{\partial \bar{u}_i}{\partial x_i} = \frac{\partial u_i'}{\partial x_i} = 0 \tag{2.7}$$

$$\frac{\partial \overline{u}_i}{\partial t} + \overline{u}_j \frac{\partial u_i'}{\partial x_j} = -\frac{1}{\rho}\frac{\partial \overline{p}}{\partial x_i} + \nu \frac{\partial^2 \overline{u}_i}{\partial x_j \partial x_j} - \frac{\partial}{\partial x_j}\overline{u_i' u_j'} \tag{2.8}$$

$$\frac{\partial \overline{T}}{\partial t} + \overline{u}_j \frac{\partial \overline{T}}{\partial x_j} = \alpha \frac{\partial^2 \overline{T}}{\partial x_j^2} - \frac{\partial}{\partial x_j}\overline{u_j' T'} \tag{2.9}$$

where α is the thermal diffusivity defined by

$$\alpha = \frac{k}{\rho c_p} \tag{2.10}$$

The last term on Equation (2.8) and Equation (2.9) requires more information in order to solve for the turbulent boundary layer. These terms are usually modeled and almost all turbulence modeling of these terms are approached by the Boussinesq's gradient transport hypothesis which assumes that the fine scale motions contributes to the transport of mass, momentum, and energy in a similar manner to the molecular transport. Based on that assumption the last term of Equation (2.8) known as the *apparent stresses* or *Reynolds stresses* is given by:

$$-\overline{u_i' u_j'} = \nu_T \frac{\partial \overline{u}_i}{\partial x_j} \tag{2.11}$$

where ν_T is called eddy or turbulent diffusivity. The momentum equation becomes

$$\frac{\partial \overline{u}_i}{\partial t} + \overline{u}_j \frac{\partial u_i'}{\partial x_j} = -\frac{1}{\rho}\frac{\partial \overline{p}}{\partial x_i} + \frac{\partial}{\partial x_j}\left[\left(\nu + \nu_T\right)\frac{\partial \overline{u}_i}{\partial x_j}\right] \tag{2.12}$$

Also, an eddy or turbulent viscosity is defined as

$$\mu_T = \rho \nu_T \tag{2.13}$$

It should be noted that viscosity is a fluid property, but the eddy viscosity is a flow property.

Now it is all a matter of how this turbulent viscosity is modeled. Models could be algebraic, one-equation, and two-equation models. Aside from the general turbulent viscosity modeling, turbulent flow near walls and the current models solving for it are the main interest of the research at hand. Experimental results for the hydrodynamic boundary layer and the two-dimensional velocity vector fields would provide modelers with actual representation of near-wall velocity distribution and actual values for Reynolds stresses; thus validating current models. The most widely used near-wall velocity model is “law-of-the wall”, which is often applied to IC engines analysis. This model may not give a real representation of the boundary layer in IC engines because upon its derivation the mean flow was assumed fully developed and steady, which is not the case in IC engines. It must be noted also that the flow may not be turbulent in IC engines at some instances as will be seen in the next chapter on the boundary layer literature review section.

It is worth noting that one of the known algebraic models of the turbulent diffusivity, known as Prandtl “mixing length model”, could also be investigated in addition to resolving the boundary layer in the combustion chamber. The model expresses the turbulent diffusivity as follows:

$$\nu_T = l^2 \left| \frac{\partial \bar{u}}{\partial y} \right| \tag{2.14}$$

where l is the mixing length. It is determined from the measurements of the turbulent shear stress and the velocity gradient (5):

$$-\overline{u'v'} = l^2 \left(\frac{\partial \bar{u}}{\partial y} \right)^2 \tag{2.15}$$

Analogous to the thermal diffusivity, the last term of Equation (2.9) is defined in term of turbulent thermal diffusivity, α_T

$$\overline{v'T'} = \alpha_T \frac{\partial \bar{T}}{\partial y} \tag{2.16}$$

also, eddy conductivity is defined as follows

$$k_T = \rho c_p \alpha_T \tag{2.17}$$

A turbulent Prandtl number can be defined analogously to the molecular Prandtl number by

$$\mathrm{Pr}_T = \frac{\mu_T c_p}{k_T} = \frac{\nu_T}{\alpha_T} \tag{2.18}$$

The energy equation (Equation (2.9)) can then be written as follows:

$$\frac{\partial \bar{T}}{\partial t} + \bar{u}_j \frac{\partial \bar{T}}{\partial x_j} = \frac{\partial}{\partial x_j}\left[\left(\alpha_T + \frac{\nu_T}{\mathrm{Pr}_T}\right)\frac{\partial \bar{T}}{\partial x_j}\right] \tag{2.19}$$

After this brief description of the governing equation of turbulent flow, an overview of what experimentally has been done to solve for the heat transfer coefficient *h* will be discussed. In the literature, the heat transfer coefficient *h* for steady heat transfer is given for various geometries and flow condition in the following form

$$Nu = C\,\mathrm{Re}^m\,\mathrm{Pr}^n \tag{2.20}$$

Nu is Nusselt number, Re is Reynolds number, and Pr is the molecular Prandtl number.

$$Nu = \frac{hL}{k_f},\ \ \mathrm{Re} = \frac{\rho u L}{\mu} = \frac{uL}{\nu},\ \ \mathrm{Pr} = \frac{c_p \mu}{k_f}$$

where ρ is the fluid density, μ is the dynamic viscosity, ν is the kinematic viscosity, k_f is the fluid thermal conductivity, not to be confused by the solid thermal conductivity mentioned earlier on the conduction heat transfer section. L and u are the characteristic length and velocity.

Heat flux and wall temperatures are measured by means of thermocouples. The gas temperature is determined by the ideal gas law

$$T_g = \frac{pVM}{m\bar{R}} \tag{2.21}$$

where p is the pressure measured by pressure transducer, V is volume, M is the molecular weight of the gas, m is the mass of the gas, and $\bar{R}$ is the universal gas constant. The heat transfer coefficient h is then determined from Newton's law of cooling (Equation (2.2)). A number of tests could be conducted for a variety of test conditions. A *log-log* scale is used to plot Nusselt number vs. Reynolds number for a given Prandtl number which usually assumed constant for combustion gases (Pr = 0.7), and the coefficients C, *m,* and *n* are determined from the plot.

2.3.3 Radiation Heat Transfer

Radiation heat transfer occurs in general from hot areas to cold ones through electromagnetic waves of certain wavelengths. In the combustion chamber, this mode of heat transfer occurs from combustion gases to engines walls. The energy transferred by radiation in the combustion chamber is comparable in magnitude to the amount of energy

transferred by convection in diesel engines only. In SI engines, radiation heat transfer is usually ignored.

If both bodies exchanging energy by means of radiation are black bodies (emits and absorbs equally radiation of all wavelengths), the amount of energy transferred is given by

$$\dot{q} = \sigma(T_1^4 - T_2^4) \tag{2.22}$$

where σ is the Stefan-Boltzmann constant 5.67 x 10^{-8} W/m^2.K^4.

In the combustion chamber, as in most realistic situations, different factors make applying Equation (2.22) not practical. Real surfaces reflections and absorptions depend on shape factors and wavelengths that are accounted for by applying emissivity, absorbtivity, and reflectivity.

All modes of heat transfer in engines are shown below schematically in Figure 2-2.

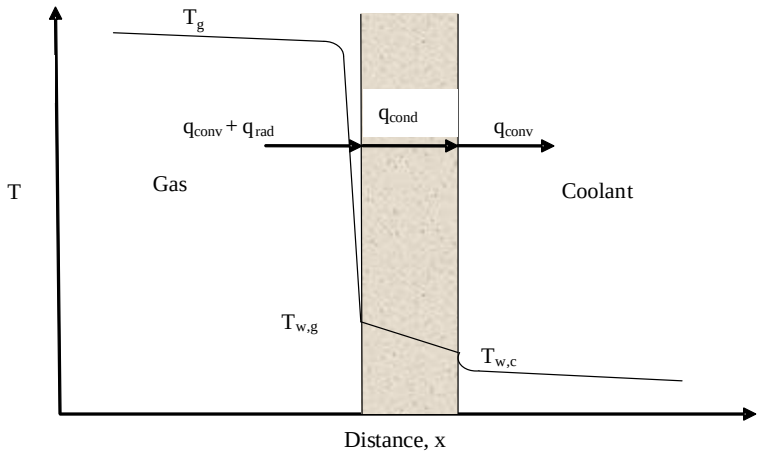

Figure 2-2: Schematic of heat transfer flow from combustion chamber to the coolant through cylinder wall

2.4 Literature Review on Gas Side Convective Heat Transfer

The lack of information necessary for solving the energy equation for IC engines combustion chambers made it difficult for both experimenters and modelers to come up with a satisfactory model for engine heat transfer. For the past 80 years, different models that are the results of different approaches for solving combustion heat transfer problem have been proposed. Those approaches are categorized as follows

- Global (one-zone) thermodynamic models
- Zonal (more than one zone) thermodynamic models
- One dimensional analytical and CFD models
- Multidimensional CFD models
- Radiant heat transfer models.

2.4.1 Global Models

Heat transfer coefficients in global models, with the exception of the instantaneous local correlations, are assumed to be the same for all combustion chamber surfaces. Equation 2.2 is used to calculate heat flux applying the heat transfer coefficients predicted by the global models. Equation (2.2) can be furthered modified to account for local wall temperature differences.

$$\dot{q} = \frac{1}{A} h \sum_{i=1}^{N} A_i \left(T_g - T_{w,i} \right) \tag{2.23}$$

where A is the total area, A_i is the local area, and $T_{w,i}$ is the local wall temperature.

Global models correlations are categorized into three major subcategories:

- Time-averaged heat flux correlations
- Instantaneous spatial average correlations
- Instantaneous local correlations

Major correlations are shown next.

2.4.1.1 *Time-Averaged Heat Flux Correlations*

Taylor and Toong (6) proposed an overall engine heat transfer correlation based on data from 19 different engines with different coolant medium (air or water).. They defined an average effective gas temperature $T_{g,a}$ that would result in $\int Ah\left(T - T_{g,a}\right)d\theta = 0$ over the entire engine cycle. In other words, $T_{g,a}$, is the gas temperature at which the

cylinder wall would stabilize if no heat was removed from the outside. Their Nusselt number equation along with the Reynolds number is shown in Figure 2-3.

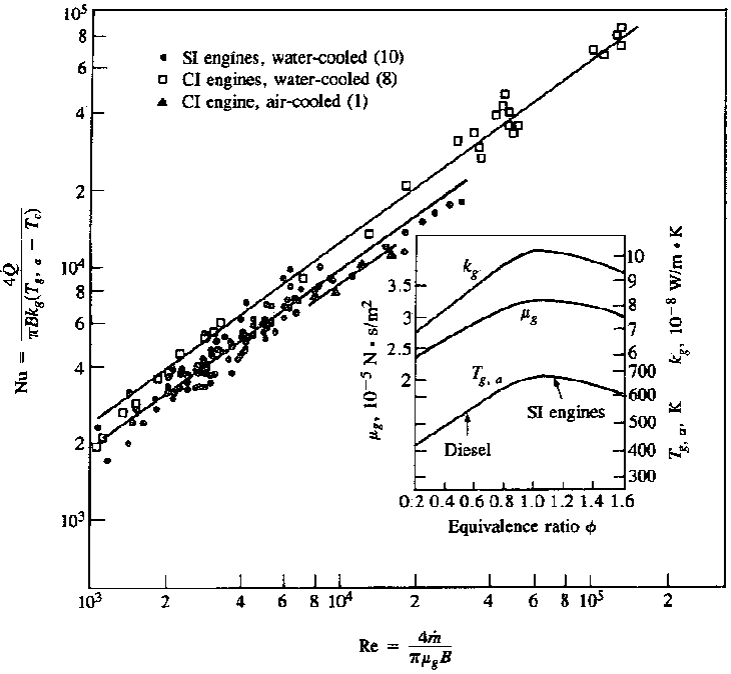

Figure 2-3: Overall engine heat transfer coefficient. μ_g: gas viscosity, k_g: gas thermal conductivity, m: charge mass flow rate (6).

2.4.1.2 *Instantaneous Spatial Average Correlations*

Nusselt (7) presented the first model for engine heat transfer. It is a time average correlation but has been used for predicting instantaneous heat flux. His experiment setup was actually a spherical bomb. His heat transfer coefficient is the sum of convective component, h_c, and radiant component, h_r, each given by:

$$h_c = 5.41\times10^{-3}(1+1.24\bar{V}_p)(p^2T)^{1/3}\ ,\left[\mathrm{kW}/\left(\mathrm{m}^2.\mathrm{K}\right)\right]$$

$$h_r = \frac{4.21\times10^{-4}}{\left(\frac{1}{\varepsilon_g}+\frac{1}{\varepsilon_w}-1\right)}\frac{\left(T/100\right)^4-\left(T_w/100\right)^4}{\left(T-T_w\right)} \tag{2.24}$$

where $\bar{V}_p$ is the mean piston speed in m/sec, p is the instantaneous pressure, T is the instantaneous temperature, and ε_g and ε_w and the gas and wall emissivities, respectively.

The first measurement of instantaneous heat flux in IC engines was carried out by Eichelberg (8). His experiment was done on two stroke and four stroke diesel engines. His proposed heat transfer coefficient is

$$h = 7.67\times10^{-3}(\bar{V}_p)^{1/3}(pT)^{1/2},\quad \left[\mathrm{kW}/\left(\mathrm{m}^2.\mathrm{K}\right)\right] \tag{2.25}$$

Even though dated back to 1939, Eichelberg's correlation is still used for low speed engines.

In 1963, Annand (9) presented his instantaneous heat transfer correlation after examining all available formulas and heat transfer data at that time. His widely used correlation, which is based on steady turbulent convection heat transfer, is:

$$Nu = a\,\mathrm{Re}^{0.7} \tag{2.26}$$

where a is a constant whose value depends on the intensity of the charge motion $(0.35 \le a \le 0.8)$. The characteristic length is the bore and the characteristic velocity is the piston mean speed. Gas properties are to be evaluated at mean bulk temperature instead of the average of the gas and wall temperature using the ideal gas law (Equation (2.21)). Annand full heat flux equation that includes both convection and radiant heat transfer is:

$$\dot{q} = a\frac{k}{B}\mathrm{Re}^{0.7}(T - T_w) + b(T^4 - T_w^4), \quad \left[\mathrm{kW/m^2}\right] \qquad (2.27)$$

where b = 3.3 x 10^{-11} for diesel engines and 4.3 x 10^{-12} for SI engines. Even though data for this correlation were collected from a thermocouple on the cylinder head, it has been used as an approximate for instantaneous spatial average heat fluxes for the entire combustion chamber walls.

Another widely used correlation is the one proposed by Woschni (10). A heat balance approach was used instead of local temperature measurement to determine the amount of heat transfer crossing the combustion chamber walls

$$h = 0.820B^{-0.2}p^{0.8}W^{0.8}T^{-0.53}, \quad \left[\mathrm{kW/m^2.K}\right] \qquad (2.28)$$

where W is the average cylinder gas velocity related to the mean piston speed by the following formula obtained for four stroke, water cooled, four valve diesel engine with no swirl:

$$W = \left[C_1 . \bar{V}_p + C_2 \frac{V_d T_1}{p_1 V_1} (p - p_m) \right] \tag{2.29}$$

where V_d is the displacement volume, p is the instantaneous cylinder pressure in MPa, p_m is the motored cylinder pressure at the same crank angle as p, the subscript 1 indicates a reference point in time when the pressure and temperature are known, for example the beginning of combustion or inlet valve closing. Coefficients C_1 and C_2 are given as follows:

For the gas exchange process: $C_1 = 6.18$, $C_2 = 0$

For the compression process: $C_1 = 2.28$, $C_2 = 0$

For the combustion and expansion process: $C_1 = 2.28$, $C_2 = 3.24 \times 10^{-3}$

Woschni (11) modified those constants for high speed engines with swirl:

For the gas exchange process: $C_1 = 6.18 + 0.417 \frac{\upsilon_s}{\bar{V}_p}$

For the rest of the cycle: $C_1 = 2.28 + 0.308 \frac{\upsilon_s}{\bar{V}_p}$

where $\upsilon_s = \pi B n_D$, and n_D is the rotation speed of the disk used to measure the swirl velocity.

One of the problems with the correlations discussed in this section is that they lack spatial resolution. Franco and Martorano (12) stated in their paper that was published in 1998 in which they evaluated several instantaneous spatially averaged heat transfer models that experiments show that variation of local heat flux is usually out of phase with

the variation of apparent driving temperature difference between gas and the wall. They claim that this out of phase behavior is evidence for the variability of heat flux with both space and time. They further say that "such experimental results have been known for more than 25 years, but they have been largely ignored."

In 2005, Schubert *et al.* (13) mentioned that zero-dimensional models dominate engine cycle heat transfer simulation due to their simplicity; however, such models do not yield satisfactory results in certain application because they lack to consider the actual flow field. Even though this approach gives satisfactory results for a large range of applications, it became obvious in the last few years that this approach is not suitable for certain conditions. Example was given on how Woschni's model predicted too low heat transfer during intake compared to experiment, causing an over estimate of the volumetric efficiency values.

2.4.1.3 *Instantaneous Local Correlations*

Little have been done experimentally to come up with an instantaneous and local heat transfer coefficient correlation to compensate for the drawbacks of the spatially averaged correlations. The difficulty comes from the "local" part of the problem. Thermocouples have to be installed in every location on the cylinder wall making this process not feasible.

LeFeuvre *et al.*(14) carried out a number of experiments measuring wall temperature at eight different locations as shown in Figure 2-4. Cyclic surface

temperature at five locations in the cylinder is shown in Figure 2-5. Heat flux values from their experiments were compared to a number of previously proposed correlations (Figure 2-6). The authors then proposed the use of rotating flow heat transfer correlation for instantaneous and local heat transfer measurements:

$$Nu = 0.047\,\mathrm{Re}^{0.8}\,\mathrm{Pr}^{0.33} \tag{2.30}$$

where the characteristic length in Nusselt and Reynolds number is the circumference of the cylinder instead of the flat plate length, and the characteristic velocity of the Reynolds number is the product of radius and the swirl angular velocity. Their proposed correlation is only applicable to the cylinder head and piston face provided a solid body rotation exist. In their paper, it was shown that the proposed correlation gave good results compared to the motored experimental cases; however, a considerable discrepancy was observed for the fired runs.

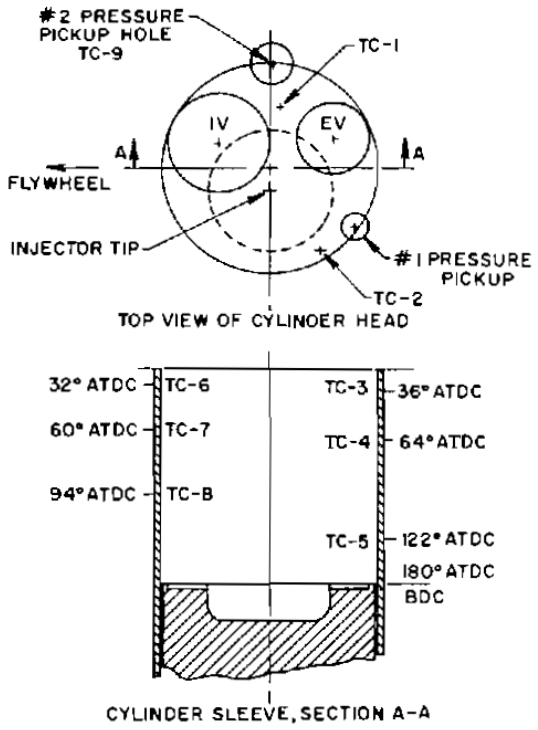

Figure 2-4: Thermocouple locations on cylinder head and wall (14).

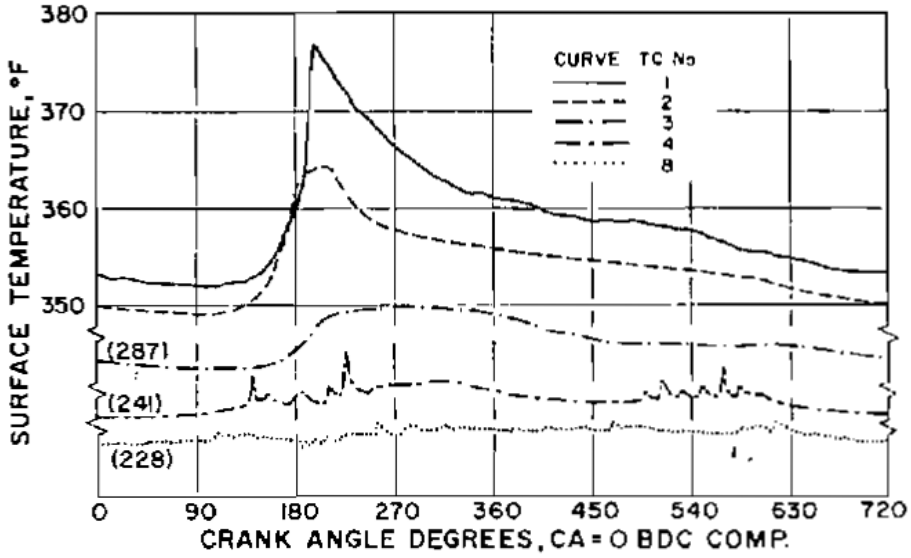

Figure 2-5: Instantaneous temperature distribution at different locations (14).

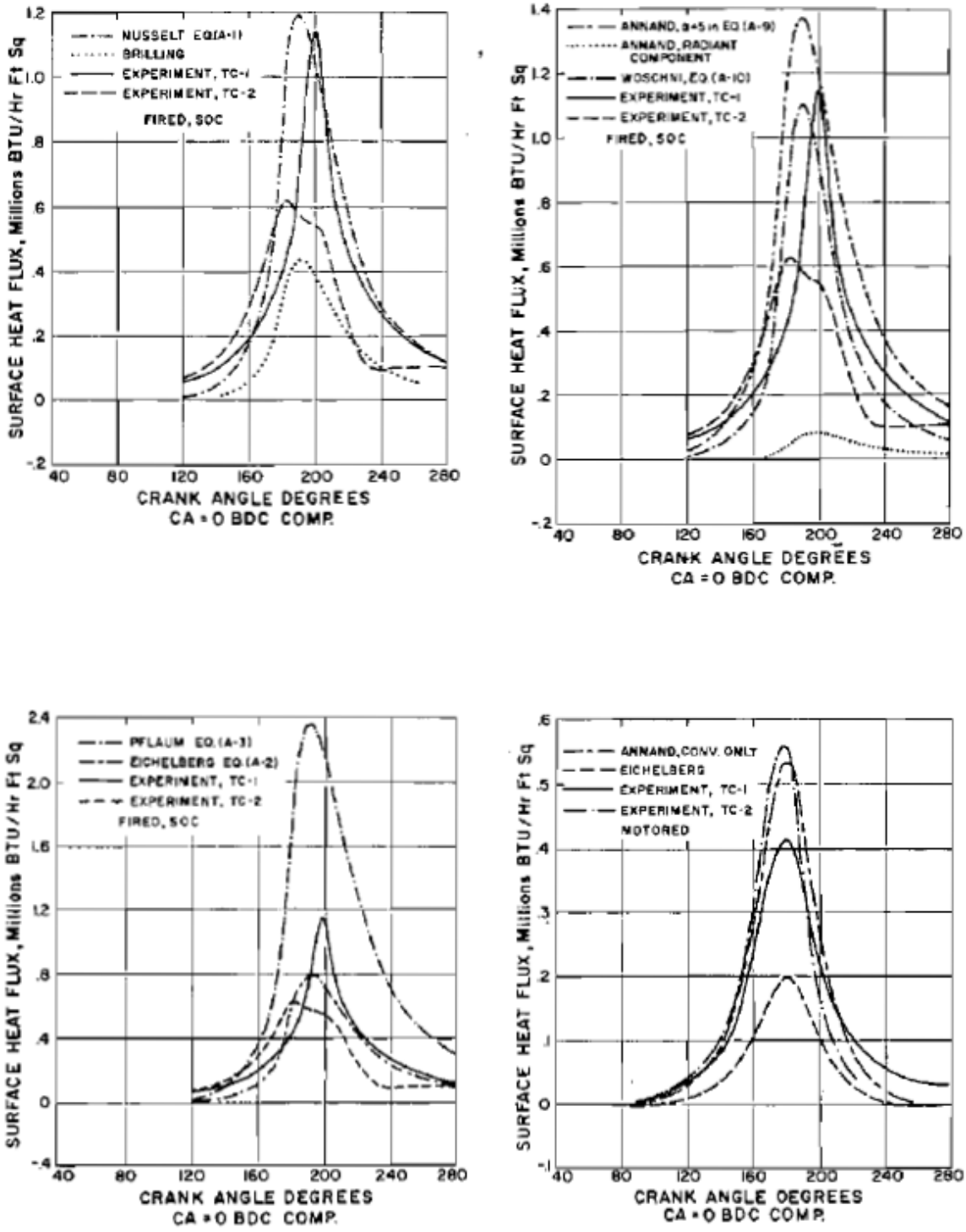

Figure 2-6: Comparisons of predictions of previous correlations with experimental data (14).

It is interesting to mention that spatial variations of local heat fluxes are minimal in homogenous charge compression ignition engines (HCCI) and the study of local heat transfer at one point should be sufficient to generalize for the whole combustion chamber. Chang *et al.* (15) conducted an experimental study on a single cylinder HCCI engine operated with a premixed charge of air and gasoline. Two heat flux probes were inserted in the cylinder head and seven in the piston as shown in Figure 2-7.

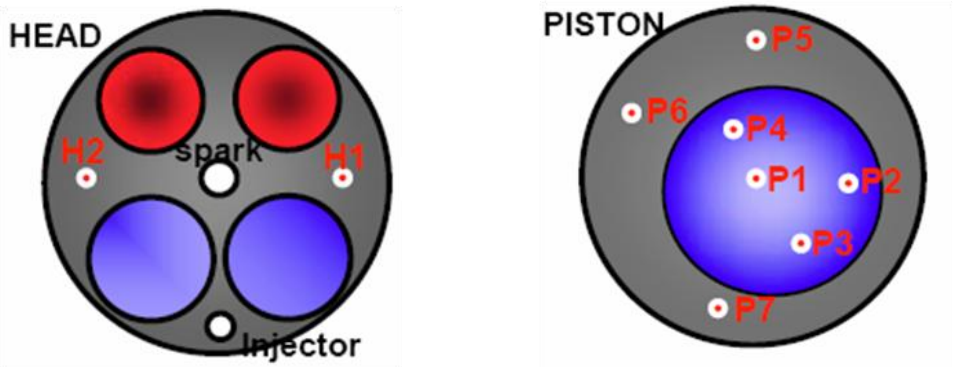

Figure 2-7: locations of heat flux probes (15).

The instantaneous surface heat flux was calculated by solving the unsteady heat conduction equation with two boundary conditions (cylinder wall and 4mm into the solid wall) and one initial condition. The instantaneous temperature distribution measured at various locations on the piston top and cylinder head (ensemble of 200 cycles) is shown in Figure 2-8. A comparison of instantaneous heat flux at different locations between a homogenous charge spark ignition engine and their HCCI engine is shown in Figure 2-9.

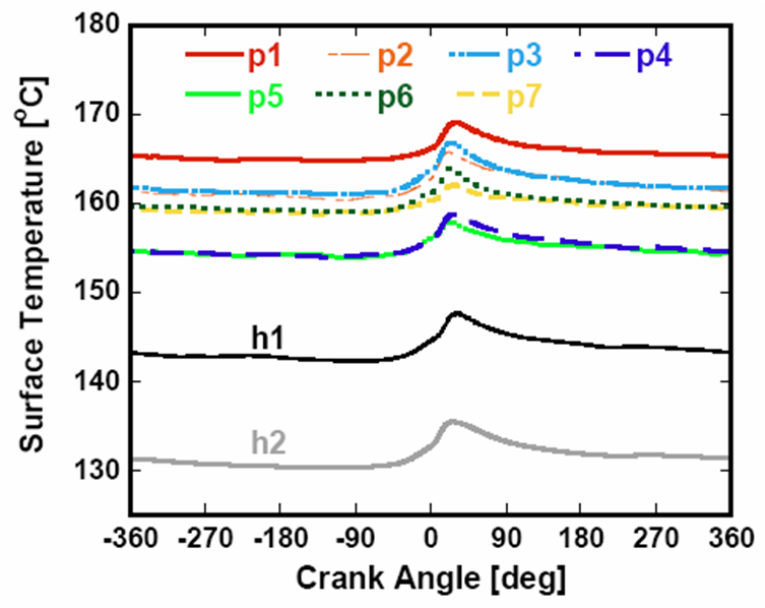

Figure 2-8: Instantaneous temperature distribution measured at various locations on the piston top and cylinder head (15).

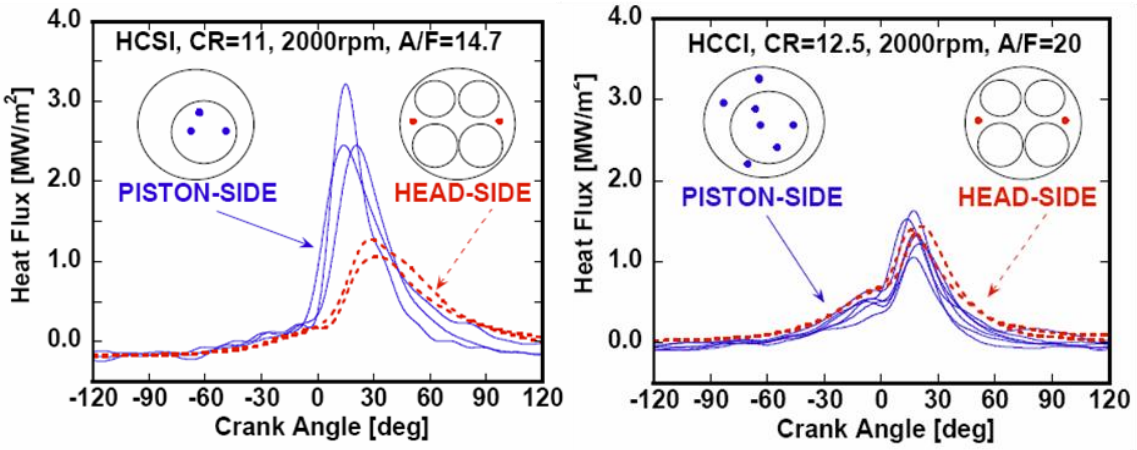

Figure 2-9: Instantaneous heat flux at different locations for a homogenous charge spark ignition engine (left) and the HCCI engine (right) (15).

The authors explain that the expected heat flux uniformity in HCCI engines is due to the fact that not only the charge is homogeneous, but also the conditions during combustion are relatively uniform. Whereas in SI engine, even though having a homogenous charge, the flame front separates the combustion chamber into a hot burned

zone and a cold unburned zone. And in the case of CI combustion, the burning is heterogeneous that the heat flux measurements indicate the conditions near the heat flux probe only. Woschni's equation (Equations (2.28) and (2.29)) was then modified for the HCCI engine,

$$h = \alpha_{scaling} L^{-0.2} p^{0.8} W^{0.8} T^{-0.73} \tag{2.31}$$

$$W = \left[C_1 . \bar{V}_p + \frac{C_2}{6} \frac{V_d T_1}{p_1 V_1} (p - p_m) \right] \tag{2.32}$$

where $\alpha_{scaling}$ is used to tune the coefficient to match engine geometry, and L is the instantaneous chamber height.

2.4.2 Zonal Models

Zonal model divides the combustion chamber into a number of volumes where each has its own temperature and heat transfer coefficient. Krieger and Borman (16) divided the combustion chamber into a burned products and unburned charge zones. Utilizing Eichelberg correlation, Equation (2.25), a heat transfer coefficient was determined for each zone.

Borgnakke *et al*. (17) proposed a local heat transfer two zone model by dividing the combustion chamber into an adiabatic core and a thermal boundary layer. The unsteady boundary layer equation was solved for the unburned and burned gas region of an SI engine. Effective heat conductivity, k_e, was modeled in terms of the turbulent

kinetic energy and an integral length scale characterized by the k-ε model. The local heat flux is given by

$$\dot{q} = k_e (T_\infty - T_w) / \delta \tag{2.33}$$

where T_∞ is the core gas temperature and δ is the boundary layer thickness.

2.4.3 One Dimensional and Three Dimensional CFD Models

Another approach for the heat transfer problem is by solving the one-dimensional energy equation. Assuming one dimensional heat transfer is acceptable provided that temperature gradients normal to the combustion chamber wall are much larger than parallel components.

A number of solutions to the one-dimensional energy equation have been proposed in the past few decades. Some of the solutions were numerical and assumed laminar flow. The solutions to the turbulent energy equation often assume "law of the wall" velocity profile which is not necessarily the case in IC engines.

Three dimensional modeling should provide detailed description of the heat transfer process in IC engines in addition to velocity, turbulence, and chemical reactions. One of the major difficulties facing modelers is resolving velocity distribution near the wall; thus resorting to the "law of the wall" just like the case for the one dimensional models. The problem with applying this law is that it was originally obtained for two-

dimensional, steady, and fully developed flows, and engine flows are far from being steady and are often three-dimensional motions.

One of the recent computer simulations was by Payri *et al.* (18) who conducted a computational study of heat transfer to the walls of a DI diesel engine using commercial CFD package *Fluent*. The purpose of the study was to compare their results to, and modify, a zonal model based on a variant of Woshni equation. The renormalization group (RNG) k-ε turbulence model was used for closure, with *enhanced wall functions*. According to *Fluent 6.2* user guide (19), the enhanced wall function is a special formulation of the law-of-the wall as a single wall law for the entire wall region.

CHAPTER 3

FLOW IN THE CYLINDER

Gas flow in the cylinder has a great impact on the performance of the engine. It has a major role on the combustion process in the engine by enhancing flame speed, and mixing air and fuel in direct injection engines. Convection heat transfer, which is the motivation of the research at hand, is another process in which fluid motion has a direct influence on. Major fluid motions inside the combustion chamber are tumble, swirl, and squish. Initial forms of tumble and swirl are introduced by the intake process, and then may break into smaller structures at the end of the intake process or as compression progresses.

In this chapter, the major fluid motions are described, followed by gas velocity characteristics (mean and turbulence). A more detailed description of the mean flow equations is then introduced as a continuation of what briefly discussed in the convection heat transfer section of the previous chapter (Section 2.3.2) taking into account variable density, kinetic energy budget, and law of the wall. A literature review for the major optical diagnostics, namely Laser Doppler Velocimetry (LDV) and Particle Image Velocimetry (PIV), on IC engines is discussed followed by previous attempts to utilize those techniques to resolve near-wall velocity.

3.1 Major Fluid Motions in the Cylinder

Knowing the major fluid motions, how they are generated, and which part of the combustion chamber do each one interacts with and for how long, is important to know before any near wall measurements are carried out. For example, during intake in an off-axes intake valves, tumble motion is expected to dominate during the intake process, thus a boundary layer with certain properties influenced by the structure of the free stream flow is expected to develop along the cylinder head and cylinder walls in the same plane. If swirl is induced, the free stream behavior would have a different impact on the development and the shape of the boundary layer at the cylinder wall, cylinder head, and piston top.

3.1.1 Tumble and Swirl Mean Flows

Tumble and swirl mean flows most of the times coexist; therefore their descriptions are combined in the same section. Both of these motions are induced in the cylinder by means of valve lift strategies, and port and valve configurations. Schematic of both motions are shown in Figure 3-1.

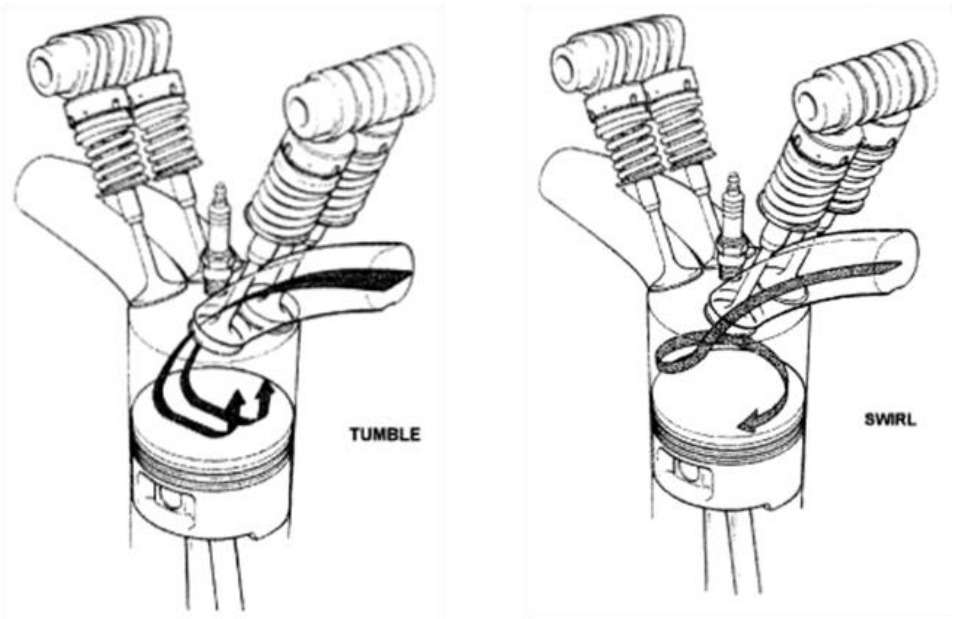

Figure 3-1: Schematic of tumble and swirl, Wilson *et al*. (20).

The intake flow into the cylinder is turbulent and the turbulent velocity is higher than the mean velocity. The purpose of inducing tumble and/or swirl is to turn the incoming flow into a coherent flow which is described as an organized mean flow entrained in the unorganized turbulence. Turbulence in the intake flow is generated by converting the energy of the incoming flow. This turbulence decays real fast leaving too little structured motions at ignition. So the purpose of tumble and swirl is to encapsulate the incoming flow momentum into a coherent flow that is less dissipative and thus lasts longer. During the compression stroke near top dead center, tumble vortex of the size of the bore cannot be retained and break up into smaller vortices of the size of the clearance volume producing high levels of turbulence which produce higher flame speeds. Inducing tumble/swirl also helps in creating the same large scale from cycle to cycle which would reduce cycle-to-cycle variability. Other purposes for inducing mean flow motions are to help having reliable combustion at lean charge or with EGR, and to avoid

knock by generating higher flame speed that allow flame to reach end zone before auto-ignition. Tumble and swirl are also used to stratify the gas inside the cylinder. It is known that inducing swirl will automatically generate tumble motion, not as intense as the swirl motion though. Tumble on the other hand can be induced without swirl; however, secondary tumble motions are usually associated with the main induced mean flow (3).

3.1.2 Squish

Squish occurs toward the end of the compression stroke. Gas flows radially toward the center of the cylinder as the piston approaches the TDC (Figure 3-2). This occurs towards the end of the compression stroke and helps in intensifying the swirl motion.

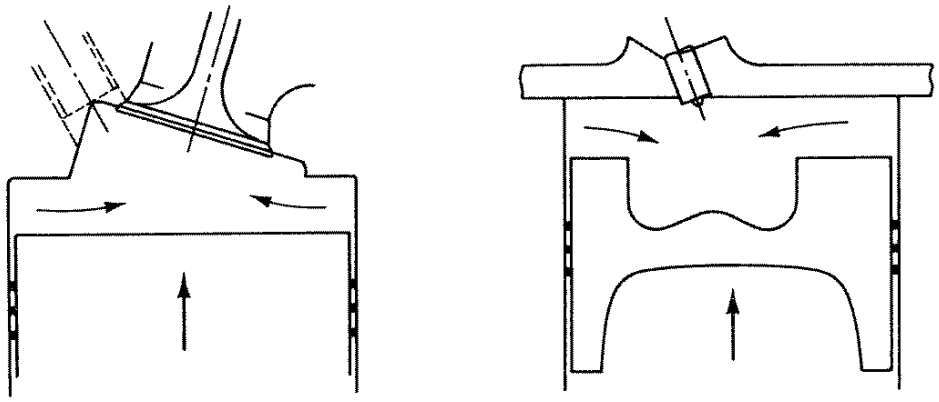

Figure 3-2: Schematic of how piston motion generates squish (2).

3.2 Mean Velocity and Turbulence Characteristics

As discussed earlier, the flow in the cylinder is turbulent. Turbulent flow is defined by fluctuations about an average velocity. Therefore, statistical methods are applied to describe the turbulent flow field. In general, turbulence could be either

stationary in which it does not change statistically with time or non-stationary where statistics vary with time. In cylinder flow is not stationary during the cycle span causing statistics to be different from one crank angle to another. Due to these differences, ensemble average is usually used, also called phase average (2). Time average is also used to find the individual cycle mean, which is also called cycle-resolved mean, which is usually different in value than the ensemble average mean due to cycle-to-cycle variation. It is always important to clarify which average is used since it gives different representation of the cycle mean.

Fluctuation about the mean is used to show the turbulence intensity. It has been a subject of argument which mean should be used to calculate the turbulence intensity in engines. In the literature, some use individual cycle time average mean to determine turbulence intensity and argue that using ensemble average mean will over estimate turbulence intensity since cycle-to-cycle variation will add up to the fluctuations (21). They usually call the intensity evaluated at the ensemble average mean "fluctuation intensity". Others, however, will calculate turbulence intensity using the ensemble average mean proposing that cycle-to-cycle variations are mainly due to the initial flow at the end of the intake process. These differences in flow conditions at the end of the intake stoke, even if they are small in value, can cause noticeable variability since turbulence is sensitive to initial conditions (3).

The ensemble average is a function of crank angle θ and individual cycle i. The instantaneous velocity at a certain crank angle on specific cycle is given by

$$u(\theta,i)=\bar{u}(\theta)+u'(\theta,i) \tag{2.34}$$

where $u'(\theta,i)$ is the fluctuation velocity and $\bar{u}(\theta)$ is the ensemble average velocity given by

$$\bar{u}(\theta)=\frac{1}{N}\sum_{i=1}^{N}u(\theta,i) \tag{2.35}$$

where N is the number of cycles. The decomposition of an instantaneous property, whether scalar or vector, into its mean and fluctuation is referred to as the *Reynolds decomposition*. The fluctuation/turbulence intensity is defined as the root mean square of the fluctuation velocity

$$u'_{rms}=\left(\frac{1}{N}\sum_{i=1}^{N}u'^{2}(\theta,i)\right)^{1/2} \tag{2.36}$$

The time average, also called cycle-resolved mean, on the other hand is a function of time *t*. The instantaneous velocity is given by

$$u(t)=\bar{u}+u'(t) \tag{2.37}$$

where $u'(t)$ is the fluctuation velocity and $\bar{u}$ is the time average velocity given by

$$\bar{u} = \frac{1}{\tau}\int_{-\tau/2}^{+\tau/2} u(t)dt \tag{2.38}$$

where τ is the time period over which the instantaneous velocity is averaged. It is an intermediate time scale between the smallest and largest scales of turbulence. The cycle-resolved mean could also be determined by taking the Fourier transform of the velocity time record of each cycle. Fourier coefficients of all frequencies above a selected cutoff frequency are set to zero. The result is inverse transformed back to the time domain yielding the cycle-resolved mean. This frequency filtering method for determining the cycle-resolved mean is equivalent to the moving average approach (Equation (2.38)) in the time domain over a characteristic time interval equivalent to the reciprocal of the cutoff frequency (22), hence the name "time average".

3.3 Mean Flow Equations

The mean flow equations were introduced in Chapter 2 with the assumption of constant density to explain the importance of understanding the flow behavior in order to solve the convection heat transfer problem properly. The following is a more elaborate description of mean flow equation taking into account density temporal and spatial variations.

The continuity equation in index notation is given by

$$\frac{\partial \rho}{\partial t} + \frac{\partial}{\partial x_i}\left(\rho u_i\right) = 0 \tag{2.39}$$

The temporal gradient of density cannot be assumed negligible since density changes drastically throughout the internal engine cycle duration.

Applying Reynolds decomposition and taking the average of Equation (2.39) results in the following form of the continuity equation:

$$\frac{\partial \bar{\rho}}{\partial t} + \frac{\partial}{\partial x_i}\left(\bar{\rho}\bar{u}_i + \overline{\rho' u_i'}\right) = 0 \tag{2.40}$$

Dividing the terms inside the parenthesis by the mean density leads to the Favre average of velocity (23),

$$\tilde{u} = \bar{u} + \frac{\overline{\rho' u'}}{\bar{\rho}} \tag{2.41}$$

where the first term on the right hand side is the ensemble averaged velocity. Favre average is actually defined as follows (23)

$$\tilde{\varphi} = \frac{\overline{\rho\varphi}}{\bar{\rho}} \tag{2.42}$$

where φ is any scalar or vector property.

If the density is constant per CAD (instantaneous density is equal to the ensemble averaged density), then the second term in the parenthesis of Equation (2.40) drops out. Having the same density per realization (CAD) also simplifies calculations of turbulent quantities where density is involved (i.e. Reynolds stresses).

Therefore, Favre average of the normal x-component Reynolds stresses where determined from 180 to 330 CAD, and then compared to their corresponding ensemble averaged values. Error between the two was found to be around 0.31% on average as will be seen in Chapter 5. Hence, it is reasonable to assume constant density at a given CAD. The mean continuity equation therefore reduces to

$$\frac{\partial \bar{\rho}}{\partial t} + \frac{\partial}{\partial x_i}\left(\bar{\rho}\bar{u}_i\right) = 0 \tag{2.43}$$

and with mathematical manipulations and with the assumption of spatially homogeneous density in the combustion chamber, the fluctuation form of the continuity equation becomes

$$\frac{\partial u_i'}{\partial x_i} = 0 \tag{2.44}$$

It is quite important to point out that density cannot be assumed homogenous within the combustion chamber especially near the wall region because of the substantial temperature gradient that drives heat transfer to the wall; however, this assumption was

made above due to lack of temperature distribution information. This fact should emphasize the need to carry out a simultaneous thermal boundary layer investigation in order to have a complete data set that would provide the means for modeling validation.

The Navier-Stokes (momentum) equations are averaged. The result is the mean-momentum equations, also known as *Reynolds equations*,

$$\frac{\partial\left(\rho\bar{u}_i\right)}{\partial t}+\rho\bar{u}_j\frac{\partial\bar{u}_i}{\partial xj}=-\frac{\partial\bar{p}}{\partial x_i}+\rho g_i+\mu\frac{\partial^2\bar{u}_i}{\partial x_j\partial x_j}-\rho\frac{\partial}{\partial x_j}\overline{u_i'u_j'} \tag{2.45}$$

The Reynolds equations appear to be similar to the Navier-Stokes equations with the instantaneous velocities and pressure being replaced with their averages. There is, however, an additional term (4th term on the right hand side of Equation (2.45)). This last term represents stresses due to turbulent fluctuation motion. These additional stresses are called *apparent stresses* or *Reynolds stresses*.

Analogous to the molecular momentum transport due to viscous stresses, Reynolds stresses transfer momentum by means of fluctuating velocity field. Davidson (24) states that Reynolds stresses are not actually true stresses but they represent the mean momentum fluxes by the turbulence, and the effects of these fluxes can be captured by pretending that these terms are stresses. Reynolds stresses usually dominate the viscous stresses; thus, the latter is usually neglected except in regions very close to the wall.

The set of the three Reynolds equations and the continuity equation contain more than four unknowns. In addition to the average pressure and the three components of the average velocity, there are also Reynolds stresses which are the components of a second order tensor. Problem like that is said to be unclosed and additional equations linking the Reynolds stresses to the mean flow is required to solve the *closure problem*. These additional equations are called turbulence models. Brief description on Reynolds stresses modeling was discussed on the previous chapter.

For this experiment, Reynolds stresses near the cylinder head will be determined from the 2D vector fields obtained from the μPIV+PTV measurements.

The balance of the kinetic energy of the turbulent fluctuations (*k*-Equation) is important when studying turbulence fluctuations and their physical impacts. Equation (2.46) shows the quantity of the kinetic energy that is to be balanced,

$$k = \frac{1}{2}\overline{q^2} = \frac{1}{2}\overline{u_i'^2} \tag{2.46}$$

The *k*-Equation is given by

$$\frac{D}{Dt}(\rho k) = -\frac{\partial}{\partial x_j}\left(\overline{p'u_j'} + \frac{1}{2}\rho\overline{u_i'^2 u_j'} - 2\mu\overline{u_i' e_{ij}}\right) - 2\mu\overline{e_{ij}e_{ij}} - \rho\overline{u_i'u_j'}\frac{\partial \overline{u}_i}{\partial x_j} \tag{2.47}$$

The *k*-Equation illustrates the energy balance between the different inputs of turbulent fluctuations. The term on the left hand side is turbulence kinetic energy convection. The first three terms on the right-hand side of represent the diffusion of turbulent kinetic energy; the first two terms correspond to the diffusion by turbulence, and the third term denotes viscous diffusion. The fourth term is the turbulent kinetic energy production which is the rate of energy generation due to the interaction of the Reynolds stresses with the mean shear. The fifth term on the right-hand side is the viscous dissipation of turbulent kinetic energy. It is a sink where kinetic energy is transformed to internal energy.

3.3.1 Boundary Layer Equations for Plane Flows

Following similar assumptions made to laminar boundary layers flows ($\bar{v} << U_\infty$, $\partial/\partial x << \partial/\partial y$), where U_∞ is the free stream velocity, the continuity, momentum, and turbulent kinetic energy equations for plane turbulent boundary layer in Cartesian coordinates are simplified as follows (for more details on boundary layer estimations, refer to (25)):

$$\frac{1}{\bar{\rho}}\frac{\partial \bar{\rho}}{\partial t} + \frac{\partial \bar{u}}{\partial x} + \frac{\partial \bar{v}}{\partial y} = 0 \tag{2.48}$$

$$\frac{\partial\left(\bar{\rho}\bar{u}\right)}{\partial t} + \bar{\rho}\left(\bar{u}\frac{\partial \bar{u}}{\partial x} + \bar{v}\frac{\partial \bar{u}}{\partial y}\right) = -\frac{\partial \bar{p}}{\partial x} + \frac{\partial}{\partial y}\left(\mu\frac{\partial \bar{u}}{\partial y} - \bar{\rho}\overline{u'v'}\right) \tag{2.49}$$

$$\frac{\partial\left(\bar{\rho}k\right)}{\partial t} + \bar{\rho}\left[\bar{u}\frac{\partial k}{\partial x} + \bar{v}\frac{\partial k}{\partial y}\right] = -\frac{\partial}{\partial y}\left[\overline{v'\left(\frac{\rho}{2}q^2\right)}\right] + \mu\left[\frac{\partial^2}{\partial y^2}\left(k + \overline{v'^2}\right)\right] - \bar{\rho}\overline{u'v'}\frac{\partial \bar{u}}{\partial y} - \bar{\rho}\tilde{\varepsilon} \tag{2.50}$$

where the dissipation for plane flows is expanded as follows:

$$\tilde{\varepsilon} = \nu \left[2\overline{\left(\frac{\partial u'}{\partial x}\right)^2} + 2\overline{\left(\frac{\partial v'}{\partial y}\right)^2} + \overline{\left(\frac{\partial u'}{\partial y}\right)^2} + \overline{\left(\frac{\partial v'}{\partial x}\right)^2} + 2\overline{\frac{\partial u' \partial v'}{\partial y \partial x}} \right] \tag{2.51}$$

The velocity fluctuation part of the viscous diffusion (second component in the second term on the right hand side of Equation (2.50)) is sometimes combined with the dissipation term resulting in what is known as a *pseudo-dissipation*. The resulting *k*-Equation is

$$\frac{\partial(\bar{\rho}k)}{\partial t} + \bar{\rho}\left[\bar{u}\frac{\partial k}{\partial x} + \bar{v}\frac{\partial k}{\partial y}\right] = -\frac{\partial}{\partial y}\left[\overline{v'\left(\frac{\rho}{2}q^2\right)}\right] + \mu\left[\frac{\partial^2}{\partial y^2}(k)\right] - \bar{\rho}\overline{u'v'}\frac{\partial \bar{u}}{\partial y} - \bar{\rho}\varepsilon \tag{2.52}$$

and the pseudo-dissipation is re-arranged as follows

$$\varepsilon = \nu \left[\overline{\left(\frac{\partial u'}{\partial x}\right)^2} + \overline{\left(\frac{\partial v'}{\partial x}\right)^2} + \overline{\left(\frac{\partial u'}{\partial y}\right)^2} + \overline{\left(\frac{\partial v'}{\partial y}\right)^2} \right] \tag{2.53}$$

First order and second order derivatives are determined by finite difference schemes applied to the vector field grid shown in Figure 3-3.

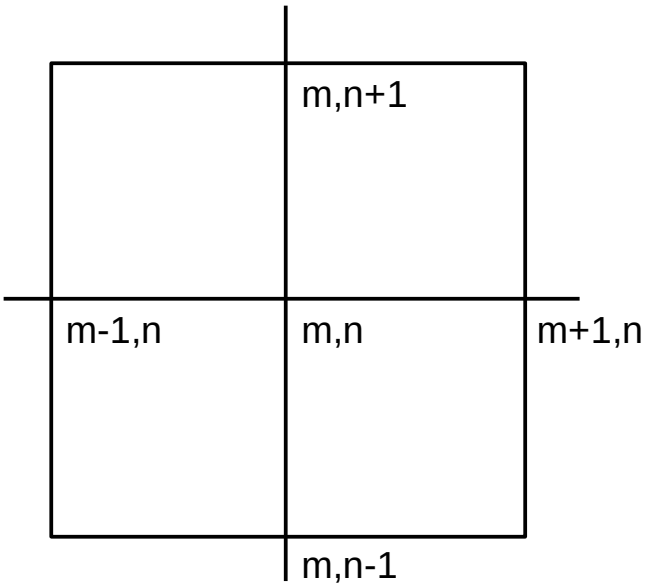

Figure 3-3: Velocity vector grid.

First order and second order spatial derivatives are obtained from the following two central differences equations, respectively. Spatial derivatives at grid points at the boundaries are determined by forward and backward differencing the vector field. Temporal derivatives are obtained similarly. More detailed description of the different differencing schemes used could be found in (23).

$$\left(\frac{\partial u}{\partial x}\right)_{m,n} = \frac{u_{m+1,n} - u_{m-1,n}}{2\Delta x} \tag{2.54}$$

$$\left(\frac{\partial^2 u}{\partial x^2}\right)_{m,n} = \frac{1}{\Delta x^2}\left(u_{m+1,n} - 2u_{m,n} + u_{m-1,n}\right) \tag{2.55}$$

3.3.2 The Universal Law of the Wall

Turbulent flows bounded by at least one solid surface have been investigated for different types of configurations. Fully developed channel and pipe flows, and the flat plate boundary layer, in which the mean velocity is mainly parallel to the wall, were found to have universal characteristics.

Gas flow in internal combustion engines is a unique turbulent wall flow in which different types of mean motions (tumble, swirl, and squish) are involved throughout the engine cycle. The flow is primarily three dimensional and the mean flow is not necessarily parallel to the wall. Flow also varies from one stroke and cycle to another. While the intake flow exhibits a jet-like flow inducing tumble and/or swirl mean motion, compression stroke flow is mainly driven by those induced motions. The power stroke flow is affected by the combustion process and the exhaust stroke gas flow is driven by pressure difference and piston motion. Valves timing is another factor that impacts the flow behavior.

With the complexity of the engine gas flow mentioned above, it is important to study the feasibility of applying the universal law of the wall model, which is derived for steady and fully developed two dimensional turbulent channel or boundary layer flows, to the near wall gas flow in internal combustion engines.

In this experiment, the law of the wall will be investigated and compared to experimental results of near cylinder head flow from 180 to 330 CAD. Results after 330

CAD cannot be tested since the flow actually starts decreasing and eventually reversing as will be shown from the low resolution experiment causing the law of the wall model to fail. This flow reversal observation emphasizes the need for full optical boundary layer investigation of the whole engine cycle at different locations to validate or exclude the application of turbulent model for near wall flows at specific locations and/or timings. The following is a brief description of the universal law of the wall.

The no-slip boundary condition dictates that the Reynolds stresses are zero at the wall. The wall shear stress is thus completely due to viscous effects and is equal to:

$$\tau_w = \mu \left. \frac{d\bar{u}}{dy} \right|_{y=0} \tag{2.56}$$

At a given wall shear stress, the inner velocity scale known as *friction velocity* is given by

$$u_\tau = \left(\frac{\tau_w}{\rho} \right)^{1/2} \tag{2.57}$$

and the *inner* (or viscous) length scale is given by

$$l_\tau = \frac{\nu}{u_\tau} \tag{2.58}$$

The distance from the wall in terms of viscous lengths, known as *wall units*, is given by

$$y^+ = \frac{y}{l_\tau} = \frac{u_\tau y}{\nu} \tag{2.59}$$

which is similar to the *friction Reynolds number* defined by

$$\mathrm{Re}_\tau = \frac{u_\tau \delta}{\nu} \tag{2.60}$$

so the magnitude of the wall units could be interpreted as a measure of viscous and turbulence effects. The inner velocity is given by

$$u^+ = \frac{\bar{u}}{u_\tau} \tag{2.61}$$

Based on the wall units, different regions within the turbulent boundary layer are defined. *The inner layer* ($y/\delta < 0.1$) is where the average velocity is determined from the friction velocity (u_τ) and the wall unit. Within the inner layer is the *viscous wall region* ($y^+ < 50$) where the viscous effect on the shear stress is significant, and below $y^+ = 5$ is the *viscous sublayer* where Reynolds shear stress is negligible in comparison with the viscous stress.

In *the outer layer* ($y^+ > 50$), the effects of viscosity are negligible. The region between the inner and outer layers is the *overlap region* ($y^+ > 50$, $y/\delta < 0.1$). Within the overlap region and the inner layer, the *log-law* holds between $y^+ > 30$ and $y/\delta < 0.3$. The region between the viscous sublayer and the log-law region is called the *buffer layer* ($5 < y^+ < 30$) (26).

The behavior of the velocity profile within the inner layer is the same whether the flow is inside a channel or over a flat plate (boundary layer flow). In the outer layer, however, the boundary layer shows a significant departure from the log law which requires different treatment of the *velocity-defect law* which describes the velocity profile in the outer region (26). In this experiment, the high resolution imaging limits the near-wall flow investigations to within the inner layer, namely the viscous sublayer and the log-law region. Therefore, no special assumptions are needed to further approximate the near cylinder head flow to either a channel flow or a boundary layer (flat plate) flow. It is important though to have a careful examination to the outer layer region of the near cylinder head flow in future studies that extend the investigations to a wider range of the turbulent boundary layer regions.

The viscous sublayer ($y^+ < 5$) velocity profile is linear and given by

$$u^+ = y^+ \tag{2.62}$$

In the log-law region ($y^+ > 30$ and $y/\delta < 0.3$), the velocity profile is determined by

$$u^+ = \frac{1}{\kappa} \ln y^+ + B \tag{2.63}$$

where κ is the von Karman constant and is equal to 0.41, and B = 5.2. In the literature, variations in the values of these two constants are within 5% (26).

3.4 Analysis of Instantaneous Velocity Vector Fields

One of the advantages of two-dimensional velocity vector fields obtained from PIV is the extended amount of information that could be extracted from the instantaneous velocity fields. In addition to Reynolds decomposition, which is widely applied to turbulence statistics as was discussed earlier (i.e. Reynolds stresses and turbulence kinetic energy budget), other decomposition methods could be used on the instantaneous velocity fields to reveal more information about the turbulence structure. The visualization and identification of small-scale structures not only help in assessing the turbulence dynamics but also extend the analysis of heat transfer problem from studying the mean flow boundary layer effect to investigating the instantaneous impact of turbulence structures on transporting thermal energy to and away from the wall.

Adrian *et al.* (27) explain that identification of vortices in a velocity field and conducting vortex statistics such as diameter and strength is usually accomplished by locating regions of isolated regions of significant vorticity. While this procedure is straightforward in simple flows with minimal shear, vortices in complex flows are generally masked by region of significant shear which degrades vortex statistics. In such complex flows, it is difficult to utilize vorticity maps to identify vortices.

In addition to Reynolds decomposition, Adrian *et al.* (27) presents other decomposition methods that help visualize small-scale structures along with modern eddy classifier based on critical-point analysis of the local velocity gradient tensor which determines swirling strength. Those decomposition methods to visualize turbulence structures and identify their strength are presented next after a brief definition of a vortex.

There is no agreed-upon definition of a vortex. One of the common definitions is the one by Kline and Robinson (28) in which they state that "A vortex exists when instantaneous streamlines mapped onto a plane normal to the core exhibit a roughly circular or spiral pattern, when viewed in a reference frame moving with the center of the vortex core".

3.4.1 Visualization of Vortices

From the vortex definition mentioned above, two important conditions should be met to properly visualize a turbulence structure. The first condition is that a velocity field must be viewed in a frame that has the same velocity as the vortex core. The second condition dictates that the vorticity is concentrated at the core of a vortex (27). A turbulent flow field consists of a number of small-scale structures embedded in a large-scale structure. To be able to extract those small-scale structures, the velocity at the center of each small vortex has to be removed.

One of the decomposition methods used to recognize vertical structures is the Galilean analysis is which the total instantaneous velocity is represented as follows

$$u = U_c + u_c \tag{2.64}$$

where U_c is a constant convection velocity and u_c is the deviation. Most vortical structures could be revealed if a wide range of convection velocities is tested. Visualized vortices at a certain convection velocity actually move at that velocity.

Reynolds decomposition (Equation (2.5)) reveals more vortices than a single Galilean decomposition because vortical structures often move at velocities similar to the local mean velocity. On the other hand, it removes large-scale features associated with the mean flow while the Galilean decomposition retains those large-scale structures.

In the large eddy simulation (LES) decomposition, the large-eddy field is defined by the low-pass filtering the total velocity as follows

$$\bar{u}(x,t) = \int_D f(x,x')u(x',t)dx \tag{2.65}$$

where $\bar{u}$ is the filtered large-scale field, f is the filtering kernel and D is the domain of the velocity field. The total velocity field is given by

$$u = \bar{u} + u'' \tag{2.66}$$

where u'' is the remaining smaller-scale field. The filtering kernel f could be any standard homogeneous filter (Gaussian, top-hat, etc), or inhomogeneous filter using proper

orthogonal decomposition methods (27). Equations (3.31) to (3.33) are adapted from Adrian *et al*. (27) where interested reader could refer to for more details on the subject of vortex visualization.

3.4.2 Vortex Identification

As mentioned earlier, vorticity maps do not show vortex cores only but also shearing motions in the flow field. Shear layers are highly present in near-wall flows and relying on the vorticity maps to reveal vortex structures may results in masking out those turbulent eddies (27). Therefore, other methods have to be applied to extract vortex cores in order to obtain a more reliable statistics.

One of the methods proposed to identify vortex cores embedded in a flow field is based on critical-point analysis of the local velocity gradient tensor (29), (30), and (31). The local velocity gradient tensor (in three dimensions) will have one real eigenvalue (λ_r) and a pair of complex conjugate eigenvalues ($\lambda_{cr} \pm i\lambda_{ci}$) if the discriminant of its characteristic equation is positive. Zhou *et al.* (30) and (31) demonstrate that λ_{ci} quantifies the strength of any local swirling motion. Adrian *et al.* (27) show that for two-dimensional fields (PIV planar fields), an equivalent two-dimensional form of the local velocity gradient tensor can be analyzed yielding either two real eigenvalues or a pair of complex conjugate. Vortices are identified by plotting iso-regions of $\lambda_{ci} > 0$. From LaVision's FlowMaster manual (32), λ_{ci} for a two-dimensional velocity gradient tensor is given by

$$\lambda_{ci} = -\left(\frac{\partial u}{\partial y}\frac{\partial v}{\partial x} - \frac{1}{2}\left(\frac{\partial u}{\partial x}\frac{\partial v}{\partial y} \right) + \frac{1}{4}\left(\left(\frac{\partial u}{\partial x} \right)^2 + \left(\frac{\partial v}{\partial y} \right)^2 \right) \right) \tag{2.67}$$

The plots of swirling strength can be used to validate the results obtained from flow field decomposition, and to further modify the decomposition parameters to reveal more vortex motions (i.e. perform local Galilean decomposition in the vicinity of a vortex, or reduce/increase the size of the LES domain).

3.5 Experimental Flow Diagnostic Techniques and Their Applications to IC Engines

Over the past few decades, laser diagnostic techniques applied to fluid flow measurements have gained great popularity and became more reliable and accepted as the laser technology have advanced providing a wide range of products ready to utilize for different flow measurement situation.

3.5.1 Laser Doppler Velocimetry

Laser Doppler Velocimetry (LDV), also known as Laser Doppler Anemometry (LDA), was first demonstrated in 1964 by Yeh and Cummins (33). Since then it has developed into a major non-intrusive flow diagnostic technique that provides instantaneous velocity and turbulence intensity. LDV can measure velocity at high temporal resolution at specific spatial locations.

The general setup of LDV consists of a collimated and coherent light source (laser) that is split into two beams in parallel which then cross each other at the laser

beam waist at a certain angle to create straight fringes perpendicular to the flow direction. The flow is seeded with a material that is light enough to follow the flow faithfully. As the seeding particles cross the fringes they reflect light to a photo detector. Knowing the distance between the fringes and the frequency the particles cross the fringes determined by the photo detector, the velocity can them be calculated.

Early applications of LDV on IC engines were carried out by Witze in the late 1970's. One of his early papers is (34) where several new measurement techniques were applied to direct injection stratified charge motored engine. Velocity and turbulence levels were measured during compression and injection using dual beam backscatter optical arrangements. Radial distribution of the mean tangential velocity at half of the clearance height is shown on Figure 3-4. The outermost radial position where velocity was resolved was at x/R = 0.99 corresponding to 380μm. Radial velocity at this outermost position ranges 13 to 24 m/s depending on the crank angle as could be seen on Figure 3-4. The authors concluded that there was no evidence of the wall boundary layer and it was clearly very thin.

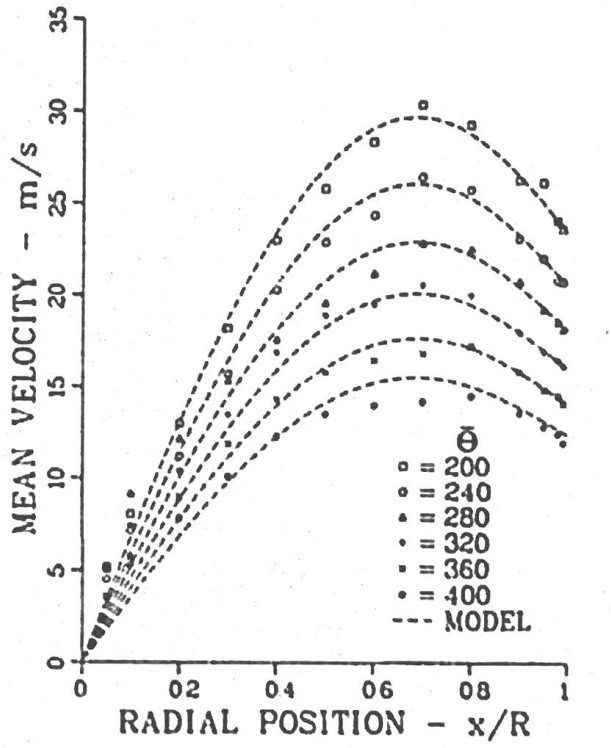

Figure 3-4: Radial distribution of mean tangential velocity at half of the clearance height (34).

3.5.2 Particle Image Velocimetry

The use of LDV has faded away with the introduction of Particle Image Velocimetry (PIV) twenty four years ago. Providing means of measuring velocity in a plane (2D) and even in a volume (3D stereo PIV and holographic PIV), this method provides high spatial resolution velocity measurement where in addition to turbulence intensity, derivative quantities such as strain rates and vorticity can also be approximated. With the advances in laser technology, higher temporal resolutions can also be achieved making PIV even more attractive than LDV.

PIV originated from Laser Speckle Velocimetry, a method which was based on laser speckle measurement of solid body deformation. A number of researcher in 1977

independently applied laser speckle to fluid flow by measuring the velocity profile in pipe flow (35), (36), and (37). After their success, Meynart conducted intensive research on this promising method and had shown that measurement of laminar flow and turbulent flow of liquids and gases could be achieved. According to him, even though the presence of a classical speckle in the photograph was not essential, the technique was called speckle velocimetry to emphasize the close connection between the processing methods used in his paper and in speckle photography (38).

It was revealed from Meynart images that speckle images were actually particle images. Pickering and Halliwell (39) and Adrian (40) recognized the importance of particle images, and Adrian argued that light sheet illumination of seeding particles results on particle images and not speckle patterns. The name particle image velocimetry (PIV) was then proposed declaring the birth of a new flow measurement technique that has developed substantially the past twenty five years.

The following is a brief general description of PIV. PIV is a non-intrusive measurement optical technique which allows velocity measurements in high speed flows or in boundary layers close to the walls without disturbing the flow by pressure probes or hot wires as the case in conventional measurement techniques. Small tracer particles are introduced to the flow that have to be large enough to scatter as much light from the light sheet and at the same time small to follow the flow faithfully. The light sheet produced by lasers and accompanying optics is illuminated twice with a time delay that depends on the mean flow and the magnification of the imaging system. The Mie scatter by the

seeding particles is recorded by film camera or high-resolution digital camera. The latter is used in the current research where the output of the camera sensor is transferred directly from the camera's built-in memory to the computer memory. Consecutive particle images are either recorded on the same frame where autocorrelation is used to process the images or on double frames where cross-correlation is applied to process the data. Autocorrelation has a drawback of vector direction ambiguity. Image shifting techniques are used to remove this ambiguity. In digital PIV, each image is divided into small areas called interrogation windows. Local displacement of the images of the seeding particles of the first and second illumination is determined for each interrogation window by statistical method (correlations mentioned above). Velocity vector fields are then computed provided the knowledge of the calculated displacement and the time delay between images (41).

The first application of PIV in IC engines was in 1989 by Reuss *et al*. (42). Velocity measurements were made in the clearance volume parallel to the piston using a double-pulsed laser sheet with 20-40 μs pulse separation. Images of the seeded flow were taken at CA 78 BTDC compression and CA 12 ATDC. Computed velocity fields were valid to within 500 μm of a surface. Out-of-plane vorticity components were evaluated at each point in the vector field by computing the circulation around a closed contour surrounding the point. The authors used this method instead of the first-order difference scheme to provide smoothing of the vorticity field. Three components of the strain rate tensor were evaluated from the first-order differences of the vector field at each point.

3.6 Literature Review on Near-Wall Velocity Measurements on IC Engines and the Structures of Turbulent Boundary Layer

Hall and Bracco (21) conducted LDV velocity and turbulence measurements near the cylinder wall of a non-firing and firing SI engine cycles operating with a swirl number of 4. The engine was fired every seventh cycle. Tangential velocity measurements were made in both firing and non-firing cycles at nine spatial locations with the closest being 0.5 mm from the cylinder wall. Radial velocity measurements were made at four of the nine locations with the closest component being 1.5 mm from the cylinder wall (Figure 3-5). Velocity measurements were made at the center of the clearance height (6.5 cm below the engine head.) in a single-cylinder research engine at operating speed of 1200 rpm. All measurements were made with one crank angle resolution from 42 degrees BTDC to 22 degrees ATDC. The seeding particles used were 1.5 μm diameter zirconium oxide (ZrO_2) which has good visibility in the burned gas and minimal window fouling; however, it was found to be abrasive.

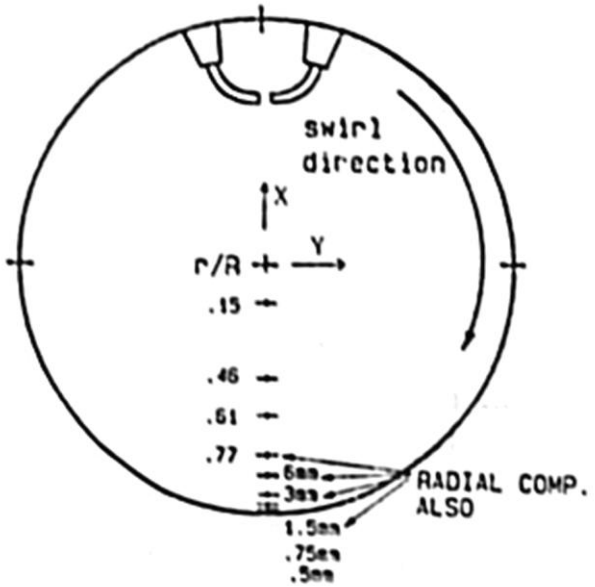

Figure 3-5: LDV measurement locations in the center of the clearance height (21).

Figure 3-6 shows the tangential ensemble averaged mean velocities in non-firing cycles at the nine radial locations for a number of crank angles near TDC. The flow exhibit a solid-body rotation until 1 cm from the wall where velocity decreases due to momentum diffusion to the wall. Boundary layer is evident as close as 0.5 mm to the wall. Figure 3-7 shows the tangential ensemble averaged mean velocities in firing cycles at the nine radial locations for a number of crank angles near TDC. The profiles are more complicated the non-firing case. There is noticeable increase in tangential velocity ahead of the flame at crank angles 350 and 355, and then a decrease as the flame passes before recovering due to the momentum of the swirling flow. The boundary layer is very thin in both the burned and unburned gas.

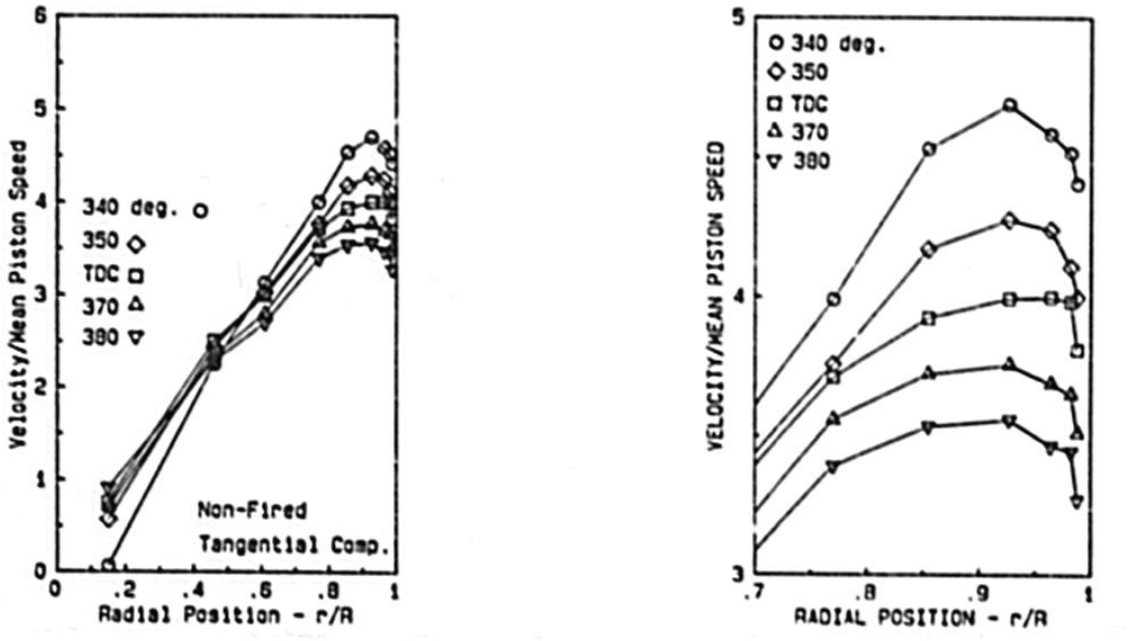

Figure 3-6: (left) Ensemble averaged mean velocity profiles measured in non-firing cycles, (right) Magnified view From Figure 3.5 (21).

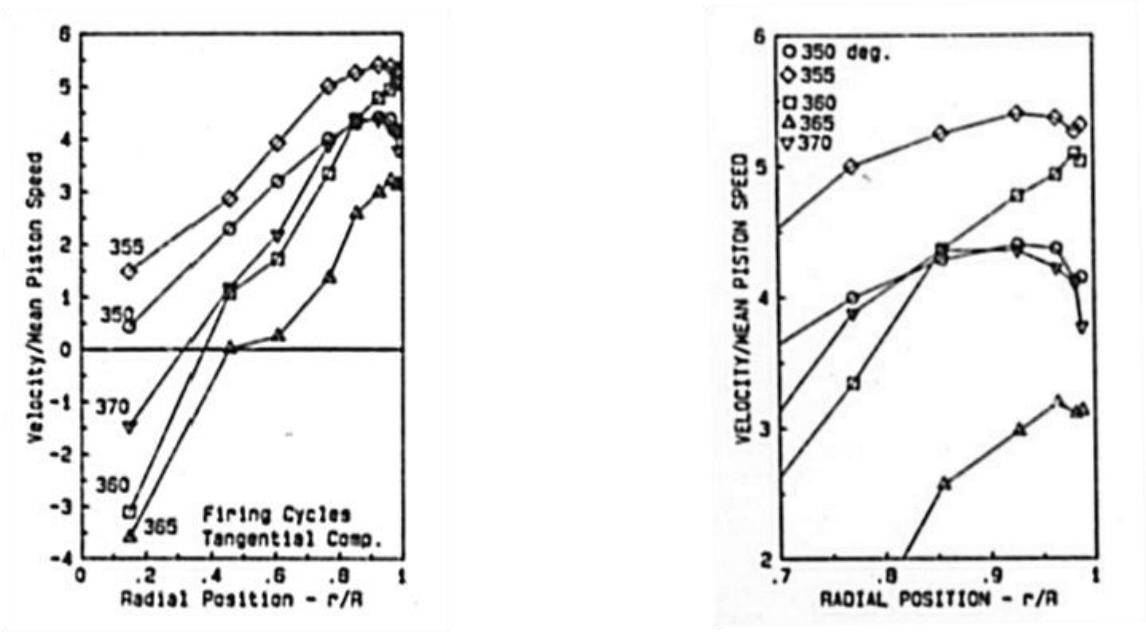

Figure 3-7: (left) Ensemble averaged mean velocity profiles measured in firing cycles, (right) Magnified view From Figure 3.6 (21).

Foster and Witze (43) carried out LDV velocity and turbulence measurements near the engine head wall in SI research engine. A special design toroidal contoured engine head with the apex at the half the radius of the cylinder was used to make it possible to get the LDV volume within 60 μm from the wall (Figure 3-8). Two levels of swirl were used to vary the flow Reynolds number. Boundary layer thickness less than 200 μm was observed in the high swirl motored operation case, and a boundary layer thickness of 700-1000 μm was noticed for the low swirl motored operation case. The boundary layer thickness increased when the engine was fired for both levels of swirl. Engine speed was 300 rpm and it was fired every fifth cycle. Velocity measurements 2 mm below the apex were made. These values were used as the characteristic free stream velocities to evaluate the Reynolds number with the radial position *r* as the characteristic length.

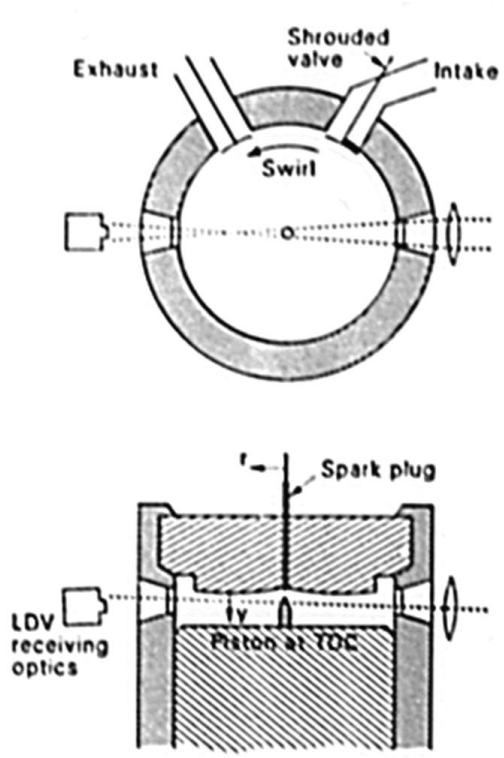

Figure 3-8: Schematic of the engine combustion chamber (43).

Figure 3-9 shows the velocity profiles in both the non-firing and the firing cycles of the high swirl case. For the non-firing cycles (top part of the Figure) the boundary layer effect could not be observed to within 70μm of the wall. However, velocity reduction starting 200μm from the wall is noticed after TDC. In the firing cycles (bottom part of the Figure), only measurements of the burned gas are shown. Measurements as close to 100μm were obtained; however, the authors suggest that these measurements at this distance should be discounted because of the erratic behavior mainly caused by beam steering. The boundary layer thickness increases after combustion is complete due to the drop in Reynolds number by a factor of more than three between pre-flame and post-flame flows.

Figure 3-10 shows the velocity profiles in both the non-firing and the firing cycles of the low swirl case. In the non-firing cycles, the boundary layer grows from 200μm to 1000μm during expansion as the outer flow stabilizes. The Y-axis is shifted for the firing case to account for the negative velocities recorded. The authors explain that since it is hard to justify negative velocities while the free stream is positive, they believe that beam steering is again causing problems.

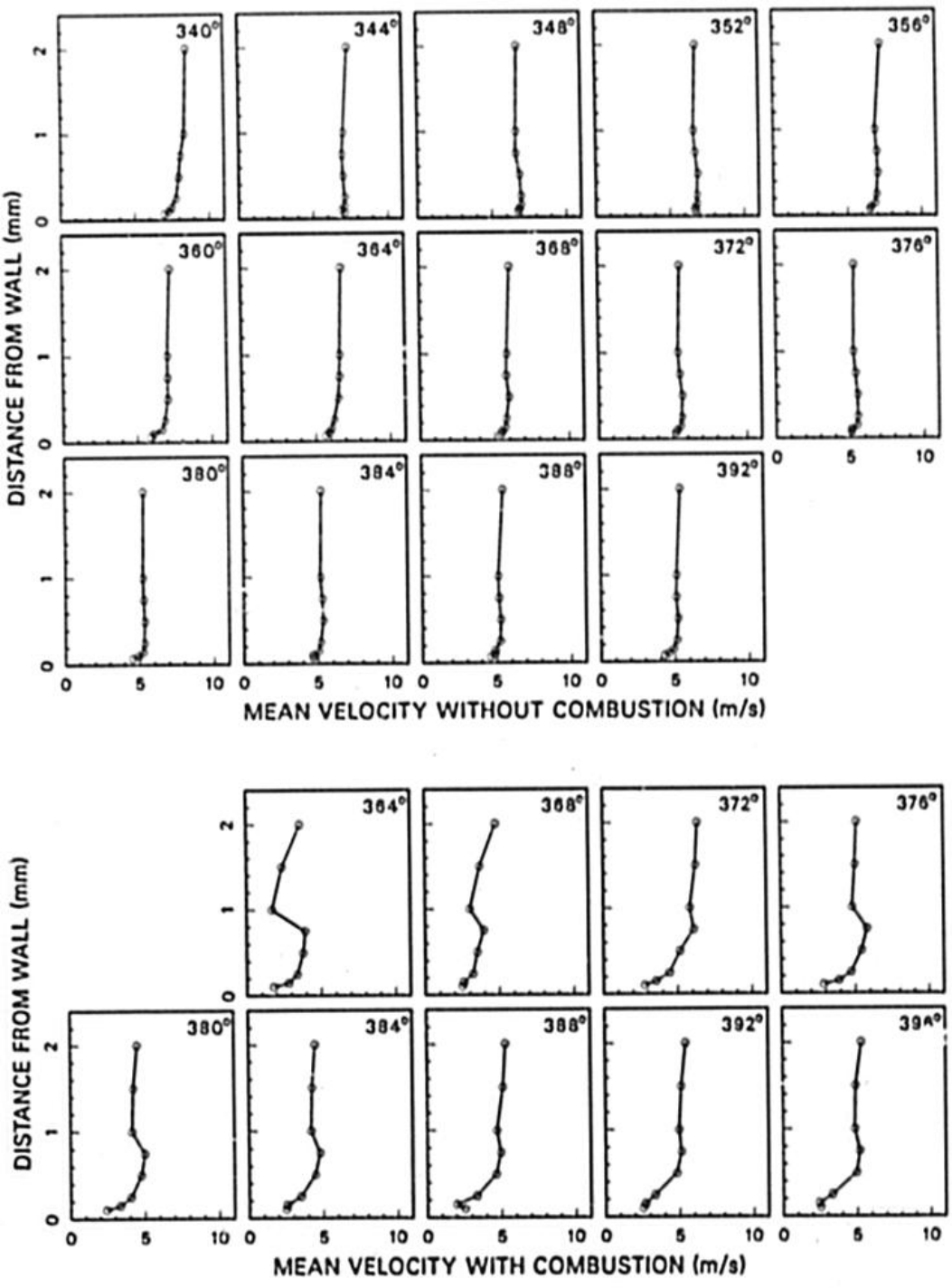

Figure 3-9: Boundary layer velocity profiles for the high swirl case (43).

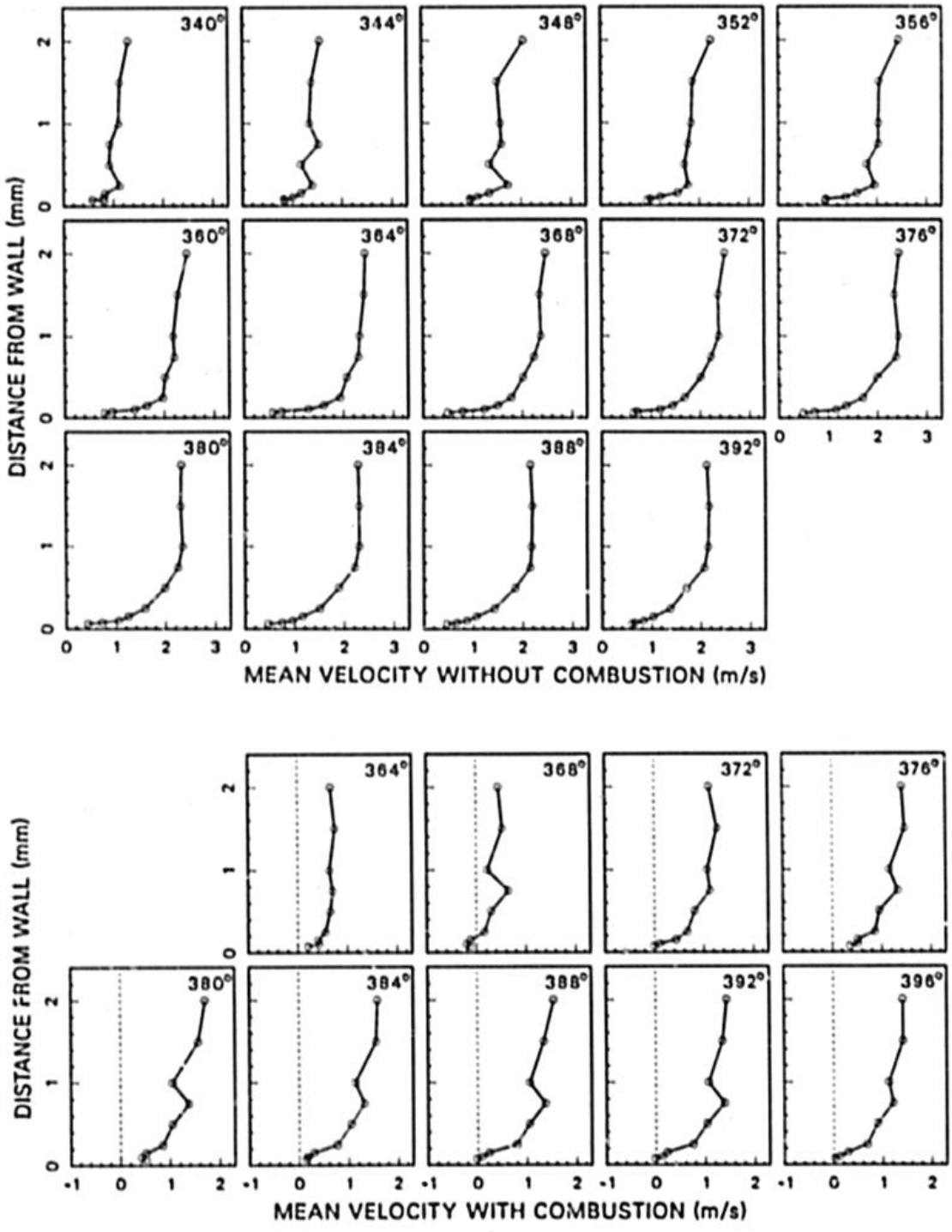

Figure 3-10: Boundary layer velocity profiles for the low swirl case (43).

Another boundary layer investigation was carried out by Pierce *et al*. (44), in which measurements of the near-wall velocity were made for several different engines cases. In this study, engines were setup to have realistic intake systems that included overhead valves and porting arrangements in order to have measurements of near-wall velocities in production-like engines. Five experiments were conducted; the first two applied LDV to measure velocity in a four stroke engine: the first one was near a protruding surface on the cylinder head, and the second one was near a flush surface on the cylinder head. The third experiment utilized multi-exposure particle images to visualize the flow near the cylinder wall on a two stroke disc shaped combustion chamber with no boost port. The fourth one is the same as the third one but with boost port. The Last experiment also used multi-exposure particle images to visualize the flow in a two stroke bowl-in-head combustion chamber with boost port.

Experiment 1: mean swirl velocity LDV measurement near a protruding surface on the cylinder head. The protruding surface is a plug with a cylindrical extension of 2 cm in diameter and 2 mm in depth. It was placed in the instrumentation port (Figure 3-11). Measurement were made for several different crank angles before and after TDC of the compression stroke for 750 rpm and 1500 rpm with the intake shroud oriented for maximum swirl. Measurements were taken to within 50 μm of the cylinder head wall. Near-wall velocities remain high and similar in magnitude to the core flow.

Experiment 2: individual swirl, radial, and axial velocity measurements near the flush surface of the cylinder head were made for a higher number of crank angles than

experiment 1 for 750 rpm and 1500 rpm for maximum swirl. Measurements were taken to within 400 μm of the flush cylinder head wall. Sample representation of the results is shown in Figure 3-12.

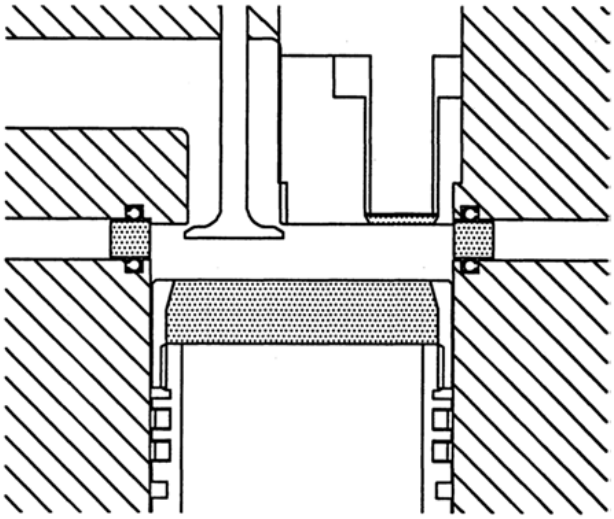

Figure 3-11: Schematic of the bottom view of cylinder head (top) and clearance volume (bottom) of the four stroke engine used for the LDV measurements in experiment 1 and 2 (44).

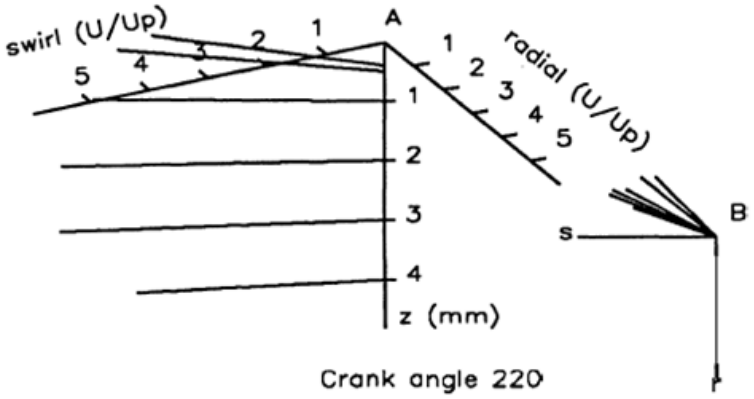

Figure 3-12: Velocity vectors for the 750 rpm high swirl case at 220 degrees (44).

Experiments 3, 4, and 5: Multi-exposure particle pictures were used as the primary technique used for flow diagnostics. Imaging plane was at half of the height of the clearance volume. Porting geometry and field of view for experiments 3 through 5 are shown in Figure 3-13. The boost port shown on the figure was not implemented on experiment 3 engine. Schematics of engine heads used for each of the three experiments are shown in Figure 3-14.

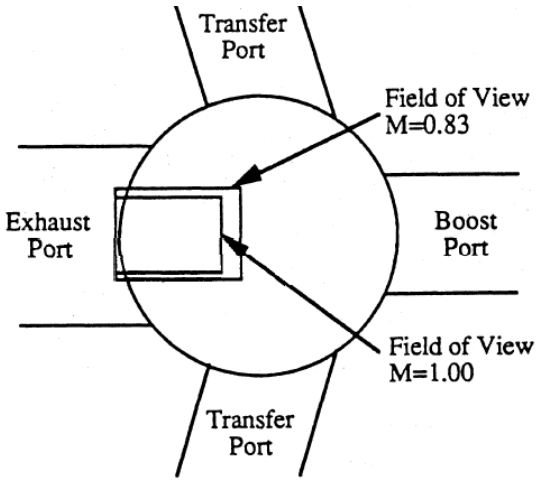

Figure 3-13: Porting geometry and field of view for experiment 3 (no boost port, M=0.83 and M=1.0), experiment 4 and 5 (with boost port, M=1) (44).

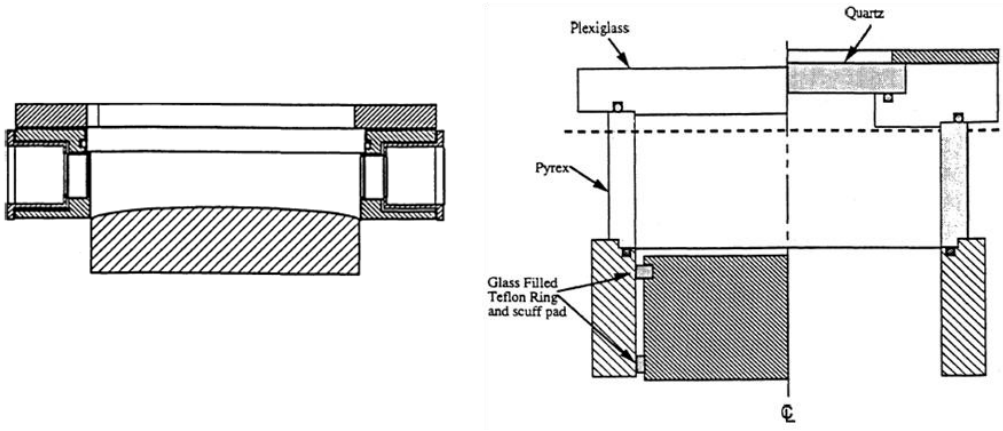

Figure 3-14: Schematic of head detail of the combustion chamber for experiment 3 (left), experiment 4 (left portion of the image on right), and experiment 5 (left portion of the image on right) (44).

The authors stated that the flow visualization results from experiment 3 show that the existence of well defined boundary layers in engines may be the unusual case. Rotational structures apparently persist all the way to the cylinder wall. Images were taken with five laser pulses at TDC with magnification of 0.833 and pulse separation of 80 μs, and at 25 degrees ATDC with magnification of unity and pulse separation of 120 μs. Engine speed in both cases was 750 rpm.

Experiment 4 was run at 500 rpm. Images were taken at TDC with a magnification of unity, varying only pulse separation timing from 80 μs to 120 μs. The engine used is similar to the one from experiment 3 with one modification of a boost port. It was concluded from these two runs that no organized mean flow was apparent and it only seemed as a decaying turbulent flow. The authors suggest that with the boost port, no typical boundary layer formation would be expected, and the transport of momentum, energy, and mass near the wall would be governed by the near-wall turbulent structures and their interaction with the wall.

Experiment 5 was run at 500 rpm. Images were taken at TDC with a magnification of unity and pulse separation of 120 μs. The same crank case was used with the addition of a bowl in the cylinder head to induce squish. The existence of an eddy right next to the wall surface was noticed.

It could be concluded from Pierce *et al*. (44) and Foster and Witze (43) that while LDV measurements can resolve boundary layers in IC engines are quite effective, they

lack the ability to be applied to a more realistic engine designs. Special arrangements and configurations have to be implemented in order to bring the LDV volume as close as possible to the surface of interest. The use of PIV instead of LDV would definitely eliminate this difficulty. PIV measurements would also provide an instantaneous two-dimensional flow field allowing investigating the boundary layer at different locations in one experiment, and extracting vortical structures as was noticed from experiment 5 in Pierce *et al*. (44).

A common characteristic of turbulent boundary layers is the generation of quasi-coherent vortex structures which have been an area of interest for many turbulence researchers in the past few years. These vortex structures within the boundary layer have a great impact on mass, momentum, and heat transfer near rigid boundaries in turbulent flows. Many explanations have been introduced about the evolution of these structures and an overview is presented by Davidson (24).

Kline et al. (45) carried out one of the earliest experiments studying coherent structures in turbulent boundary layers by visualizing hydrogen bubbles on a horizontal flat plate. Images showed that streaks of low speed fluid are quasi periodic in the spanwise direction of the flow. These slowly moving streaks were noticed to lift up in the buffer region and went through characteristic oscillations. The oscillations end rapidly as the lifted vortices break into small scale eddies, thus enhancing turbulence production. The process of ejecting slower fluid near the wall to an upper stream is called bursting. The upper stream decelerates causing a point of inflection in the velocity profile (S-

shaped velocity profile). Continuity requires counter flows from high flow layers to occur toward the wall in other regions; these flows are known as sweeps (26).

Boundary layer structures in steady flows have been the main focus of many studies, and little has been done on unsteady boundary layers. Costamagna *et al.* (46) in their DNS study of coherent structures in oscillatory boundary layers state that investigating turbulence structures in unsteady accelerating and decelerating flows may provide additional physical insight regarding the origin and development of wall turbulence. Furthermore, the study of coherent structures in oscillating or pulsatile flows is relevant to many science and engineering fields such as biofluid mechanics and oceanic and atmospheric sciences.

Kearney et al. (47) conducted a time-resolved thermal boundary layer structure investigation in a pulsatile reversing channel flow to study the impact of flow reversal on heat transfer from a heated flat plate to a partially and a fully reversing flow. It was found that in either case the effect of flow reversal was a dramatic thickening of the thermal boundary layer. They concluded that the main two reasons for the near-wall and bulk flow increase in temperature were the vertical ejection of fluid from the near-wall region, a phenomenon encountered in flow reversal, and the limited degree of turbulent transition. A subsequent dip in temperature following the rapid initial increase was noticed which was explained by a sudden fluid inrush (sweep) to preserve continuity, as discussed earlier. The wall heat transfer then recovers as the accelerated boundary layer flow clears the channel of high enthalpy fluid.

While the main purpose of the current research is to study velocity boundary layers, vortex structures were observed in the vector fields within the boundary layers. This shows an added benefit for applying μPIV for boundary layer investigations in IC engines. Future work of sampling vortex structures within the boundary layer could help in understanding heat transfer in IC engines, in addition to gaining more knowledge about wall turbulence in unsteady oscillating flows. However, the required high spatial and temporal resolution for such studies poses particular challenges for such studies in rapidly varying flows.

CHAPTER 4

PIV AND PTV PARAMETER OPTIMIZATIONS AND ERROR ANALYSIS

Following the brief description of PIV presented in section 3.2.2, it is important now to discuss several parameters that are relevant to PIV and are important in optimizing the experimental setup and reducing measurement uncertainty.

4.1 PIV Parameters

4.1.1 Imaging System

The imaging system parameters are shown in Figure 4-1. The magnification factor is determined by

$$M = \frac{z_0}{Z_0} \tag{3.1}$$

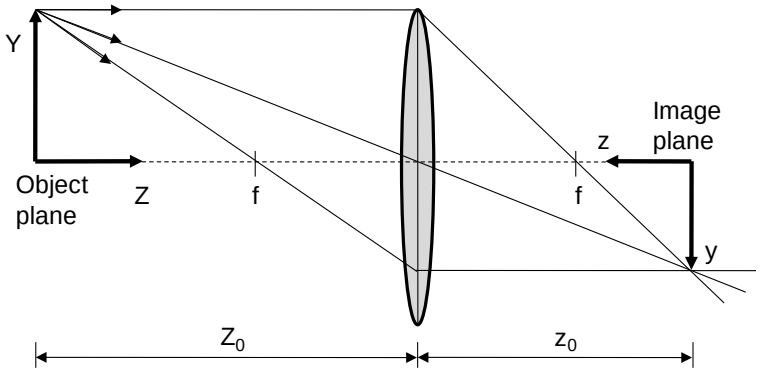

Figure 4-1: Geometric image construction.

The diffraction limited minimum image diameter is calculated by

$$d_{diff} = 2.44 f\#(M+1)\lambda \tag{3.2}$$

where *f*# is the f-number (or f-stop) defined as the ratio of the focal length of the lens and the aperture diameter, and λ is the laser wavelength. In some imaging tools, such as the long distance microscope used in this experiment, tabulated values of numerical apertures (*N.A.*) are provided based on the working distance (z_0). The f-number could then be determined as follows

$$f\# = \frac{1}{2N.A.} \tag{3.3}$$

The particle image diameter could be estimated using the following formula

$$d_\tau = \sqrt{\left(Md_p\right)^2 + d_{diff}^2} \tag{3.4}$$

where d_p is the seeding particle diameter. The depth of field is given by

$$\delta z = 2 f\#\, d_{diff} (M+1) / M^2 \tag{3.5}$$

4.1.2 Particle Image Shift

The flow speed is described by

$$u = \alpha \left(\Delta X / \Delta t \right) + \delta u \tag{3.6}$$

where α is the scaling or calibration factor that provides the physical amount of flow velocity and it is determined via calibration of the camera by simply placing a target with known spacing in the image plane (laser sheet plane). ΔX is the particle displacement (in pixels) detected by means of correlating particle patterns of two successive images separated by a known time interval Δt. δu is the uncertainty in velocity measurements. The time interval must be optimized such that the maximum particle displacement is not larger than one quarter the final interrogation window size (48)

$$\Delta s \leq \frac{1}{4} d_{IW} \tag{3.7}$$

where d_{IW} is the interrogation window size.

The measurement location and time are defined by the following two equations

$$x = \alpha\left[\left(X_s + X_e\right)/2 - X_0\right] \tag{3.8}$$

$$t = \left(t_s + t_e\right)/2 \tag{3.9}$$

where X_0 is the origin of the image plane, X_s and X_e are the starting and ending position of the correlation window, t_s and t_e are the first and the second laser pulse time.

4.1.3 Seeding Tracking

To analyze seeding constraints, i.e. evaporation and time response of the droplets in the flow, the in-cylinder temperatures have to be determined first. Temperature at the beginning of the compression stroke (180 CAD) is estimated to be equal to the intake air temperature set at 45 ºC. Pressure is acquired from a transducer located at the cylinder head that provides reading at every crank angle. Subsequent temperatures are determined for the compression stroke by applying the following isentropic relation for an ideal gas

$$\frac{T_2}{T_1} = \left(\frac{P_2}{P_1}\right)^{\frac{k-1}{k}} \tag{3.10}$$

where P is the cylinder pressure provided by the pressure transducer, k is the air specific heat ratio, and T is the in-cylinder temperature.

The air viscosity is determined from the Sutherland law (49) given by

$$\frac{\mu}{\mu_o} \approx \left(\frac{T}{T_o}\right)^{3/2} \frac{T_o + Su}{T + Su} \tag{3.11}$$

where μ is viscosity, μ_o is a reference value equal to 1.716E-5 N.s/m^2 for air, T_o is a reference temperature of 273 K for air, *Su* is the Sutherland constant and it has a value of 111 K for air.

The time response of the seeding particles is determined from

$$\tau_p = \frac{\rho_p d_p^2}{18\mu_a} \tag{3.12}$$

where ρ_p is the seeding particles density, d_p is their diameter, and μ_a is the air viscosity calculated using Equation (3.11). The seeding particles time response shall be compared with a number of time scales to determine how realistically those tracers follow the engine gas flow. The following analysis is adapted from (50).

The engine time scale is found by applying the following equation

$$\tau_e = \frac{S}{\bar{V}_p} \tag{3.13}$$

where *S* is the engine stroke and $\bar{V}_p$ is the piston mean speed. The engine time scale, τ_e, describes the effect of time varying boundary conditions on the flow variation rate.

The turbulent turn-over time scale is given by

$$\tau_t = \frac{L}{u'_{rms}} \tag{3.14}$$

where L is the length scale of the most energetic eddies, u'_{rms} is the fluctuation intensity defined as the root mean square of the fluctuation velocity (see section: Mean Velocity and Turbulence Characteristics). Following the analogy of Lumley (3), L is estimated to be 1/6 the largest possible eddy which is approximated to be the clearance height, and u'_{rms} is approximated to be the piston mean speed for the first half of the compression stroke, and half the piston mean speed for the second half of the compression stroke.

The resolved eddies turn-over time scale is given by

$$\tau_\Delta = \tau_t \left(\frac{\Delta}{L} \right)^{2/3} \tag{3.15}$$

where Δ is twice the final grid spacing of the applied algorithm and must be above estimates of ~10 μm for the Kolmogorov scale in engines (3).

Engine time scale, turbulent turn-over time scale, and resolved eddies turn-over time scale should be compared to the time response of the seeding particles by means of the *Stokes* number given by

$$St = \frac{\tau_p}{\tau} \tag{3.16}$$

where τ is the corresponding time scale, i.e. engine time scale, turbulent turn-over time scale, and resolved eddies turn-over time scale.

4.1.4 Particle Image Density

Optimum seeding density is required when conducting a PIV experiment in order to obtain a high valid detection rate and a low measurement uncertainty. Keane and Adrian (48) and (51) in their Monte Carlo simulations recommend that the seeding density should be optimized to produce 15 or more particle images per interrogation spot.

Megerle *et al*. (52) experimentally investigated the effect of particle image counts among other factors (i.e. f-stop, magnification, and focusing) on the accuracy and precision of digital PIV. A minimum RMS error of 2% was obtained for particle image count of 10 within a 32x32 interrogation window. Higher seeding counts did not seem to give an advantage regarding accuracy since the measured fluctuations of the particle images displacements were found to be independent in the range of 10-40 particle images within the 32x32 interrogation window.

A major difficulty in conducting μPIV is meeting the optimum particle image count (~10 image particles per interrogation window). One of the recommended solutions for low seeding density is to process the data applying an ensemble averaged correlation (32), or overlaying a number of raw (unprocessed) images to produce one image with

higher density (41). While the first option seems plausible, it only produces and ensemble averaged flow field, thus losing a lot of valuable statistics and the ability to calculate different turbulent terms. The second option on the other hand seems reasonable to be used if the flow under investigation is laminar.

The third option is combining PIV and PTV in a hybrid scheme where PIV serves as a predictor of the flow field and the PTV algorithm corrects for it. The predictor PIV algorithm could use larger interrogation window size (i.e. 64x64 pixels) to increase the number of seeding particles by a factor of 4, thus increasing the valid detection rate and decreasing measurement uncertainty. The PTV algorithm then tracks individual particles between the two images with the guidance of the PIV predicted flow filed. More description of the hybrid algorithm is provided in the data processing section of Chapter 5.

4.2 Error Analysis

In addition to the systematic (bias) error, random error that is due to measurement uncertainty should also be taken into account.

4.2.1 Systematic Error

Systematic (bias) error is caused by the statistical method of cross-correlation and the subsequent post-processing schemes. Using different algorithms to process and post-process PIV images will result in different levels of accuracy (53). In the second international PIV Challenge (53), the PIV algorithm provided by the LaVision team (software used in current research to process the PIV images) had a bias error of 0.113

pixels when tested for a hundred synthetic images of a turbulent channel flow. The PTV algorithm provided by LaVision which uses their own PIV scheme as a predictor performed the best among other PTV team with a bias error of 0.2 pixels. It was noticed in the challenge that PTV algorithms in general outperformed PIV ones in near wall velocity analysis due to the reduced effect of the wall bias on the interrogation windows.

4.2.2 Random Errors

Random errors induced by measurements could be evaluated by determining RMS deviation from the mean. This method cannot be implemented to the results of the current experiment since the RMS deviation from the mean includes turbulence fluctuations and cycle to cycle variations. Therefore the sources of measurement uncertainty shall be investigated by breaking the PIV experimental setup down into sub-systems and investigating each sub-system for possible errors. Error sources and their propagation are detected following the recommended procedures and guidelines of the 25th International Towing Tank Conference (54). Below are the error sources corresponding to calibration α, displacement of particle image ΔX, time interval Δt, and seeding velocity lag.

4.2.2.1 *Calibration* (α)

The calibration is conducted by placing a calibration plate of a known spacing in the object plane (laser sheet plane) as shown in Figure 4-2. The scaling or calibration factor (α) (also known as the magnification factor, a term that is not used here to avoid confusion with the imaging magnification M) is given by

$$\alpha = \frac{l_r \cos\theta_1}{L_r}, \quad \left[\text{mm / pixel}\right] \tag{3.17}$$

where l_r is the distance between the reference points on the calibration plate, L_r is the corresponding distance on the image plane, θ_1 is the angle between the light sheet and the calibration plate.

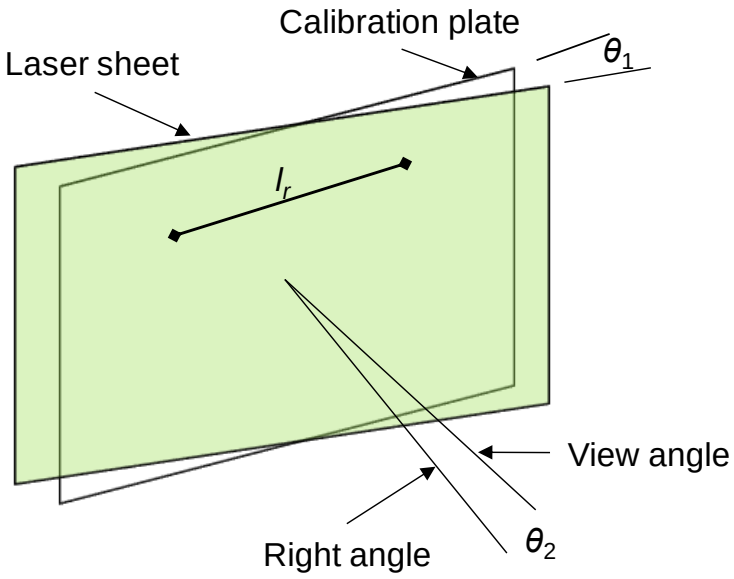

Figure 4-2: Calibration plate positioning in the laser sheet plane (image plane).

Calibration board: Image distance of reference points L_r

The position of the reference points is determined from single pixel leading to an uncertainty band of 0.5 pixels. Since two points are involved in determining L_r, the total uncertainty will be 0.7 pixels. The sensitivity factor (the partial derivative of Equation (3.17)) is

$$\frac{\partial\alpha}{\partial L_r} = -\frac{l_r \cos\theta_1}{L_r^2}, \quad \left[\text{mm / pixel}^2\right] \tag{3.18}$$

Calibration board: Physical distance of reference points l_r

The error of the 1.2 mm spaced calibration plate is estimated to be 0.001 mm. The sensitivity factor of l_r is

$$\frac{\partial \alpha}{\partial l_r} = -\frac{\cos\theta_1}{L_r}, \quad [1/\text{pixel}] \tag{3.19}$$

Optical system: Image distortion

Image could be distorted by lens aberration which affects the accuracy of calibration factor. No data is available for the lenses used in the experiments regarding their distortion percentage due to aberration. In general, the error will be distortion percentage times L_r, and the sensitivity factor is the same as Equation (3.18).

Optical system: CMOS distortion

No data is available regarding the amount of distortion of the CMOS chip used. According to the uncertainty procedure adapted here (54), this error is usually small and can be neglected.

Experimental condition: Calibration plate position

The difference between the position of the laser sheet and the calibration plate could affect the accuracy of the measurements. The uncertainty band could be estimated to be the depth of field (see Equation (3.5)). For the sensitivity factor, the pinhole camera model is assumed and α could be described as

$$\alpha = \frac{l_r \cos\theta_1}{L_r} = \frac{z_0}{f} \tag{3.20}$$

where z_0 is the working distance shown in Figure 4-1, and f is the focal length. The sensitivity factor will be

$$\frac{\partial \alpha}{\partial z_0} = \frac{l_r \cos\theta_1}{L_r z_0}, \quad [1/\text{pixel}] \tag{3.21}$$

Experimental condition: Parallel calibration plate

The angle θ_1 between the laser sheet and the calibration plate could be estimated by

$$\theta_1 = \sin^{-1}\left(\frac{\delta z}{x_{total}}\right) \tag{3.22}$$

where δz is the depth of field, and x_{total} is the width of the field of view. The sensitivity factor is

$$\frac{\partial \alpha}{\partial \theta_1} = -\frac{l_r \sin\theta_1}{L_r}, \quad [\text{mm/pixel}] \tag{3.23}$$

4.2.2.2 *Displacement of Particle Image* (*ΔX*)

Errors due to particle displacement are categorized as follow:

Visualization: Laser power fluctuation

The maximum error could be estimated as the seeding particle diameter (1 μm). In well controlled experimental conditions, error could be reduced to 1/10 of the particle diameter. Since the displacement is obtained from two particle images, the error band is estimated as Δx = 0.14 μm, and the sensitivity factor obtained from Equation (3.8) is

$$\frac{\partial X}{\partial x} = \frac{1}{\alpha}, \quad [\text{pixel} / \text{mm}] \tag{3.24}$$

Optical system: Lens and CMOS distortions

Lens and camera chip (CMOS) distortion were discussed earlier on their effect on calibration. The former was not accounted for due to lack of data, and latter was assumed negligible.

Optical system: Normal view angle

Deviation from the ideal right angle between the camera setup and the laser sheet plane (θ_2 in Figure 4-2) and its sensitivity factor are estimated in a similar manner as for θ_1.

Data processing

Error inherited from data processing is the systematic error discussed earlier.

4.2.2.3 *Time Interval* (Δt)

The sources of error associated with laser timing are discussed below. The sensitivity factor for the time measurement is 1.

Delay generator

The high speed controller (HSC) provided by LaVision controls the timing of the camera and laser. It receives two signals from the engine encoder which are a signal per cycle (PPC) and a signal per crank angle degree (360°), and outputs triggering signals to the laser and camera. According to the user manual, the jitter is less than 1 ns.

Laser pulse timing accuracy

The laser used has a 5 ns jitter in pulse timing. The signal to pulse delay is about 3 μs.

4.2.2.4 *Seeding Velocity Lag* (δu)

The error induced by seeding velocity lag could be estimated from the Stokes number that corresponds to the turbulent turn-over time scale. Stokes number (in %) is multiplied by the velocity u to give the uncertainty caused by seeding velocity lag (δu).

The combined uncertainty for each parameter is then calculated using the general formula for error propagation given by

$$\delta_c = \sqrt{\left(c_1\delta_1\right)^2 + \left(c_2\delta_2\right)^2 + ... + \left(c_i\delta_i\right)^2} \tag{3.25}$$

where c_i is the sensitivity coefficient obtained from partial derivatives, and δ_i is the uncertainty band.

The effect of the combined uncertainty for each parameter on the velocity is calculated by multiplying each one by its corresponding sensitivity factor which is derived from Equation (3.6) as follows:

1) Calibration, $c = \partial du/\partial \alpha = \Delta X/\Delta t = u/\alpha$

2) ΔX, $c = \partial u/\partial(\Delta X) = \alpha/\Delta t$

3) Δt, $c = \partial u/\partial(\Delta t) = -\alpha \Delta X/(\Delta t)^2 = u/\Delta t$

CHAPTER 5

LOW AND HIGH RESOLUTION PIV EXPERIMENTS NEAR THE CYLINDER HEAD

This chapter presents high-speed PIV measurements of the boundary layer flow at a production-type four-valve pent-roof cylinder head of a spark ignition direct injection engine. Two experiments were conducted; one at a low spatial resolution and high temporal resolution of 4.8 kHz (imaging at every crank angle) utilizing PIV to get a general overview of the flow behavior near the cylinder head during the compression and expansion strokes. In the second experiment, PIV and Particle Tracking Velocimetry (PTV) were applied to measure two-dimensional near-wall velocity fields at the cylinder head at 2.4 kHz. To achieve the spatial resolution that is required to resolve important structures of the boundary layer, a long distance microscope was used to image Mie scattering signals onto a CMOS camera. Results are reported with a spatial resolution of 45 μm as close as 22 μm from the wall for measurements during the compression and expansion strokes in a motored engine. This study presents the first step towards a complete characterization of dynamic boundary layers in internal combustion engines. In addition to the flow properties, in a second step the temperature distribution in the gas phase and on the surface will have to be simultaneously measured as well. This can be achieved with laser-induced fluorescence (55) and phosphorescence imaging (56).

5.1 Experiment

5.1.1 Setup

The experiment was conducted in a four-stroke, single cylinder, four-valve spark ignition direct injection optical engine. The engine head is pent-roof shaped with a spark plug located on the exhaust valves side and the eight-hole injector located on the intake valves side oriented in a way that part of the injection is aimed at the spark plug. The intake system consists of a bulk flow port and a tangential port. The bulk flow port could be closed to create a high level of swirl rated at 5.5 swirl ratio. In this experiment, the bulk flow valve was left open providing a 0.8 swirl ratio. Engine specifications are shown in Table 5.1. The optical components of the engines are transparent quartz cylinder, two flat quartz windows located at both sides of the pent-roof combustion chamber, and quartz windows located on the top and sides of the piston (Figure 5-1). For this experiment, imaging was carried out through the flat pent-roof windows. The field of view is in the tumble flow plane at the cylinder head between the spark plug and the fuel injector as shown in Figure 5-1 and Figure 5-2.

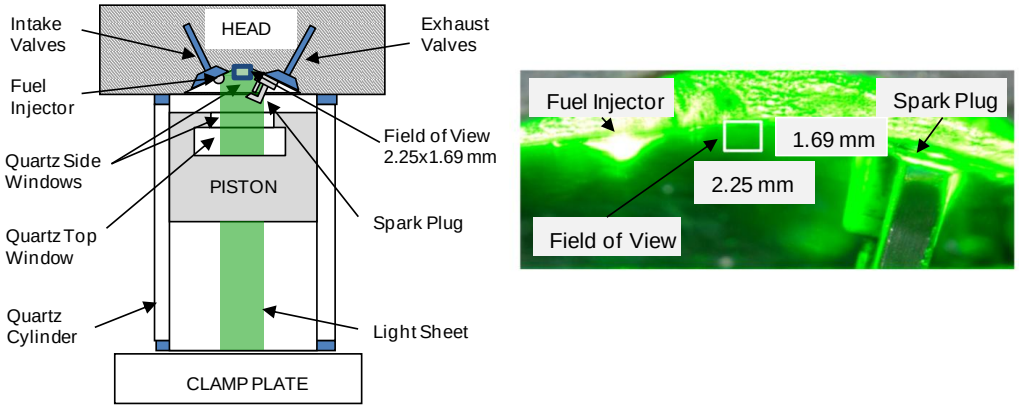

Figure 5-1: Schematic of the optical SIDI engine. Field of view shown on the right image is for the high resolution experiment. The low resolution measurements cover the entire area between the spark plug and the fuel injector.

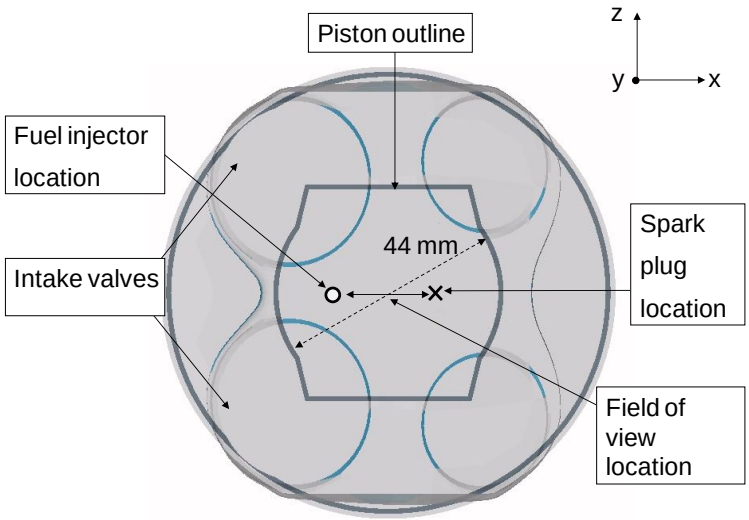

Figure 5-2: Light sheet position on the cylinder head between spark plug and injection, viewed from bottom of the engine (57). Indicated field of view location is for the low resolution experiment. The high resolution field of view is within the range shown as in the right of Figure 5-1.

Table 5.1: Optical SIDI engine specifications. Note: valves timings are with 0.1 mm lift.

Connecting Rod	159 mm
Bore	86 mm
Stroke	86 mm
Displacement	500 cm^3
Compression Ratio	9.0:1
Intake Valve Open (IVO)	717 CAD
Intake Valve Close (IVC)	231 CAD
Exhaust Valve Open (EVO)	497 CAD
Exhaust Valve Close (EVO)	12 CAD
Engine Speed	800 RPM
Intake Pressure	95 kPa
Intake Temperature	45 ºC

A dual oscillator single head 527 nm Nd:YLF laser (Quantronix Darwin-Duo) was operated at a frequency of 4.8 kHz and 5.5 mJ/pulse for the low spatial resolution experiment and at 2.4 kHz and 17 mJ/pulse for the high spatial resolution experiment. Time separation between laser pulses was optimized to best meet the maximum

displacement value of 1/4 (or less) the interrogation window size suggested by Keane and Adrian (48).

Since maximum velocity within the field of view varies throughout the compression and expansion strokes, variable time separation would be a good feature to fulfill the maximum displacement value of 1/4 the interrogation window size criterion. However, with the lack of ability to vary time separation as function of CAD during image recording, it was chosen to satisfy the maximum displacement for a wide range of crank angle degrees. Displacement was less than the recommended maximum displacement for the rest of crank angle degrees intervals which still meets Equation (3.7) , except for the first four crank angle degrees of the compression stroke where displacement was higher and on the order of 1/3 of the interrogation window size, which according to Keane and Adrian (48) represents an upper limit after which the valid detection rate declines sharply. For the low resolution experiment with a final interrogation window of 32x32 pixels and pulse separation of 35 μs, the displacement was between 6 to 8 pixels for most of the compression stroke and 2 to 5 for the expansion stroke before the exhaust valves open. A maximum displacement of 12 pixels was recorded at the beginning of the compression stroke. For the high resolution μPIV+PTV experiment with a final PIV interrogation window of 64x64 pixels and pulse separation of 15 μs, the displacement was between 6 to 16 pixels for most of the compression stroke and 4 to 10 for the expansion stroke before the exhaust valves open. A maximum displacement of 20 pixels was recorded at the beginning of the compression stroke.

Imaging through thick windows can lead to aberrations that limit the use of PIV in engines (58). Static imaging tests through the 18 mm thick, flat side window in the cylinder head produced high quality Mie scattering images from the seed droplets, even when using the long distance microscope. For the low resolution experiment, a 105 mm 1:2.8D lens (Sigma DG Macro) was used to image Mie scattering signals onto the camera chip. The f-number was set to 11. For the high resolution μPIV experiment, a long distance microscope (Questar Corporation QM 100) was used to collect the Mie scattering. The long distance microscope has a working distance ranging from 150 mm to 380 mm. In this experiment, it was set at a distance of 190 mm which gave a numerical aperture NA = 0.128. The f-number was then determined from Equation (3.3) to be 3.9. For both experiments, the camera was calibrated using a mm-spaced resolution target giving a calibration factor of 21.43 μm/pixel and a magnification M = 1 for the low resolution experiment and a calibration factor of 2.82 μm/pixel and a magnification M = 7.8 for the high resolution experiment. The PIV velocity measurements for the low resolution experiment based on a 32x32 interrogation window with 50% overlap produced a vector every 343 μm and the PIV+PTV velocity measurements for the high resolution experiment based on a 64x64 interrogation window with 50% overlap for the PIV part and a final 16x16 grid reconstruction after the PTV part produced a vector every 45 μm.

Details of the experimental setup are shown in Figure 5-3. Laser beams were reflected by a HR532 45º mirror and then passed through a telescope to expand them into

laser sheets. The two overlapping light sheets were reflected upward by a 45º mirror sending the light sheet through the piston top window to illuminate the tumble plane.

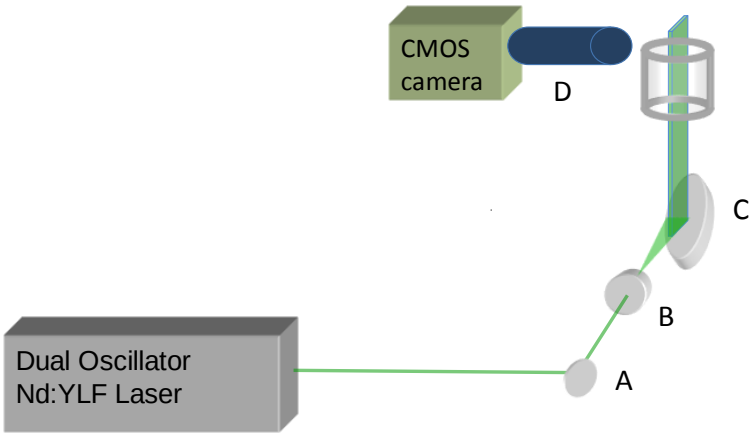

Figure 5-3: A) HR532 mirror, B) telescope lens, C) 45º mirror, D) long distance microscope.

A summary of the PIV parameters is shown in Table 5.2.

Table 5.2: PIV parameters.

Parameter	Low Resolution	High Resolution
Light sheet thickness	1 mm	1 mm
Field of view	9.94x10.63 mm^2	2.25x1.69 mm^2
Magnification	1.0	7.8
f-number	11	3.9
Depth of field	1.25 mm	50 µm
Vector spacing (16x16 grid spacing)	343 µm	45 µm

Heat resistant, high flash point, low volatility phenylmethyl polysiloxane silicone oil droplets (Dow Corning® 510) as PIV seeding were produced using one jet of a six-jet atomizer (TSI Model 9306). The seeding density was controlled via a pressure regulator attached to the atomizer and the droplet stream was added to the combustion chamber

through the intake plenum. Mie scattering signals from the seeding particles were recorded by a high-speed 14-bit CMOS camera (Vision Research Phantom 7.3) equipped with 16 GB onboard memory. At 2.4 kHz, the camera could use the full chip with 800x600 pixels.

Seeding constraints analysis, i.e. evaporation and time response of the droplets in the flow, was performed following the procedure shown in Chapter 4, section 1 (Equation (3.10) to Equation (3.16)). Temperature at the beginning of the compression stroke (180 CAD) was estimated to be equal to the intake air temperature set at 45 ºC. Pressure was acquired from a transducer located at the cylinder head that provides reading at every crank angle. A maximum temperature of 456 ºC was determined at 357 CAD. From the silicone oil manufacturer specifications, the autoignition temperature is estimated to be 482 ºC and the percentage of volatile content by weight after 4 hours at 250 ºC is 2.5 at atmospheric pressure. These figures rule out significant evaporation of the seed droplets. This was confirmed during preliminary tests where strong Mie scattering images were obtained throughout the expansion stroke, after the droplets were already exposed to the highest in-cylinder temperature.

Table 5.3 shows the different time scales at different crank angle degrees. Engine time scale, turbulent turn-over time scale, and resolved eddies turn-over time scale were compared to the time response of the seeding particles by means of the *Stokes* number (Equation (3.16)).

Table 5.3: Particle time scale, flow time scales, and the corresponding Stokes number as a function of CAD.

	τ_p (s)	τ_e (s)	St_e	τ_t (s)	St_t	τ_Δ (s)	St_Δ
180 CAD	$2.85x10^{-6}$	$3.76x10^{-2}$	$7.60x10^{-5}$	$7.04x10^{-3}$	$4.05x10^{-4}$	$2.22x10^{-4}$	$1.29x10^{-2}$
225 CAD	$2.79x10^{-6}$	$3.76x10^{-2}$	$7.42x10^{-5}$	$6.34x10^{-3}$	$4.40x10^{-4}$	$2.14x10^{-4}$	$1.30x10^{-2}$
270 CAD	$2.45x10^{-6}$	$3.76x10^{-2}$	$6.54x10^{-5}$	$4.34x10^{-3}$	$5.65x10^{-4}$	$1.89x10^{-4}$	$1.30x10^{-2}$
315 CAD	$1.95x10^{-6}$	$3.76x10^{-2}$	$5.19x10^{-5}$	$3.82x10^{-3}$	$5.10x10^{-4}$	$2.87x10^{-4}$	$6.80x10^{-3}$
360 CAD	$1.61x10^{-6}$	$3.76x10^{-2}$	$4.29x10^{-5}$	$1.56x10^{-3}$	$1.03x10^{-3}$	$2.13x10^{-4}$	$7.57x10^{-3}$

5.1.2 Data Acquisition

The lasers and camera were synchronized via a USB high-speed controller (HSC, LaVision). The controller receives a signal each crank angle degree from the engine encoder, and a signal every cycle (720 degrees) from a hall-effect sensor. Double frame images with time separation of 35 μs for the low resolution experiment and 15μs for the high resolution experiment one were recorded. For the low resolution PIV experiment, images were recorded every crank angle degree during the compression and expansion strokes from 180 CAD to 489 CAD with 360 being TDC compression. For the high resolution PIV and PTV experiment, images were obtained every other crank angle degree during the compression and expansion strokes from crank angle 180 to 540. It should be noted that the high resolution results will only be shown from 180 to 490 CAD because the high velocity increase once the outlet valves opened made velocity calculations impossible with the minimum possible time delay between the lasers provided by the high speed controller.

At the beginning of each run, images were recorded with the laser sheet only (no seeding) for ten cycles. These unseeded images were then averaged and used to determine a threshold level for the local noise intensity coming from the camera chip and the bright reflections from solid objects, which in current experiment were mostly reflections off the cylinder head. Those reflections were reduced prior to the experiment by applying a flat black paint (Krylon® *Short Cuts*® paint pen) at the boundary of interest. This helped reducing the intensity of the cylinder head glare by 84%. The average intensity of the high resolution background is 600 counts, for the low resolution measurement it is 300 counts compared to a dynamic range of the camera of 16,384 counts (14 bit).

5.1.3 Data Processing

Double-frame images were processed using commercial software (LaVision Davis 7.2)**.** In addition to the background subtraction described in the previous paragraph, other pre-processing procedures were applied to further filter out noise. Beside the common noise of camera chip and bright reflections from solid objects, which are usually encountered in PIV, a stationary fixed fringe pattern was a dominant source of noise in the high resolution experiment. By investigating the experiment setup components by a process of elimination, it is believed that the camera chip is the source of this fringe. Monochromatic light can cause a fringe pattern produced by the interference between light waves that reflects within the CMOS chip creating what is known as Newton's rings (59). A batch operation was executed on each crank angle series to calculate the minimum intensity value at all pixel positions. Then this pixel-specific minimum is

subtracted from all images in the series. A stationary fixed pattern such as the fringe intensity adds to the particle images intensities, and the minimum intensity value at a certain position is the background intensity of the fringe intensity when no particle intensity is added to the background. Since the seeding density is low enough, statistically, this procedure effectively eliminates the fringe pattern. Then a non-linear sliding minimum filter of pixel size 10 was used before cross-correlating the double frame images. This high pass filter removes the local mean background intensity (over a scale of the specified number of pixels) leaving only the local fluctuations, i.e. the smaller-sized particle images that were on the order of 8 pixels in diameter.

The evaluation of PIV images requires sufficient seeding density, typically 8-10 seeding particles per interrogation window, in order to obtain reliable and accurate results. Seeding density was sufficient for the low resolution experiment; however, seeding density is usually low in μPIV and here also due to the proximity of the surface. In the high resolution experiment, seeding density was 1 to 3 particles per a 32x32 interrogation window. An alternative to using a PIV algorithm for low density images is particle tracking velocimetry (PTV) where velocity is determined by tracking individual particles.

A hybrid PIV+PTV method was applied to evaluate the double frame images obtained in the high resolution experiment. The evaluation starts with a standard PIV algorithm to determine a “predictor” velocity field. PIV vector field computations were processed starting with a 128x128 pixel interrogation window and decreased by half to a

final size of 64x64 pixels instead of the 32x32 pixels intended for the PIV evaluation only in the case of the low resolution experiment; the 50% window overlap was maintained. With the new larger window size, the seeding count is 4 to 12 particles per interrogation window, hence increasing the reliability of the PIV calculations, keeping in mind that gradients within the increased interrogation window might have an effect on the velocity vector value. However, since the PIV results are used as a predictor-only for PTV, the window size will not have an impact on the accuracy of the final velocity field. A standard deviation filter was applied to remove spurious vectors and a mean of adjacent vectors was used to replace those vectors. The resolution of the vector field was then further refined by detecting and tracking individual particles by the PTV algorithm, which increases the number of vectors per PIV interrogation window from one to the total number of particles per same window. The particle detection method adapted in *DaVis* looks for the position of the highest intensity and arranges an interrogation window (not to be confused with the PIV interrogation window) of the size of the particle diameter around the position of the maximum intensity. The PTV interrogation window in the second frame is shifted by the "predictor" vector from the PIV calculations. Finally, an individual particle correlation will correlate the intensity pattern of both windows to determine the exact shift. The same post processing median filter applied to the PIV results was also applied to the PTV results. A final step of converting the vector field to a 16x16 pixel grid was then applied using a second order polynomial fit (60) and (32).

5.2 Measurement Uncertainty

Uncertainty analysis was carried out following procedure shown in Chapter 4, section 2. For the high resolution experiment, l_r = 1.2 mm and L_r = 426 pixel. The calibration factor is therefore equal 0.0028 mm/pixel. θ_1 and θ_2 both estimated to be 0.022 rad.

Table 5.4 summarizes all terms discussed in the error analysis section of the previous chapter. For the error caused by the particle lag, Stokes number that corresponds to the turbulent turn-over time scale at 270 CAD is multiplied by a velocity of 1.5 m/s which is the maximum velocity obtained for a wide range of crank angle degrees from the high resolution experiment. It should be noted that the velocity chosen is for demonstration purposes, and detailed calculations should take velocity variation along the boundary layer profiles into account.

Table 5.4: Summary of uncertainty terms for the high resolution experiment.

Parameter	Category	Error sources	Uncertainty band (δ_i)	Sensitivity factor (c_i)	c_i x δ_i	Combined uncertainty (δ_c)
α (mm/pix)	Calibration	Reference image Physical distance Calib. pl. position Parallel calib. pl.	0.70 (pix) 0.001 (mm) 0.05 (mm) 0.022 (rad)	-6.6E-6 (mm/pix) 2.4E-3 (1/pix) 1.5E-5 (1/pix) -6.2E-5 (mm/pix)	4.6E-6 2.4E-6 7.5E-7 1.4E-6	5.4E-6
ΔX (pix)	Acquisition	Laser power fluct. Normal view angle	1.4E-4 (mm) 0.022 (rad)	357 (pix/mm) -6.2E-5 (mm/pix)	0.05 1.4E-6	0.206
	Systematic	PIV+PTV algorithm	0.2 (pix)	1.0	0.2	
Δt (s)	Acquisition	Delay generator Laser jitter	1E-9 (s) 5E-9 (s)	1.0 1.0	1E-9 5E-9	5E-9
δu (mm/s)	Experiment	Particle lag	0.85 mm/s	1.0	0.85	0.85

The effect of combined uncertainties for each parameter on the velocity is obtained following the steps shown at the end of Chapter 4. The results are shown in Table 5.5.

Table 5.5: Combined velocity uncertainty

Parameter	δ_i	c_i	c_i x δ_i
α	5.4E-6 (mm/pix)	535714 (pix/s)	2.9
ΔX	0.206 (pix)	187 (mm/pix/s)	38.5
Δt	5E-9 (s)	1E8	0.5
Δu	0.85	1.0	0.85
Combined uncertainty			38.6 (mm/s) = 2.6%

5.3 Results and Discussion

The flow field near the cylinder head was first measured with low resolution data over 136 motored cycles from 180 to 329 CAD, and 128 cycles from 330 to 489 CAD with a signal to background ratio in the raw images of around 5.8. The low-resolution data show the larger scale features of the flow near the cylinder head and help to understand details of the high-resolution flow, including a reversal of the flow direction and the role of spatial gradients in horizontal direction. Figure 5-4 shows excerpts from this crank angle sweep. Overall the flow during the intake and compression strokes shows a strong, clockwise tumble feature. After top-dead center, however, a slowing of the near-wall flow and reversal of the flow direction is observed.

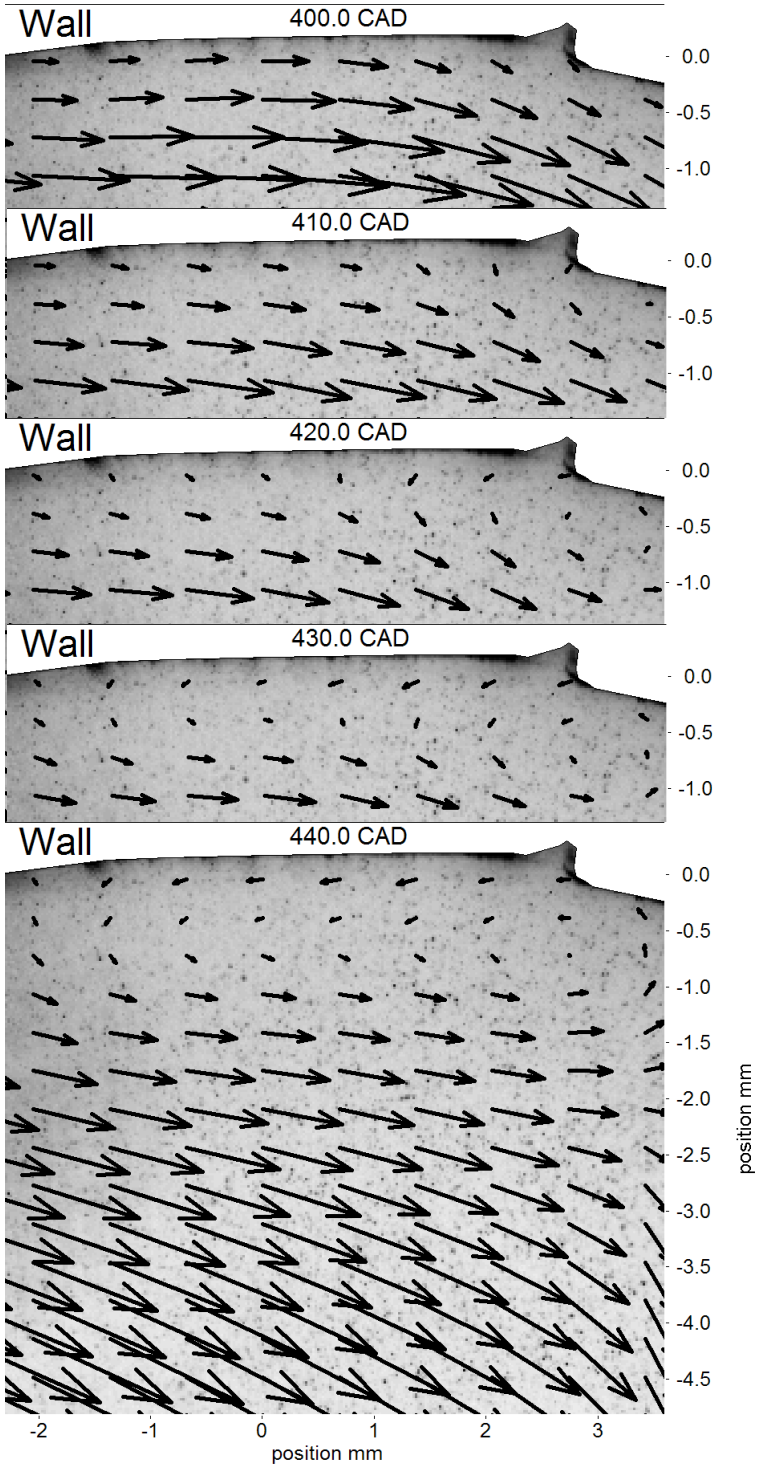

Figure 5-4: Initiation and progression of flow reversal during the expansion stroke. Spark plug and fuel injector are located to the right and left of each image, respectively. Measurements obtained from the low resolution experiment.

Velocity gradients in horizontal direction are noticed in Figure 5-4. Therefore, care must be taken when conducting high magnification imaging experiments near the cylinder wall to avoid shift in the field of view. A simple act such as tightening a bolt on the camera-lens fixture moves the field of view drastically (in a micro-imaging sense), which could result in different outcomes.

5.3.1 Mean Velocity and Fluctuation Intensity Profiles

An example averaged velocity field measured with high resolution is shown in Figure 5-5. This field of view was covered using the full resolution of the CMOS chip at 800 x 600 pixels. The origin of the y-axis is at cylinder head and the distance from the cylinder wall to the first measured vector is approximately 22 μm. The gray background in Figure 5-5 shows a typical raw image obtained at high resolution with a signal to background ratio of around 1.7.

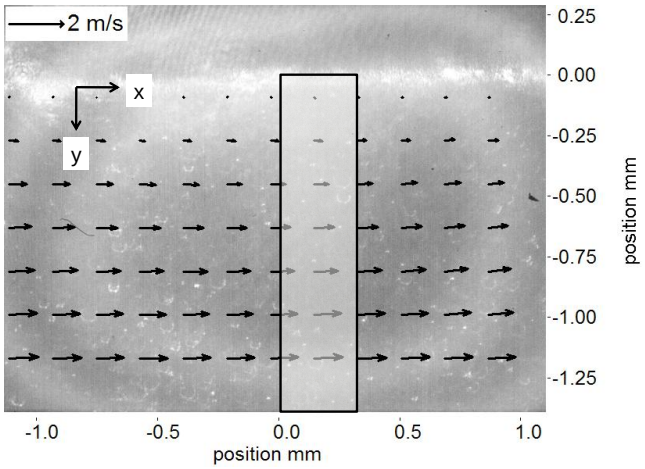

Figure 5-5: Ensemble-averaged velocity vector fields for crank angle 180. The highlighted area shows the region from where the horizontal (x-) velocity component of seven adjacent vertical profiles are spatially averaged and then are used for further analysis. Shown in the background is a raw image of seeded flow. *Note that for clarity in this image only every fourth vector in each direction is displayed to allow visualization of the vector tip.*

For this high-resolution experiment, data rates near the surface are low since the seeding density is lower than in the free stream. Therefore, to improve the statistical significance of the results, the horizontal (x-) velocity component of seven adjacent high-resolution ensemble-averaged vertical velocity profiles were averaged for this study. Their respective normalized standard deviation was used to show that spatially averaging over a small width of 315 μm that is spanned by the seven vertical high-resolution velocity profiles does not bias the results. This is shown in Table 5.6, where this normalized standard deviation remains well below 5% except for the points closest to the surface. Figure 5-6 shows all seven individual velocity profiles at 180 CAD to illustrate the negligible spatial velocity gradient in the horizontal direction.

Table 5.6: Standard deviation of seven adjacent horizontal velocity components as a function of distance from the wall for selected CAD.

	Standard Deviation/Average Velocity (%)			
y-location (mm)	180 CAD	270 CAD	360 CAD	450 CAD
0.045	23.8	19.3	14.4	30.0
.675	1.0	1.5	3.8	0.6
1.35	0.8	0.8	1.9	4.6

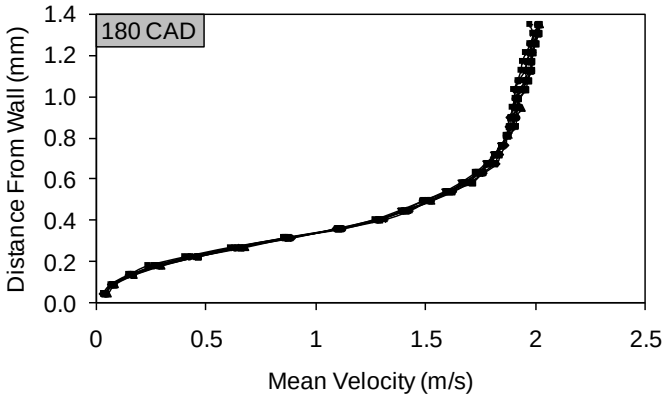

Figure 5-6: Seven velocity profiles were used to determine a spatially averaged (over 315 μm) velocity profile to improve the statistical significance of the velocity data closest to the surface. The example shown was taken at 180 CAD and shows the low variation across the averaged region, justifying this approach.

Ensemble-averaged velocity vector fields and the fluctuation intensities for the high-resolution data were calculated from data measured for 98 consecutive motored cycles from 180 to 490 CAD at every other crank angle. Figure 5-7 shows the evolution of the ensemble-averaged high resolution profiles of the horizontal velocity component during the engine cycle and, for more details, Figure 5-8 shows velocity profiles at selected crank angles for the duration of compression and most of the expansion stroke. Velocity is highest at the beginning of the compression stroke because both intake valves are still open. The primary (bulk flow port) intake valve and the secondary (tangential port) intake valve start closing at 110 and 112 CAD, respectively. Velocity decreases as the primary and secondary intake valves close until they are fully closed at 231 and 242 CAD, respectively. The maximum velocity from 240 to 290 CAD remains around 1 m/s. In this region, the momentum brought into the combustion chamber by the intake flow is dissipating; however, it is compensated for by the momentum gained from the upward piston movement. After 290 CAD, velocity starts increasing until 330 CAD.

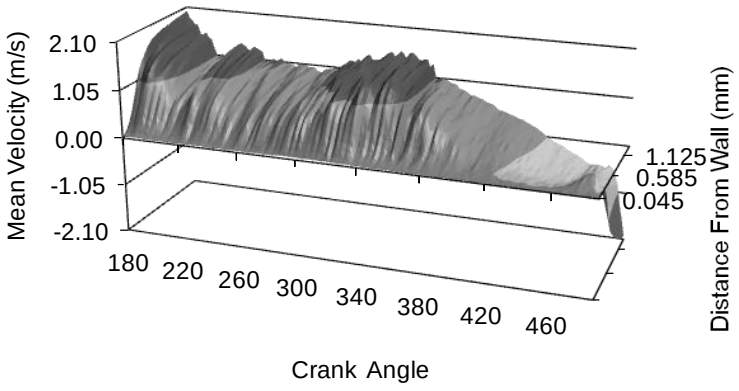

Figure 5-7: Ensemble-averaged velocity profile as a function of crank angle during the compression stroke and most of the expansion stroke (180 to 490 CAD).

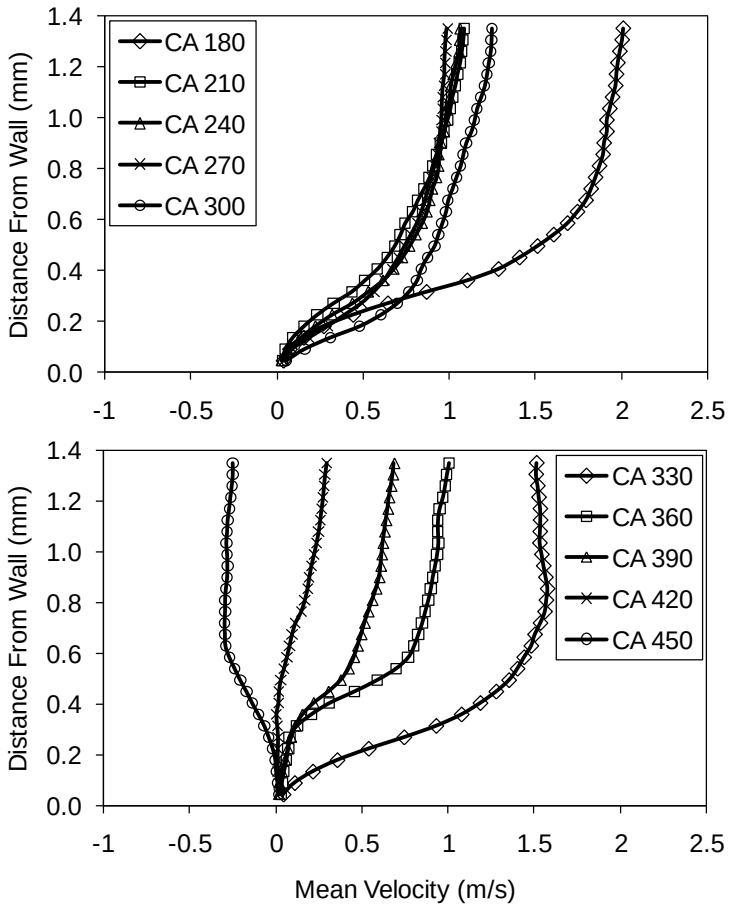

Figure 5-8: Ensemble-averaged velocity profiles at selected CAD during the end of the compression stroke and most of the expansion stroke.

Around 330 CAD, velocity starts to decrease as the piston slows down when it approaches TDC. The mean tumble flow breaks down to structures of the size of the clearance height, which results in a loss of flow momentum. Flow velocity continues to gradually decrease until around 400 CAD when a flow recirculation in the opposite direction of the mean in the vicinity of the spark plug initiates flow reversal near the wall region while the region away from the wall continues in the same direction with no reversal. This is more prominently visible in the low-resolution vector fields shown in Figure 5-4 that shows the progress of the flow reversal, initiated by a recirculating flow

next to the spark plug. This near wall reversal then extends to cover the wall area between the spark plug and the fuel injector, while the region away from the wall still maintain its original flow direction. At 489 CAD, the whole flow field reverses direction because of the blow down stream into the cylinder when the exhaust valves start lifting. This is because the exhaust backpressure is several kPa above the in-cylinder pressure at the exhaust valve opening. It should be noted that while the specified exhaust valve opening (EVO) is at 497 CAD at 0.1 mm lift, they actually start lifting at 489 CAD.

In-cylinder flows in general exhibit strong variability (3). High fluctuation intensities were also measured in the engine used in this study (57) and (61). The profiles showing the horizontal fluctuation intensity component confirms that this is also the case in the near-wall flow region (Figure 5-9). Fluctuation intensities are on the order of the mean velocities throughout the engine cycle.

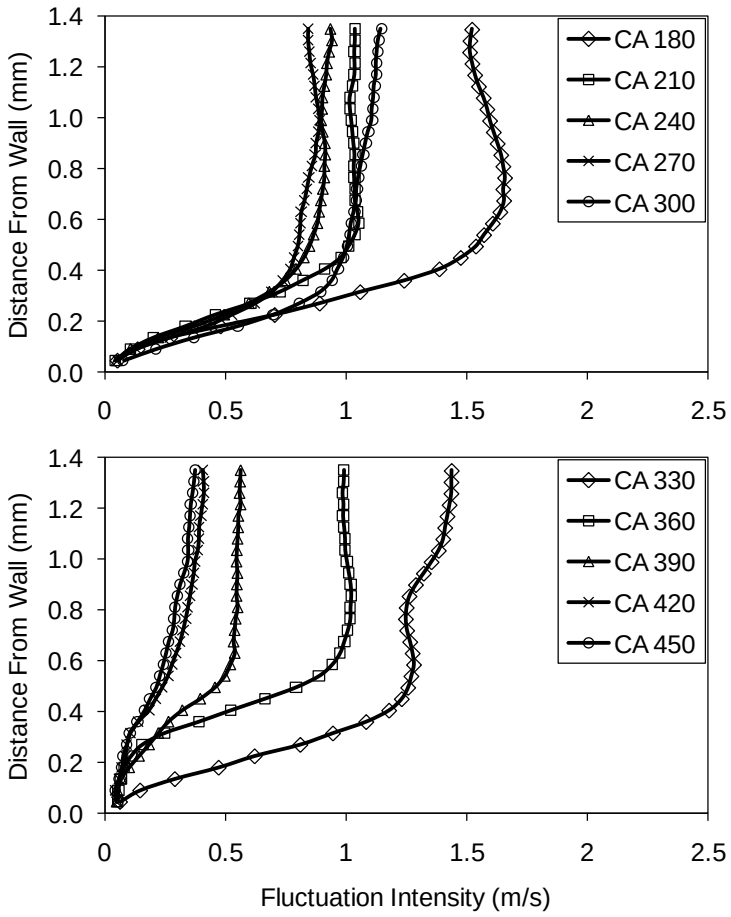

Figure 5-9: Fluctuation intensity profile as a function of crank angle (180 to 450 CAD).

5.3.2 Vortex Visualization and Identification

The capability to conduct an extensive vortex structure investigation in combustion chambers should complement the study of velocity boundary layers to better understand the engine heat transfer problem. The application of PIV to study boundary layers in internal combustion engines has the added benefit of visualizing and identifying near wall vortex structures from the instantaneous flow fields. This addition broadens the study of engine heat transfer from investigating mean velocity profiles and their impact on the energy equation to exploring the effect of vortical structures embedded in the

instantaneous flow fields in transporting momentum and energy from and away from the wall.

Low and high resolution instantaneous velocity vector fields were analyzed applying different decomposition methods. Figure 5-10 shows a low resolution instantaneous velocity vector field (sub-figure: a) decomposed using different methods. Sub-figures b to e show different results applying Galilean decomposition (deviation velocity field, u_c: see Equation (3.31)). The maximum velocity of the ensemble averaged velocity field, $U_{\text{max,mean}}$ was used as a basis to vary the convection velocity, U_c. For sub-figures b, c, and d, the convection velocity is 0.7 $U_{\text{max,mean}}$, 0.5 $U_{\text{max,mean}}$, and 0.3 $U_{\text{max,mean}}$, respectively. For sub-figure e, the convection velocity used was the spatial average of the instantaneous velocity vector field (spatial average of sub-figure a). As discussed in Chapter 3.4.1, most vortical structures could be revealed if a wide range of convection velocities is tested. The Galilean decomposition is sometimes preferred because it retains the mean flow motion. Reynolds decomposition is primarily applied to analyze turbulence statistics (i.e. turbulence intensity, Reynolds stresses, and kinetic energy budget). The fluctuation velocity vector field, u´, is shown in sub-figure f. Reynolds decomposition reveals more vortices than any single Galilean decomposition because vortical structures often move at velocities similar to the local mean velocity. On the other hand, it removes large-scale features associated with the mean flow. Sub-figure g represents the small-scale structures revealed by a high-pass LES filter. It is noted that this filter is capable of extracting more structures than either the Galilean or the Reynolds decomposition methods. This is expected since the high-pass filter in general is the

instantaneous flow field minus the low-pass filter where velocities are averaged over a local domain where its size represents filtering cut-off scale . So instead of subtracting a constant convection velocity as in the Galilean decomposition, or an ensemble average as in the Reynolds decomposition, the LES high-pass filter subtracts a local convection velocity averaged over a predetermined domain, thus removing slowly changing background in space. In sub-figure f, the averaging domain was chosen to be of the size of 1 mm (3 grid spacing). This domain size was chosen based on the swirling strength map that will be discussed next where the average noticeable vortex structure was on the order of 1-2 mm. The LES domain size could be reduced or increased to visualize structures of smaller or larger sizes, respectively. Sub-figure g shows the low-pass LES filter which was subtracted from the instantaneous velocity vector field to obtain the high-pass filter.

Vortex identification based on critical-point analysis of the local velocity gradient tensor (see Chapter 3.4.2) was applied to the instantaneous velocity vector fields. The maps of swirling strength help identify the location, size, and strength of vortical structures. Those maps also help in verifying or modifying flow visualization methods. For example, by comparing the swirling strength map to the Galilean decomposed flow field, one can change the convection velocity values to an equivalent of the local velocity averages within the area occupied by each individual identified vortex. While this seems to be a tedious procedure, it would definitely help visualize all possible structure sizes while retaining the mean flow behavior. In the case of LES filtering, the size of the

domain where the filter is applied could be varied to resolve smaller or larger scales depending on what the swirling strength map is revealing.

The swirling strength maps obtained from the instantaneous flow field of Figure 5-10 (sub-figure a) is superimposed to each decomposed flow field shown in same figure, except the low-pass LES (sub-figure h). Results are shown in Figure 5-11. It could be seen that the Galilean decomposed fields need several convection velocities to reveal all possible vortical structures. While the Reynolds decomposed field reveals more structures than any of the Galilean decomposed fields, there are still some identified structures that are not visible in the decomposed vector field. For this flow field, LES decomposition seems to show all possible vortices except for a number of small ones which require domain size smaller than the 3 grid spacing used (minimum possible is 2 grid spacing). The effect of changing the domain of the LES filter will be discussed next when examining the high resolution results.

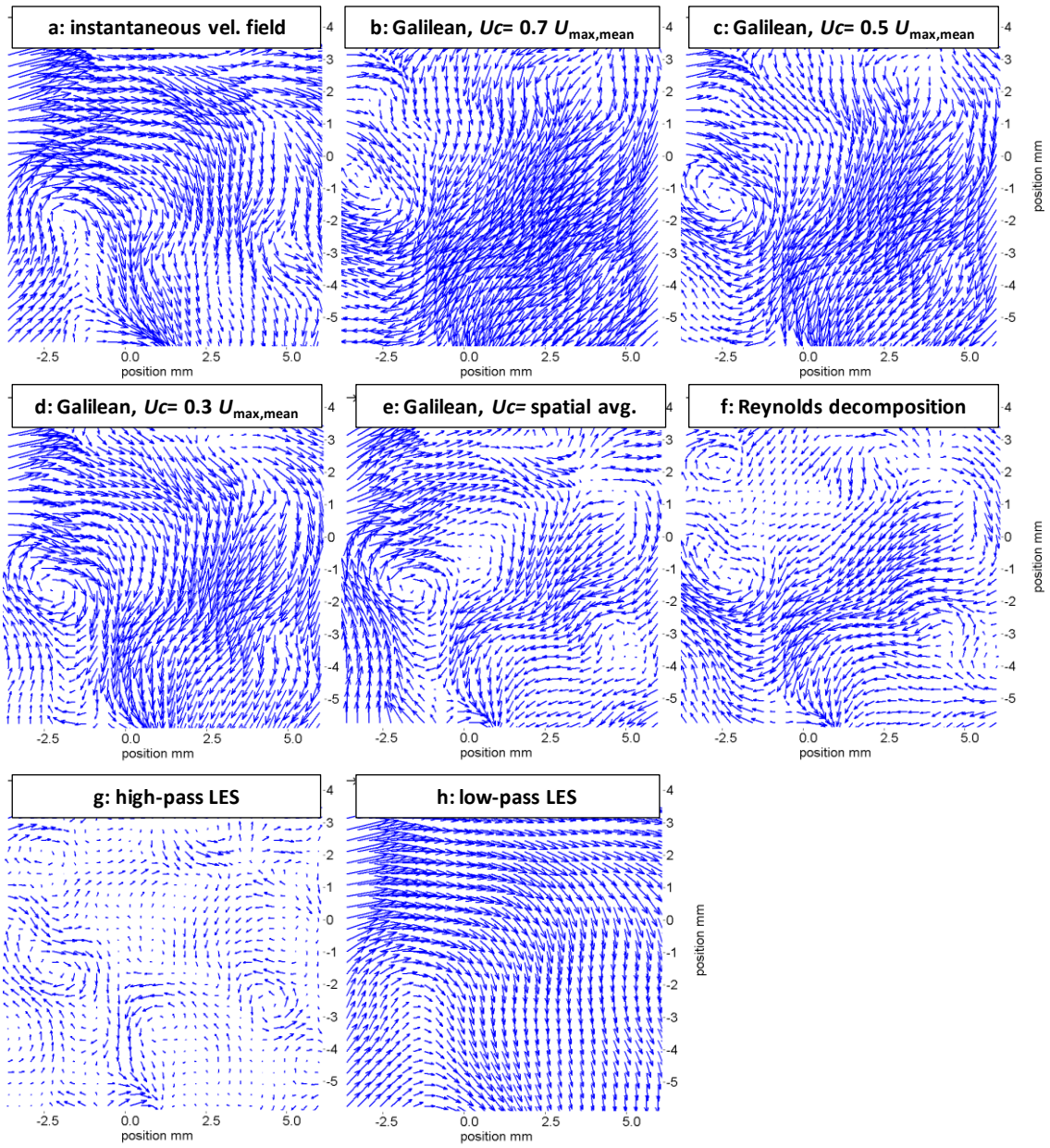

Figure 5-10: a) Low resolution instantaneous flow field decomposed using a number of Galilean convection velocities: b) Uc = 0.7 the maximum velocity of the ensemble averaged flow field ($U_{max,mean}$), c) Uc= 0.5 $U_{max,mean,}$ d) Uc = 0.3 $U_{max.mean}$, e) Uc = instantaneous velocity field spatial average, f) Reynolds decomposition, g) high pass LES, h) low pass LES.

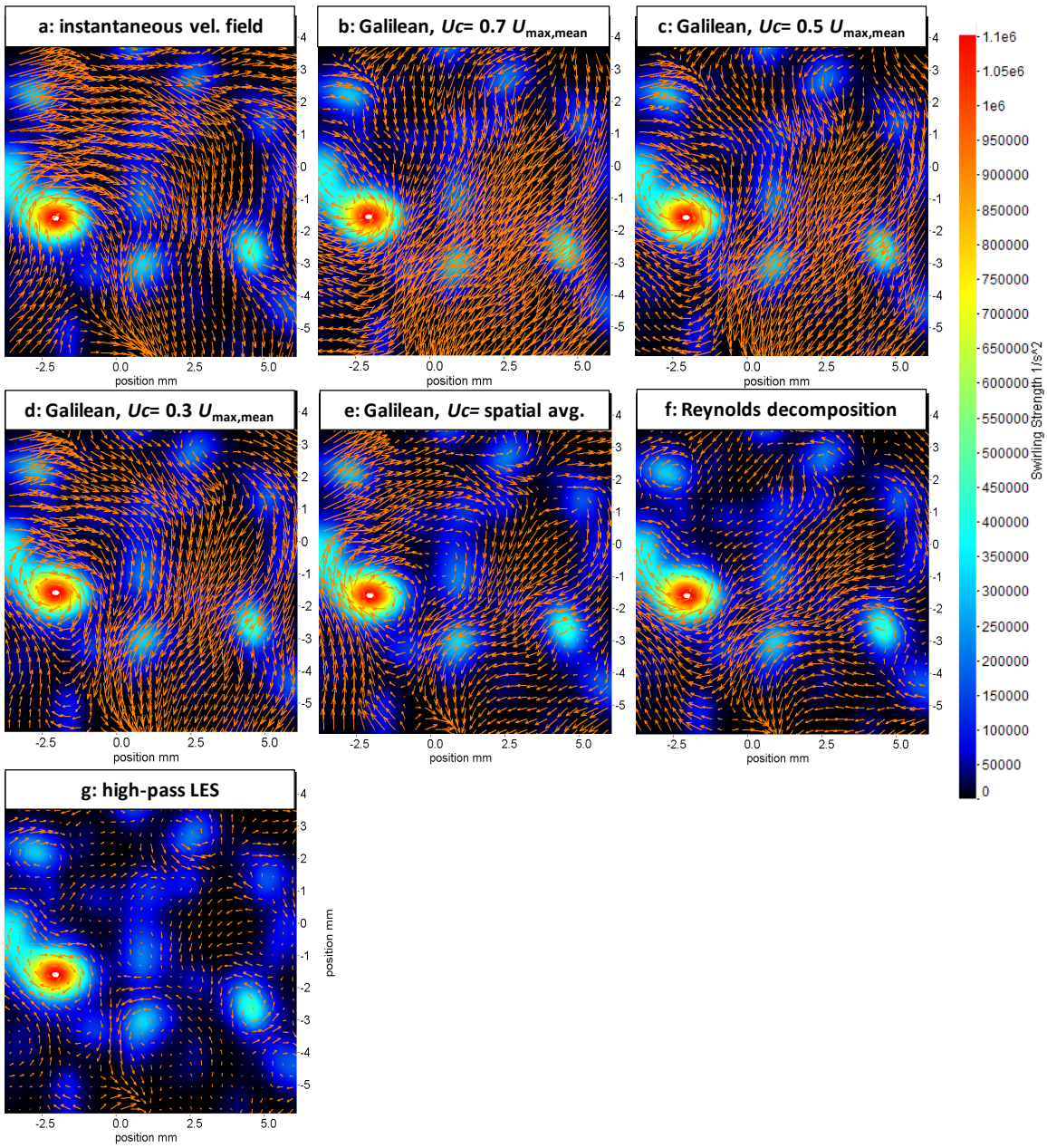

Figure 5-11: Swirling strength map superimposed on the different decompositions of the instantaneous flow field described in Figure 5-10.

Figure 5-12 shows the swirling strength map of a high resolution instantaneous velocity vector field superimposed on a LES high-pass filtered field using a 225 μm (5 grid spacing) velocity domain. It could be seen that structures of the size of a quarter mm

are revealed with this LES size domain, there are still some smaller size structures shown on the swirling strength map that are not extracted with this LES domain size. Figure 5-13 shows a swirling strength map superimposed on a LES filtered field applying a 225 μm domain (top) and a 90 μm domain (2 grid spacing). By comparing the LES decomposed fields to the swirling strength map, the high-pass LES filter applying the 90 μm domain reveals more smaller-scale structures.

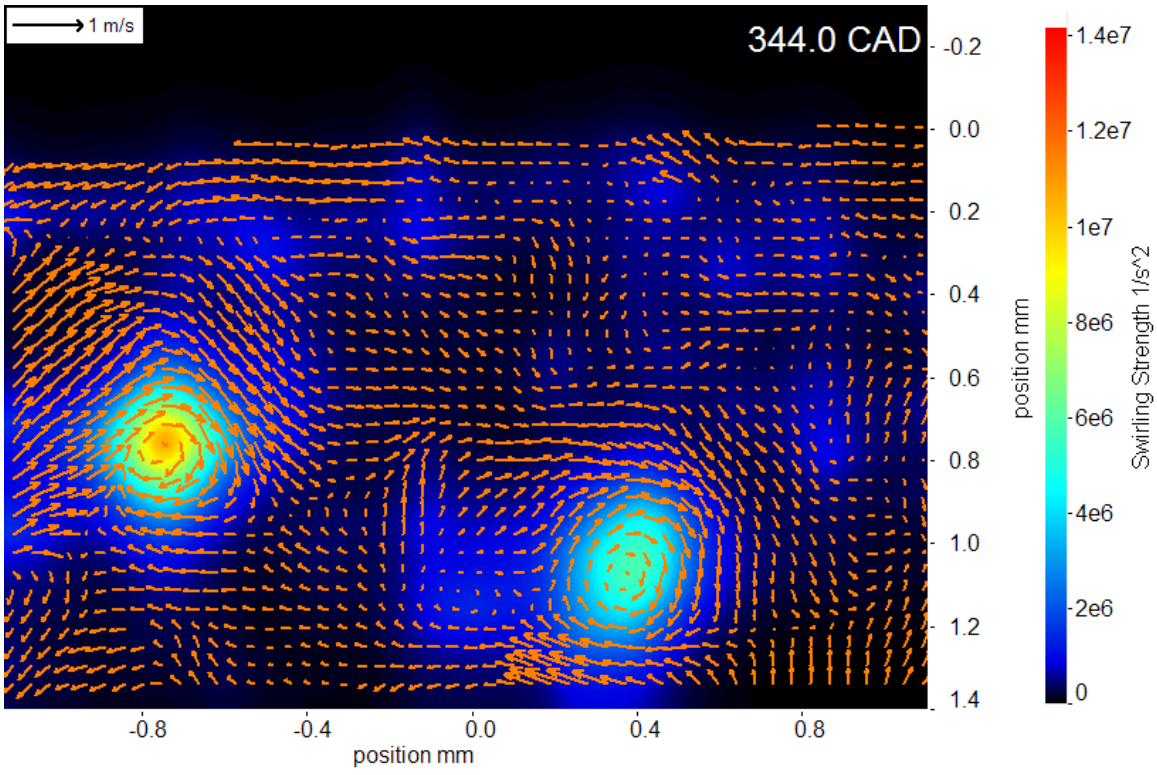

Figure 5-12: High resolution instantaneous velocity vector field decomposed using high pass LES filter applied over a 0.225 mm domain (5 grid spacing).

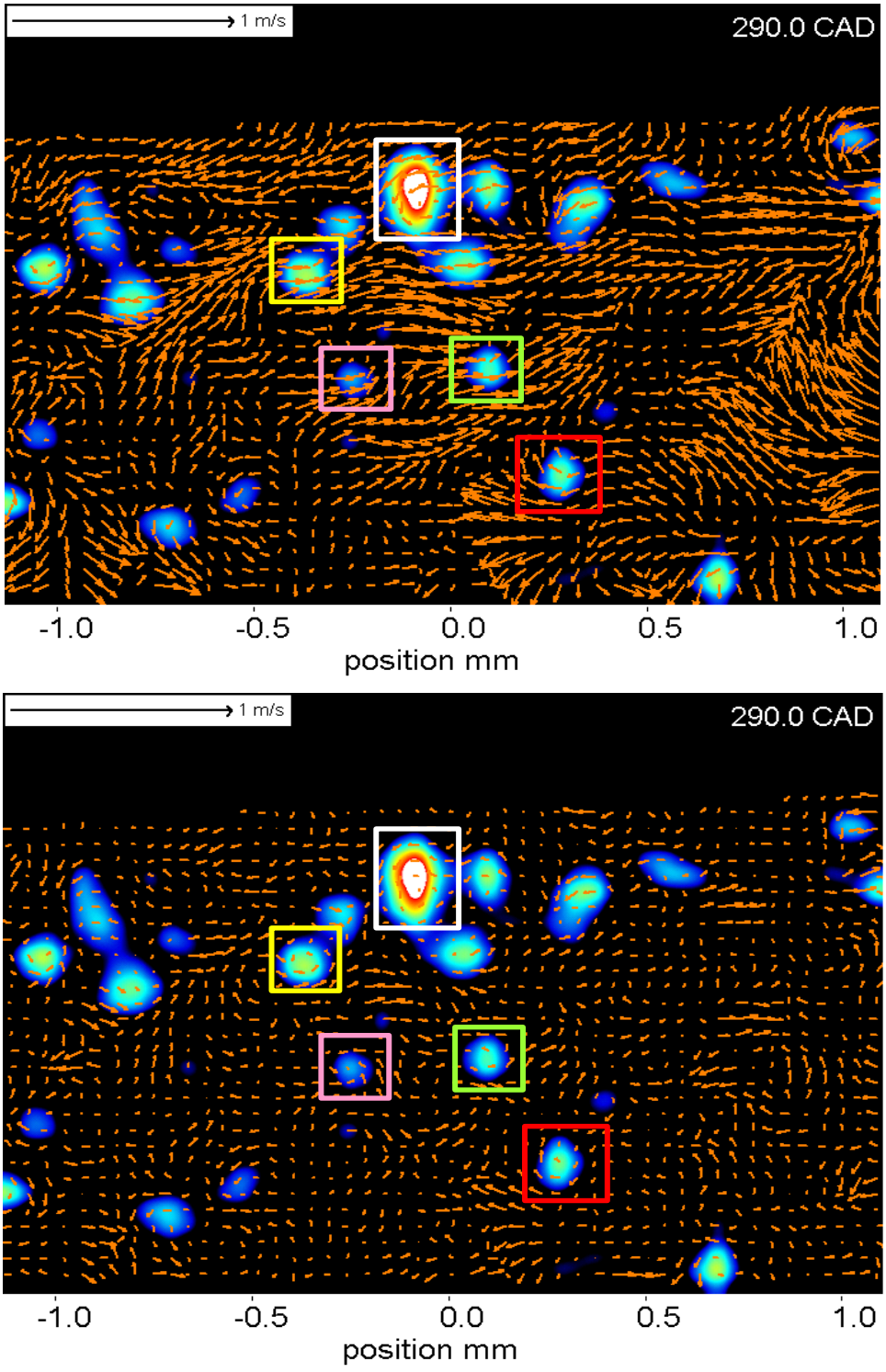

Figure 5-13: High resolution instantaneous velocity vector field decomposed using high pass LES filter applied over a 225 μm domain (5 grid spacing) (top image) and a 90 μm domain (2 grid spacing) (bottom image).

In general, the swirling strength maps could be used to obtain statistics on the location, size, and strength of vortical structures. Based on those maps, the LES domain could be varied to reveal the most possible vector representations of the vortical structures which should help identify their rotation direction.

5.3.3 Continuity Equation

Pressure fluctuations among cycles are usually expected especially in fired runs which are not the case in the current motored run experiment. Favre averaging is considered to account for pressure variability which adds to computation time and complexity. To investigate whether pressure fluctuations exist in the motored runs, Favre average of the normal x-component Reynolds stress was calculated at every CAD and results were compared to the ensemble average Reynolds stress where density was not accounted for. Difference between the two is shown in Figure 5-14. The difference on average is around 0.31% which indicates that Favre and ensembles averages are identical; therefore density can be assumed constant per realization (CAD) which simplifies calculations of averaged quantities. This outcome also simplifies Equation (2.40) by eliminating the third term reducing it to

$$\frac{\partial \overline{\rho}}{\partial t} + \frac{\partial}{\partial x_i}\left(\overline{\rho}\,\overline{u}_i + \overline{\rho' u'}\right) = 0$$

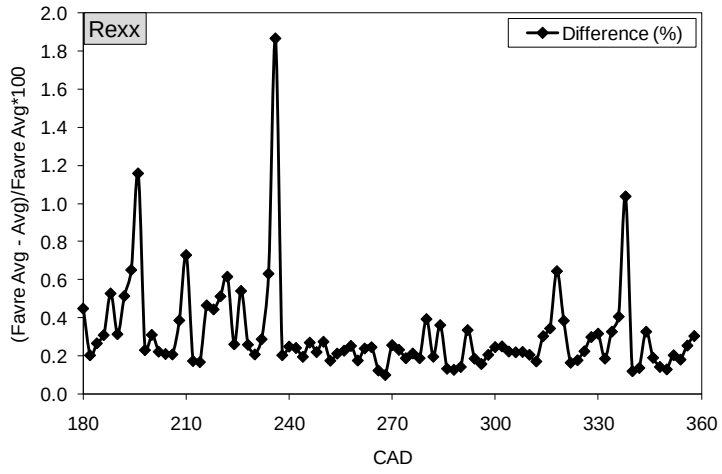

Figure 5-14: Difference between Favre averages and ensemble averages.

Continuity equation is expanded and re-arranged to check for the in-plane motion (z-component). For lack of information, spatial gradients of density are not accounted for; however, their importance on balancing the continuity equation shall be pointed out in the following discussion.

$$\frac{\partial \bar{w}}{\partial z} = -\left[\frac{1}{\bar{\rho}} \frac{\partial \bar{\rho}}{\partial t} + \frac{\partial \bar{u}}{\partial x} + \frac{\partial \bar{v}}{\partial y} + \frac{1}{\bar{\rho}} \left(\bar{u} \frac{\partial \bar{\rho}}{\partial x} + \bar{v} \frac{\partial \bar{\rho}}{\partial y} + \bar{w} \frac{\partial \bar{\rho}}{\partial z} \right) \right]$$

The density temporal gradient (first term on the right hand side) is calculated using central differencing in time. Velocity gradients (second and third term on the right hand side) are determined by central differencing in space. A plot of the density term and the combined velocity gradients, which is the divergence, versus the crank angle degrees is shown in Figure 5-15.

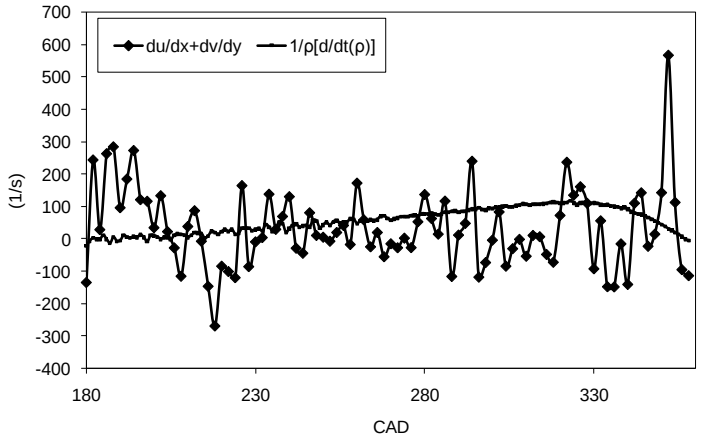

Figure 5-15: Divergence and temporal density gradient versus CAD.

If the flow is two dimensional, the two terms shown in Figure 5-15 must sum up to zero. It is obvious from the discrepancy between the two that there is a noticeable out of plane motion at the measurement plane throughout the compression stroke. Engine flows in general are three dimensional and the extent of the magnitude of the out of plane velocity component depends on a number of factors such as combustion chamber design, and swirl and tumble levels. In the current engine under investigation, the field of view is in the tumble plane and there is a swirl flow of a ratio of 0.8 induced by the intake manifold configuration, which would definitely have an impact on promoting a third velocity component in the tumble plane flow.

The spark plug which is located few millimeters downstream also has an impact on promoting a third velocity component in the out of plane direction as illustrated in Figure 5-16.

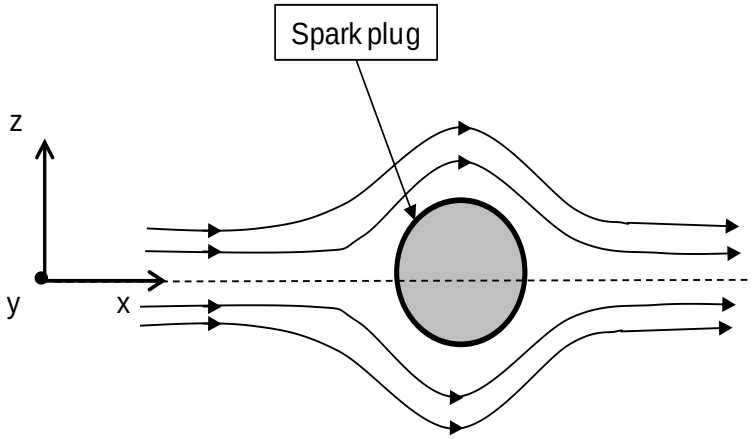

Figure 5-16: Spark plug impact on enhancing the third velocity (z-) component.

Another important factor that might had an effect on the balancing of the continuity equation was ignoring the density spatial gradients, which if neglected in the x and z directions only could be acceptable but not in the y direction (normal to the cylinder head). Maximum gas core temperature in the combustion chamber in a motored run at 800 RPM was estimated to reach 730 K which is more than twice the cylinder head temperature approximated at the coolant temperature of 318 K. This indicates that there must be a significant density gradient in the normal to the wall direction (y-axis). This density gradient should have an opposite sign of the *u* velocity gradient since the density is expected to increase as the cold wall is approached; hence, impact balance of the continuity equation.

Divergence of the ensemble averaged velocity vector fields was determined to detect any possible temperature gradient which would vary the density within the velocity profile. The divergence images shown in Figure 5-17 do not indicate any gradients in either direction. Therefore, most of the imbalance of the continuity equation could be

caused by a third velocity component (in-plane z-component) due to the swirl motion and the presence of the spark plug which is located few millimeters downstream.

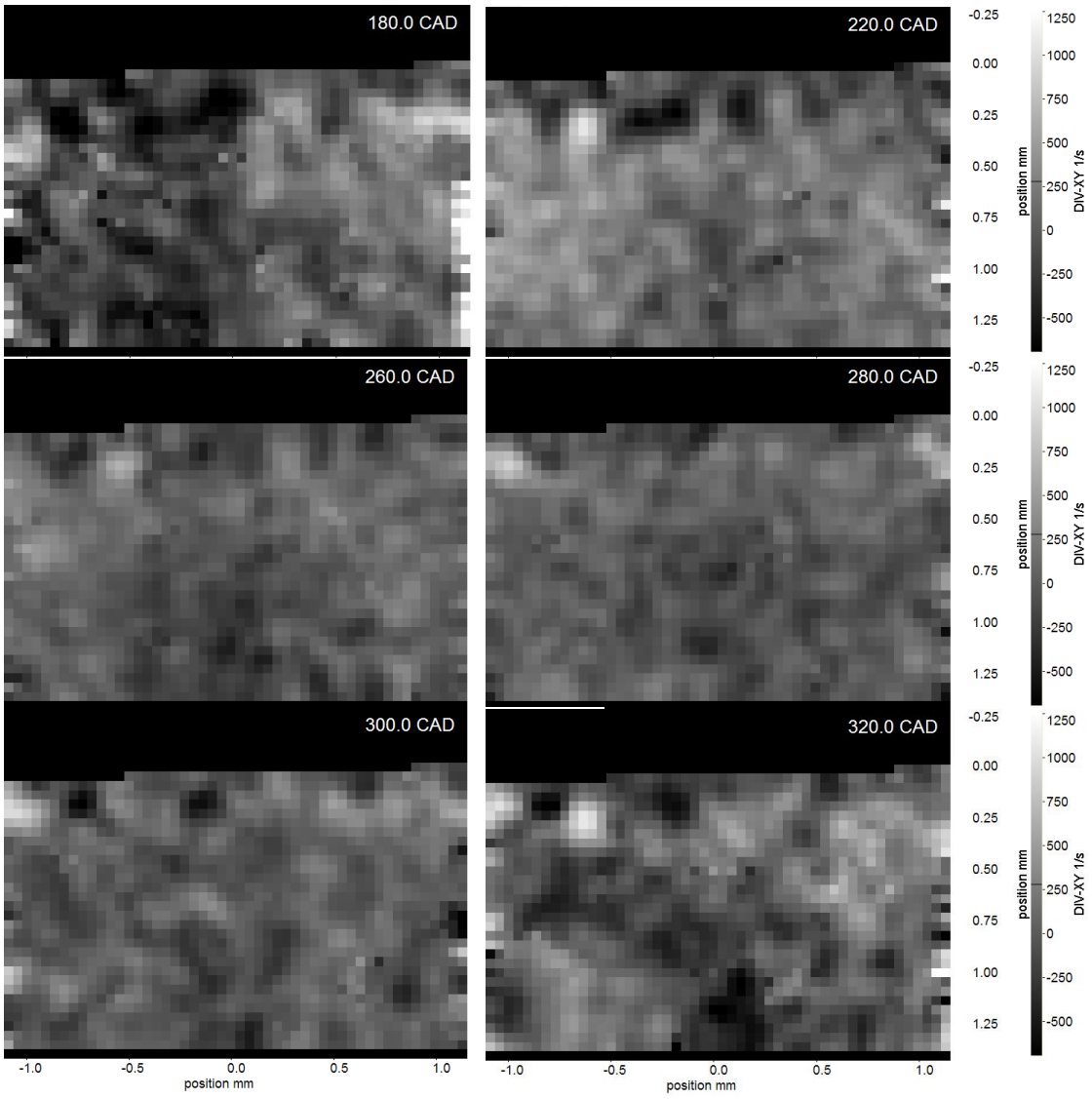

Figure 5-17: Divergence of the ensemble averaged velocity fields at selected CAD.

5.3.4 The Law of the Wall

The law of the wall was constructed based on the inner velocity and length scales (Equations (2.57) and (2.58)). Fluid properties (viscosity and density) were evaluated at the wall temperature approximated to the coolant temperature of 95° C. Finding the inner

velocity length scale actually depends on the knowledge of the wall shear stress which in turn is based on the mean velocity gradient (*du/dy*) at the wall (y = 0). The mean velocity gradient was approximated by dividing the mean velocity closest to the wall by its corresponding distance from the wall, which could be within 45 μm. It was hard to determine the exact location of the wall after preprocessing the raw PIV images (background subtraction, subtracting sliding minimum, and subtracting pixel-specific ensemble minimum). The viscous sublayer ($u^+ = y^+$) was used as a criterion to determine the exact distance of the closest measured velocity to the wall. Different values for the distance from the wall (y in Equation (3.23)) were tested (22.5 μm, 33.75 μm , and 45 μm). The value of 22.5 μm gave the best results among the three suggested values in terms of the closest fit between the viscous sublayer of the constructed law of the wall and the experimental velocity profiles. The mean velocity profiles and the distance from the wall were normalized by the inner velocity and length scales giving u^+ and wall units y^+. In addition, viscous sublayer and log-law velocity profiles were calculated using Equations (2.62) and (2.63), respectively. Normalized experimental velocity profiles compared to viscous sublayer and log-law for selected crank angle degrees are shown in Figure 5-18.

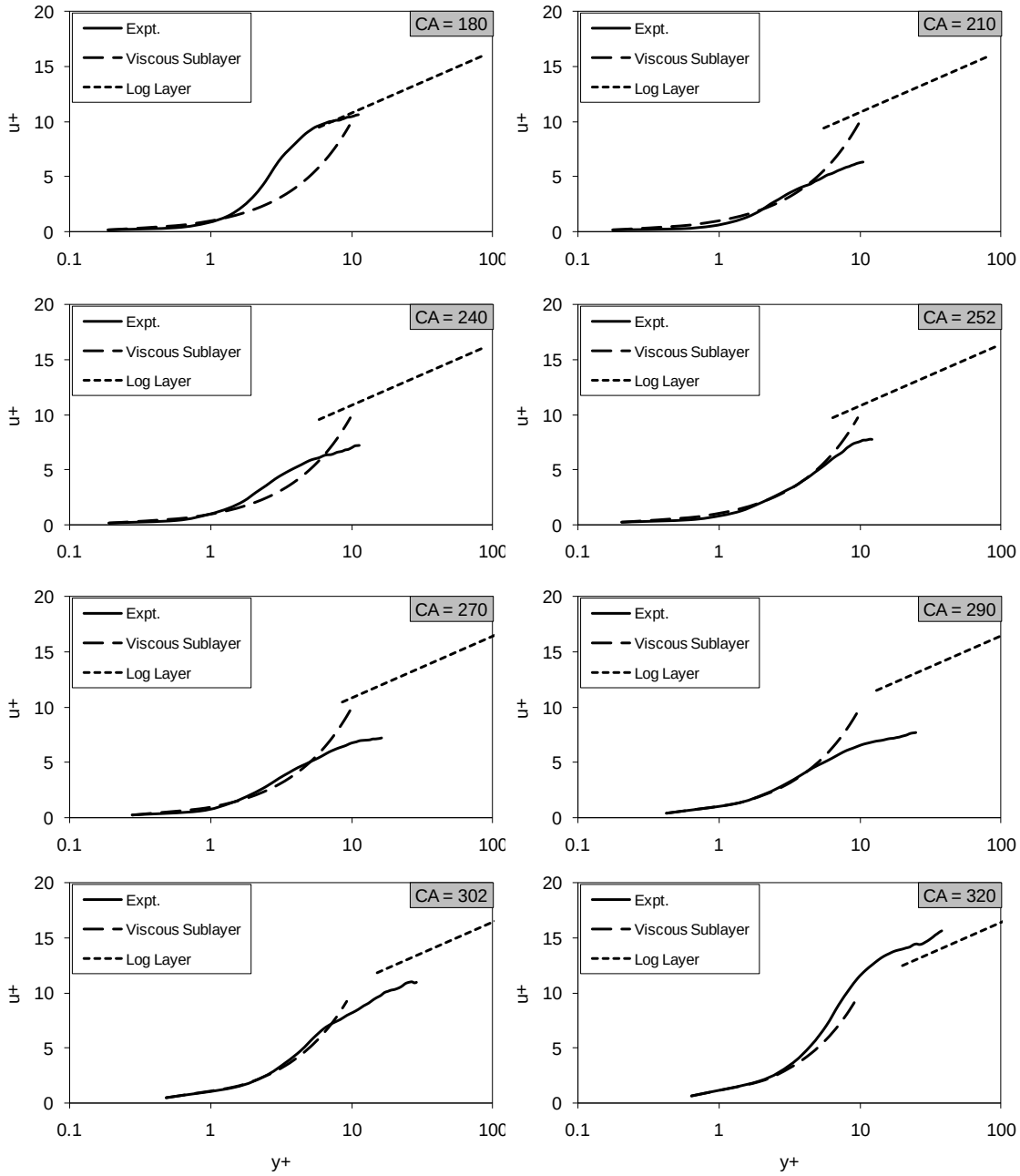

Figure 5-18: Experimental results of velocity profiles compared to viscous sublayer and log layer at selected CAD.

It can be seen from Figure 5-18 that there is a good agreement between experiment and the law of the wall in the viscous sublayer region. However, around y^+ = 5, experiment does not seem to approach the log layer which actually starts at y^+ = 30, and even though their trends look similar, there is a negative offset in most cases between

the log layer and experiment. It is known that the law of the wall is universal for pipe, channel, and boundary layer (flat plate) flows with some minor differences in the outer region between internal and external flows. It is difficult, however, to categorize combustion chamber gas flow as any of these types of flows. Besides, the universal law of the wall was derived for two dimensional steady and fully developed flows. Engine flows on the other hand are three dimensional transient and developing which makes it very hard to compare them to the law of the wall. In addition, there is another major factor that must have a great impact on the noticeable offset from the log layer which is the definition of the free stream flow. Unlike pipe and flat plate flows where a maximum free stream velocity is reached at a certain distance from the wall (boundary layer thickness) and then held constant at higher distances from the wall, the tumble motion during intake and compression strokes is similar to the rigid body motion where velocity increases away from the wall until certain distance from the wall where it starts decreasing and eventually reversing direction. This type of flow pattern could be partially seen in Figure 5-19 where the low resolution velocity profile is plotted along with the high resolution velocity profile for 200 CAD. It should be emphasized that the two experiments were conducted at different times and no means of exactly spatially overlaying the two profiles were available. The main purpose of Figure 5-19 is to show the impact of the flow pattern similar to the rigid body motion on the departure of the velocity profile from the log layer.

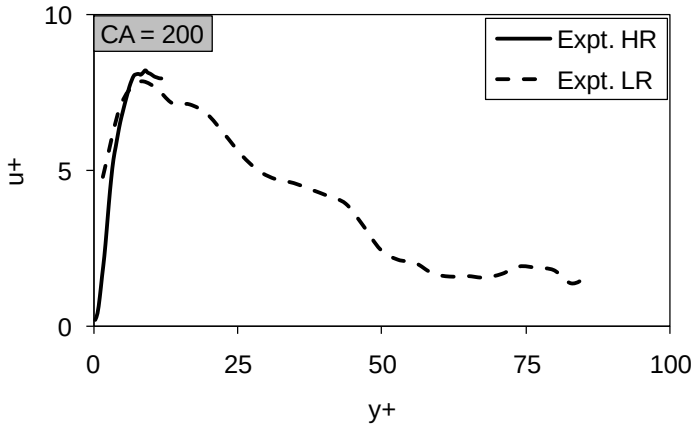

Figure 5-19: Low and high resolution velocity profiles at 200 CAD.

Reynolds stresses normalized by the friction velocity (inner velocity scale) at selected crank angle degrees are shown in Figure 5-20. The following notations for Reynolds stresses are used in the figure: $\mathrm{Re}\,xx = \overline{u'^2}$, $\mathrm{Re}\,yy = \overline{v'^2}$, $\mathrm{Re}\,xy = \overline{u'v'}$. At 180 CAD where both intake valves are open, the momentum flux by turbulence is in the highest range as could be seen from the magnitude of Rexx and Reyy. These two values decrease as both intake valves close which causes a drastic drop in the turbulent momentum flux. As the piston moves toward top dead center (360 CAD), tumble mean flow breaks down to smaller structures causing an increase in turbulence intensity and therefore a rise in turbulence momentum flux represented by an increase in Rexx and Reyy. In general, these two values increase steadily in the viscous sublayer after which the Rexx drops slowly while Reyy continue to rise. It is noticed from channel flow results in the literature (62) that these two values, along with Rezz and turbulent kinetic energy tend to reach their asymptote in the log layer region ($y^+ > 30$). While this region is not covered in the high resolution measurements, the general trend in most cases seems to be approaching a positive asymptote.

The peak values of the Reynolds normal stresses (Rexx and Reyy) normalized by the friction velocity for a channel flow which was determined from Direct Numerical Simulation (DNS) by Kim *et al*. (62) were found to be 7.5 and 1, respectively. The normalized Reynolds shear stress (Rexy) had a minimum value of -0.8. Spalart (63) obtained similar values for the Reynolds stresses normalized by friction velocity applying DNS to a boundary layer flow over a flat plate.

Values of Reynolds stresses obtained near the cylinder head are higher than the ones for a channel flow or a flat plate boundary layer flow. At the beginning of the compression stroke, the peak normalized Reynolds normal stresses (Rexx and Reyy) are 75 and 35, respectively, and the minimum value of the normalized Reynolds shear stress is -10. These values vary during the compression stroke as can been seen from Figure 5-20. They decrease in value until 230 CAD then increase gradually until 290 CAD after which their magnitudes are amplified due to the mean flow motion (tumble) breakdown to smaller structures as the piston moves closer to top dead center, thus enhancing turbulence intensity. The main factor that can be attributed to the higher magnitudes of Reynolds stresses compared to channel or flat plate flow is the cycle-to-cycle variability. When ensemble averaging, the cycle variability is not excluded. This results in an overestimation of the velocity fluctuations (See Chapter 3.2).

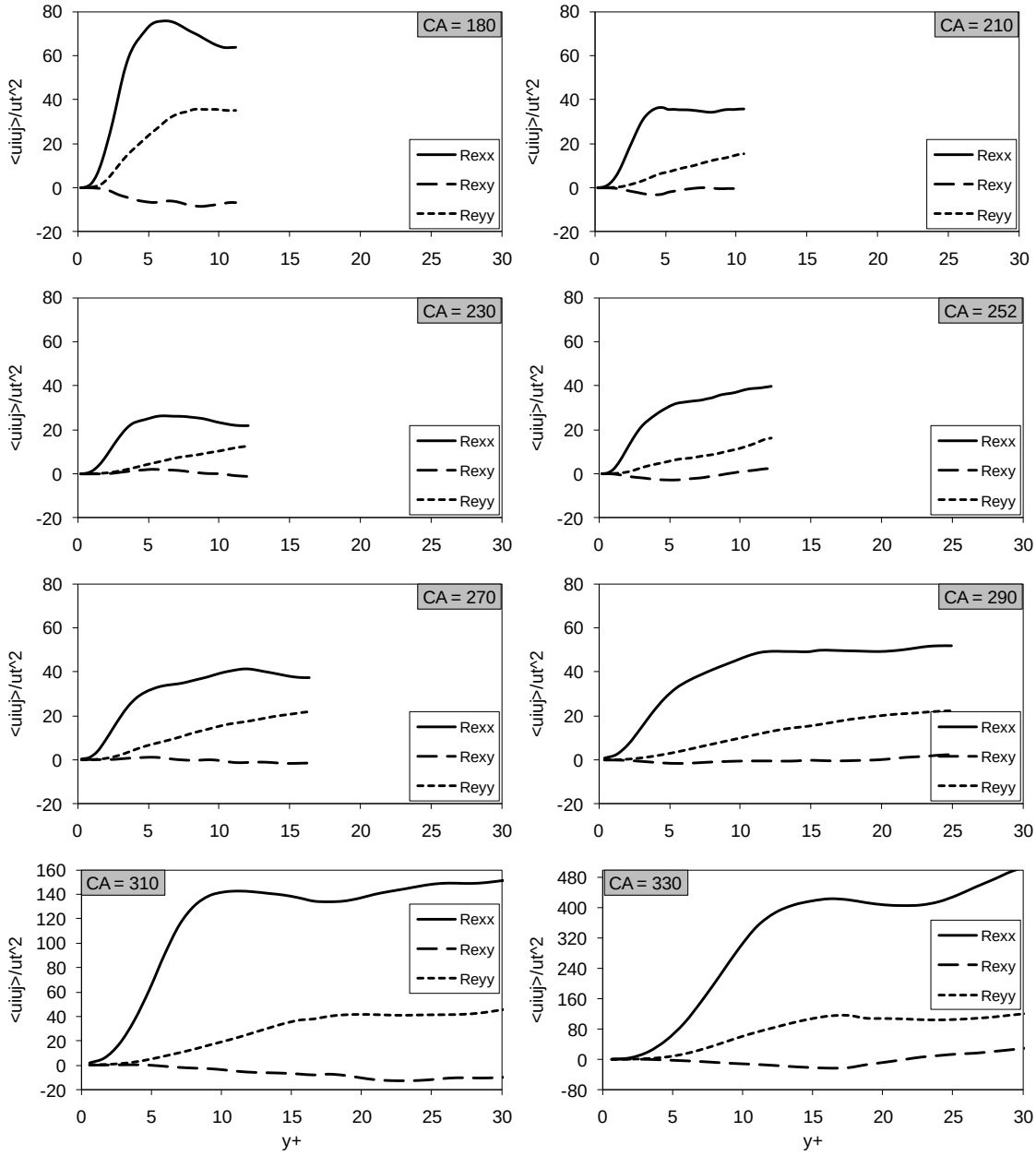

Figure 5-20: Normalized Reynolds stresses at selected CAD.

Turbulent kinetic energy production and dissipation (pseudo) at selected crank angle degrees are shown in Figure 5-21.

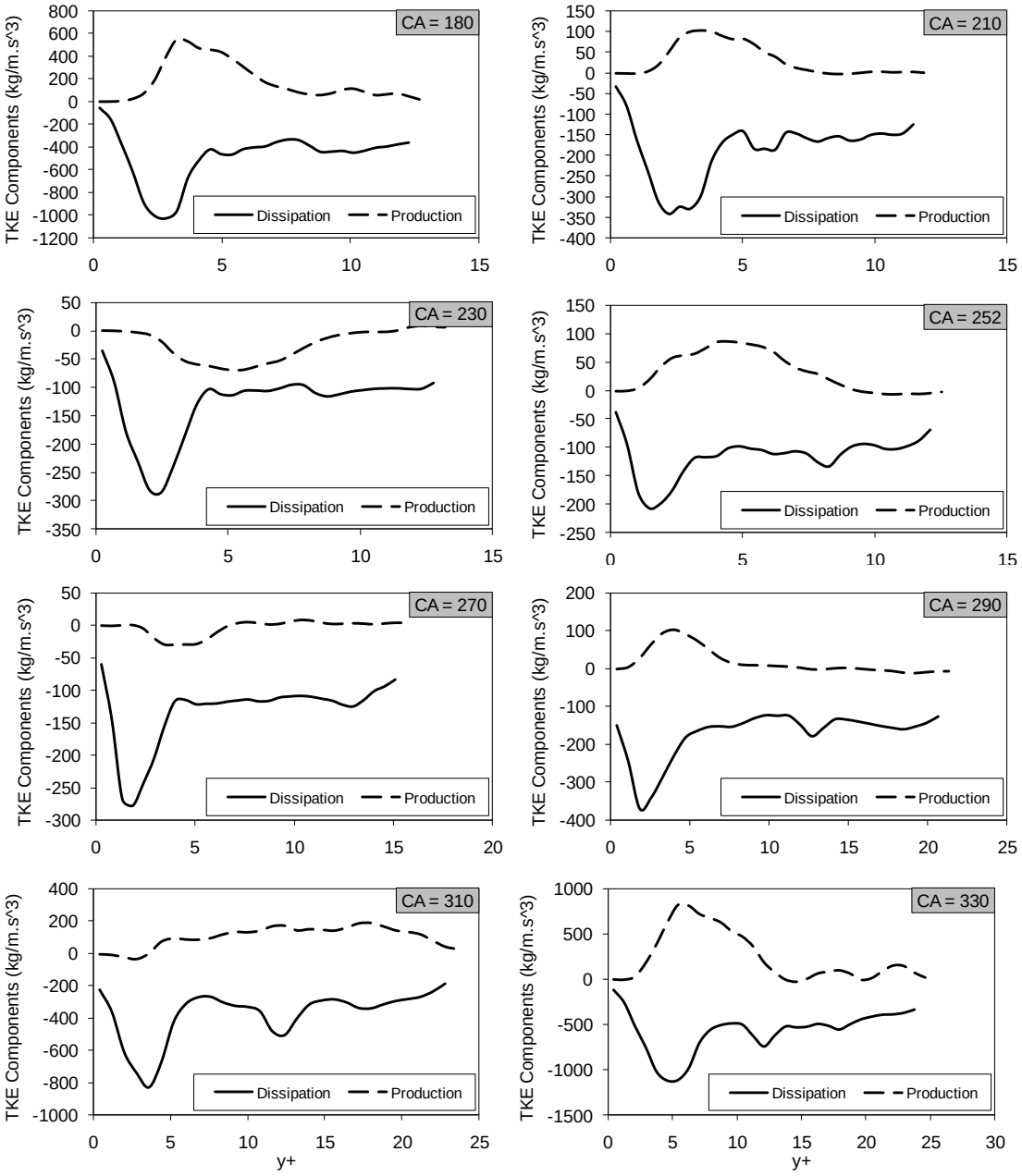

Figure 5-21: Production and dissipation of turbulent kinetic energy at selected CAD.

It can be seen from Figure 5-20 and Figure 5-21 that the turbulent activities reach their maximum within the viscous sublayer. Even though the log law region is not within measurements limits, the general trend show that turbulent kinetic energy production and dissipation achieve their peak values at y^+ less than 5. In an ordinary channel flow,

production peaks at $y^+ \sim 10$ and decrease slowly until it reaches zero at $y^+ \sim 400$, whereas from the current experiment results, it reaches zero at around $y^+ \sim 10$. The main factor that causes this significant discrepancy between the current engine results and the ordinary flat plate or channel flow is the difference in the free stream flow pattern. While the ordinary flat plate flow reaches a maximum at a certain boundary layer thickness beyond which it stays constant in the free stream; in this engine, mean flow motion in the form of tumble defines the flow pattern away from the wall which was described earlier as an increase in velocity from zero at the wall to a maximum velocity at a certain distance (positive gradient), then a decrease afterward until it reaches zero at the center of the tumble motion (negative gradient) after which it increases again in the opposite direction repeating the same pattern and creating an "S" shaped velocity profiles. Similar pattern is found in the "plane wall jet" flow in which the bottom half of the "S" shaped velocity profile exists and the rest the flow beyond that is quiescent. Schlichting (25) describes the region between the wall to the point of maximum velocity (similar to the velocity profile shown in Figure 5-19) as a two layer region consisting of a viscous wall layer and an "internal outer layer" which starts at zero Rexy and ends at the maximum velocity point. In this layer, the Reynolds shear stress changes sign and the turbulence production is negative. Energy is transferred from the turbulent fluctuations to the mean flow. This type of boundary layer behavior seems to exhibit a similar trend to the results at hand. It also presents a good reasoning why the engine results do not follow the law of the wall velocity distribution beyond the viscous sublayer. Figure 5-22 shows a more detailed description of the inner-outer layer. Turbulent kinetic energy, Reynolds shear stress, and mean velocity profile are plotted. The horizontal line in the middle of the plot

indicates the point at which Reynolds shear stress changes sign and production turns negative.

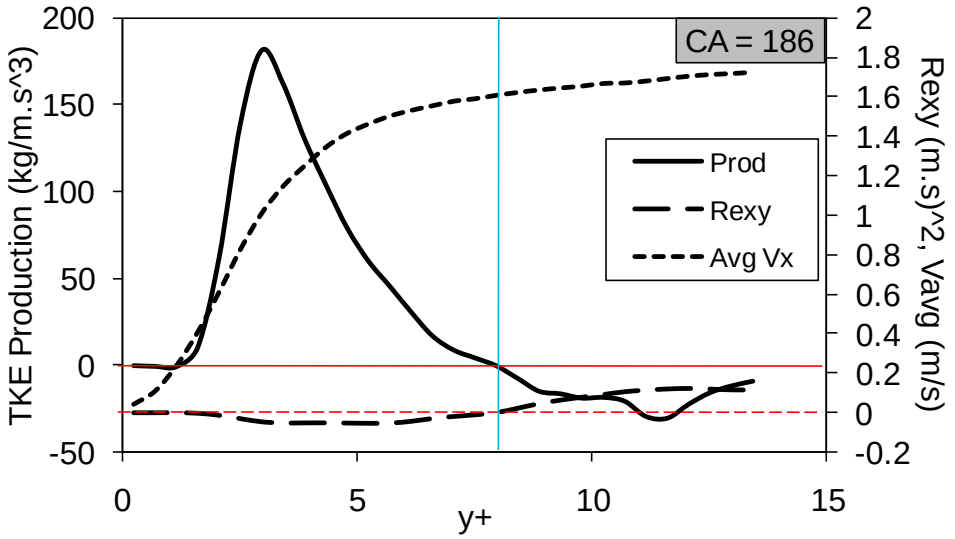

Figure 5-22: Turbulent kinetic energy production, Reynolds shear stress, and mean velocity profile at 186 CAD.

Even though fluctuations vanish at the wall ($y = 0$), the fluctuation strain rate and therefore dissipation do not as can be observed from Figure 5-21. Dissipation at the wall is balanced by viscous transport (26), a quantity that is not used in this discussion because the data were too noisy. It requires larger sample size (more cycles) to converge since it is a second order derivative.

CHAPTER 6

CONCLUSIONS AND FUTURE WORK

The measurements presented in this thesis show that boundary layer velocity and fluctuation intensity profiles could be resolved to within 22 μm from the cylinder head wall of a motored internal combustion engine utilizing a combination of a μPIV and PTV algorithm. The investigations were carried out in the pent-roof region of a production-type engine head. A CMOS camera coupled with a long distance microscope and a dual-cavity Nd-YLF laser were used for high-speed PIV measurements at 2.4 kHz frame rate.

Low-resolution PIV measurements were conducted to obtain flow fields that provide a larger scale overview of the in-cylinder flow to assist the interpretation of the high-resolution measurements. Flow deceleration started towards the end of the compression stroke. The flow continues its gradual deceleration during the expansion stroke until flow reversal starts around 400 CAD. It was noticed from the low resolution raw images and velocity vector fields that the flow reversal starts near the spark plug caused by a recirculation in the opposite direction of the mean flow near the cylinder head wall that temporally extends towards the fuel injector to reverse the flow near the cylinder head wall while the mean free flow preserves its original course until the instant

of exhaust valves open where the whole flow is totally reversed for few CAD due to the blow down effect.

High-resolution velocity fields were measured for 98 consecutive cycles at an engine speed of 800 RPM from 180 to 490 CAD at every other crank angle in each of these cycles. The ensemble velocity fluctuations are of the same order of magnitude as the mean velocities for the entire crank angle range that was studied.

The high-resolution high-speed μPIV+PTV measurements allowed identifying and tracking of sub-millimeter sized vortical structures as they moved within the boundary layer. In addition to the first time boundary layer results in internal combustion engines obtained by utilizing μPIV, the highly magnified two-dimensional instantaneous velocity vector fields provided an unprecedented substantial source of information regarding vortex motion within the boundary layer. While the mean flow results help understand the structure of the boundary layer velocity profile and therefore help provide modelers with actual representation of near wall mean velocity distribution, the identified vortices from the instantaneous velocity vector fields when sampled could offer in-depth understanding to the momentum and energy interaction with the engine wall.

Vortex investigation near the wall and within the boundary was carried out on the low and high resolution instantaneous flow fields. Different vortex visualization techniques were applied on the low resolution instantaneous velocity vector fields. Sub-millimeter vortical structures were revealed near the cylinder head. The size of extracted

vortex cores varied as the decomposition method is varied along with its parameters (i.e. convection velocity in the case of Galilean decomposition and the low-pass filter domain in the case of LES decomposition).

Swirling strength maps determined from critical-point analysis of the local velocity gradient tensor was an effective tool that revealed most of the possible vortical structures. It could be used in future studies to obtain vortex statistics that includes location, size, and strength of all possible structures. Vortex visualization techniques could be optimized in order to determine the direction of vortex rotation. The vortex visualization and identification methods were applied to the high resolution instantaneous velocity vector fields and structures as small as 90 μm were identified. Their rotational direction was visualized when the high-pass filter was applied to the smallest possible domain of two grid spacing (90 μm).

The comparison of the high resolution results with the law of the wall, along with the investigation of turbulence kinetic energy and Reynolds stresses, led to a preliminary conclusion that the nature of the free stream flow in internal combustion engines cannot be approximated to that of a flat plate or channel free stream. It is believed that the engine free stream flow, out of plane motion, density gradient in space, and temporal changes in the flow and the fluid properties are the reasons why the law of the wall cannot be implemented in internal combustion engines. The boundary layer and the corresponding turbulence production seem to resemble a plane wall jet pattern.

Being able to resolve boundary layers in internal combustion engines is one important step in analyzing the convective heat transfer in the combustion chamber. Numerical simulations and the models used to close the turbulent momentum and energy equations in engines require experimental data to support and validate the applicability of those models in internal combustion engines. Temperature measurements near engine walls are necessary to complement the current velocity measurements in order to provide modelers with a complete set of validation or modification tools.

To enable the development of engine flow and heat transfer models, velocity and fluctuations intensity profiles should be measured for the whole cycle to obtain a complete sequence of the progression of the boundary layer. Velocity profiles should also be measured as a function of engine speed. In conjunction with high-resolution measurements, velocity across the cylinder should be measured to understand what drives the evolution of the flow near the wall. Future work should also measure boundary layer velocity profiles in other locations, such as the cylinder wall. Velocity measurements near the cylinder wall were attempted by imaging at an angle which was not successful due to the fact that the camera was actually projecting a three dimensional velocity motion into a two dimensional frame. It was concluded that in order to image near cylinder wall flow motions at an angle, a three dimensional stereo PIV must be implemented which is an important upgrade to the current project. A two plane 3D PIV could be the next step afterward, which would lead to a comprehensive turbulence analysis (i.e. Reynolds stress and turbulent kinetic energy) and a better assessment for the continuity equation. Either a simultaneous low and high resolution setups or a larger format camera is recommended

in order to capture more details about the outer layer since the free stream flow has proven to have a great impact on the departure of the experimental results from the ordinary flat plate "law of the wall". Also, simultaneous temperature measurements should complement boundary layer investigations in order to implement more reasonable values of fluid properties and to ultimately provide modelers with a complete data package of velocity, temperature, and turbulence intensity profiles along with other turbulence statistics. Once this is accomplished, the convective heat transfer problem in internal combustion engines can be studied comprehensively and more realistically based on its essential fundamentals rather than by either imposing assumptions applicable to other configurations and flow conditions (i.e. flat plate 2D flow), or deriving empirical correlations based on a single (or multiple) point temperature/heat flux measurements.

Instead of imaging a complete engine stroke at a time, it is advisable to break it down to smaller intervals in order to increase the sample size to obtain better statistics, especially when analyzing higher order derivatives. This requires a very sturdy and stable setup to insure imaging the exact same location for each set. Tracking and sampling the coherent vortex structures in the engine boundary layers should complement the current velocity boundary layer study to give a comprehensive foundation for investigating heat transfer physics in IC engines, in addition to better understand turbulence production at the engine walls.

BIBLIOGRAPHY

1. Borman, G. and Nishiwaki, K., "Internal Combustion Engine Heat Transfer," *Prog. Energy Combustion Science*, Vol. 13, pp. 1-46, 1987.

2. Heywood, J. B., *Internal Combustion Engine Fundamentals*, New York: McGraw-Hill, 1988.

3. Lumley, J. L., *Engines: An Introduction*, Cambridge: Cambridge University Press, 1999.

4. Dimplefield, P. A., "Study of Autoignition in a Premixed Charge, Internal Combustion Engine using Comprehensive Chemical Kinetics; Experiments and Predictions," *PhD Thesis*, Department of Mechanical Engineering/Foster, University of Wisconsin, Madison, 1985.

5. Kays, W., Crawford, M., and Weigand, B., *Convective Heat and Mass Transfer*, 4th ed., New York: McGraw-Hill, 2006.

6. Taylor, C. F. and Toong, T. Y., "Heat Transfer in Internal Combustion Engines," *ASME*, 57-HT-17, 1957.

7. Nusselt, W., "Der Warmeubergang in der Verbrenungskraftmaschene," *Z. Verdt. Ing*., Vol. 67, pp. 692-708, 1923.

8. Eichelberg, G., "Some New Investigations on Old Combustion Engine Problems," *Engineering*, Vol. 148, pp. 463-446, 547-560, 1939.

9. Annad, W. J., "Heat Transfer in the Cylinder of Reciprocating Internal Engines," *Proc. Instn Mech. Engrs*, 36, Vol. 177, pp. 973-990, 1963.

10. Woschni, G. A., "A Universally Applicable Equation for the Instantaneous Heat Transfer Coefficient in the Internal Combustion Engine," *SAE*, 670931, 1967.

11. Woshni, G., "Die Berechnung der Wandverluste und der Thermischen Belatung der Bauteile von Dieselmotoren," *MTZ*, 12, Vol. 20, pp. 491-499, 1970.

12. Franco, A. and Martorano, L., "Evaluations on the Heat transfer in Small two Stroke Engines," *SAE*, 98762, 1998.

13. Schubert, C., Wimmer, A., and Chmela, F., "Advanced Heat transfer Model for CI Engines," *SAE*, 2005-01-0695, 2005.

14. LeFeuvre, T., Myers, P. S., and Uyehara, O. A., "Experimental Instantaneous Heat Fluxes in a Diesel Engine and Their Correlation," *SAE*, 690464, 1969.

15. Chang, J., Gurlap, O., Filipi, Z., Assanis, D., Kuo, T., Najt, P., and Rask, R., "New Heat transfer Correlation for an HCCI Engine Derived from Measurements of Instantaneous Surface Heat Flux," *SAE*, 2004-01-2996, 2004.

16. Kraiger, R. B., and Borman, G. L., "The Computation of Apparent Heat Release for Internal Combustion Engines," *ASME*, 66-WA/DGP-4, 1966.

17. Borgnakke, C., Arpaci, V. S., and Tabacsynski, R. J., "A Model for the Instantaneous Heat Transfer and Turbulence in a Spark Ignition Engine," *SAE*, 800287, 1980.

18. Payri, F., Margot, X., Gil, A., and Martin, J., "Computational Study of Heat Transfer to the Walls of a Diesel Engine," *SAE*, 2005-01-0210, 2005.

19. Fluent 6.2 User Guide, Fluent Inc., 2005.

20. Wilson, N. D., Watkins, A. J., and Dopson, C., "Asymmetric Valve Strategies and Their Effect on Combustion," *SAE*, 930821, 1993.

21. Hall, M. J., and Bracco, F. V., "Cycle-Resolved Velocity and Turbulence Measurements Near the Cyliner of a Firing S. I. Engine," *SAE*, 861530, 1986.

22. Fansler, T. D., "Turbulence Production and Relaxation in Bowel-in-Piston Engines," *SAE*, 930479, 1993.

23. Chung, T. J., *Computational Fluid Dynamics*, Cambridge: Cambridge University Press, 2002.

24. Davidson, P. A., *Turbulence: An Introduction for Scientists and Engineers*, Oxford: Oxford University Press, 2004.

25. Schlichting, H. and Gersten, K., *Boundary Layer Theory*, 8th Revised and Enlarged Edition. Berlin: Springer, 2003.

26. Pope, S. B., *Turbulent Flows*, Cambridge: Cambridge University Press, 2006.

27. Adrian, R., Christensen, K., and Liu, Z., "Analysis and Interpretation of Instantaneous Turbulent Velocity Fields," *Experiments in Fluids*, Vol. 29, pp. 275-290, 2000.

28. Kline, S. J., and Rbinson, S. K., "Quasi-Coherent Structures in the Turbulent Boundary Layer. Part I: Status Report on a Community-Wide Summary of the Data," *Proceedings of Zaric Memorial Conference*, pp. 200-217, 1989.

29. Chong, M., Perry, A. and Cantwell, B., "A General Classification of Three-Dimensional Flow Fields," *Physics of Fluids A*, Vol. 2, pp. 765-777, 1990.

30. Zhou, J., Adrian, R. and Balachandar, S., "Autogeneration of Near-Wall Vortical Stryctures in Channel Flow," *Physics of Fluids*, Vol. 8, pp. 288-290, 1996.

31. Zhou, J., Adrian, R., Balachandar, S., and Kendall, T., "Mechanisms for Generating Coherent Packets of Hairpin Vortices in Channel Flow," *Journal of Fluid Mechanics*, Vol. 387, pp. 353-396, 1999.

32. Flow Master Manual: 1003005_FlowMaster_D72.pdf, Gottingen: LaVision, 2007.

33. Yeh, Y., and Cummins, H. Z., "Localized Fluid Flow Measurements with a He-Ne Laser Spectrometer," *Applied Physics Letters*, 10, Vol. 4, pp. 176-178, 1964.

34. Johnston, S. C., Robinson, C. W., Rorke, W. S., Smith, J. R., and Witze. P. O., "Applications of Laser Diagnostics to an Injected Engine," *SAE*, 790092, 1979.

35. Barker, D. B., and Fourney, M. E., "Measuring Fluid Velocities with Speckle Patterns," *Optics Letters*, 4, Vol. 1, pp. 135-137, 1977.

36. Dudderar, T. D., and Simpkins, P. G., "Laser Speckle Photography in a Fluid Medium," *Nature*, 5632, Vol. 270, pp. 45-47, 1977.

37. Grousson, R., and Mallick, S., "Study of Flow Pattern in a Fluid by Scattered Laser Light," *Applied Optics*, 9, Vol. 16, pp. 2334-2336, 1977.

38. Meynart, R., "Instantaneous Velocity Field Measurements in Unsteady Gas Flow by Speckle Velocimetry," *Applied Optics*, 4, Vol. 22, pp. 535-540, 1983.

39. Pickering, C. J. D., and Halliwell, N. A., "Laser Speckle Photography and Particle Image Velocimetry: Photographic Film Noise," *Applied Optics*, 17, Vol. 23, pp. 2961-2969, 1984.

40. Adrian, R., "Scattering Particle Characteristics and Their Effect on Pulsed Laser Measurements of Fluid Flow: Speckle Velocimetry vs. Particle Image Velocimetry," *Applied Optics*, 11, Vol. 23, pp. 1690-1691, 1984.

41. Raffel, M., Willert, C., Wereley, S., and Kompenhans, J., *Particle Image Velocimetry: Apractical Guide*, 2nd ed., Berlin: Springer, 2007.

42. Reuss, D. L., Adrian, R. J., Landerth, C. C., French, D. T., and Fansler, T. D., "Instantaneous Planar Measurements of Velocity and Large-Scale Vorticity and Strain Rate in an Engine Using Particle Image Velocimetry," *SAE*, 890616, 1989.

43. Foster, D. F. and Witze, P. O., "Velocity Measurements in the Wall Boundary Layer of a Spark-Ignited Research Engine," *SAE*, 872105, 1987.

44. Pierce, P. H., Ghandhi, J. B., and Martin, J. K., "Near-Wall Velocity Characteristics in Valved and Ported Motored Engines," *SAE,* 920152, 1992.

45. Kline, S. J., Reynolds, W. C., Schraub, F. A., and Runstadler, P. W., "The Structure of Turbulent Boundary Layers," *Journal of Fluid Mechanics*, Vol. 30, pp. 741-773, 1967.

46. Costamagna, P., Vittori, G., and Bloneaux, P., "Coherent Structures in Oscillatory Boundary Layers," *Journal of Fluid Mechanics*, Vol. 474, pp. 1-33, doi: 10.1017/S0022112002002665, 2003.

47. Kearney, S. P., Jacobi, A. M., and Lucht, R. P., "Time_resolved Thermal Baoundary-Layer Structure in a Pulsatile Reversing Channel Flow," *ASME Journal of Heat Transfer*, Vol. 123, pp. 655-664, doi: 10.1115/1.1372317, 2001.

48. Keane, R. D., and Adrian, R. J., "Optimization of Particle Image Velocimeters. Part I: Double Pulsed Systems," *Measurement Science and Technology*, Vol. 1, pp. 1202-1215, 1990.

49. White, F. M., *Viscous Fluid Flow*, 3rd ed., New York: McGraw-Hill, 2006.

50. Cosadia, J., Boree, J., Charnay, G., and Dumont, P., "Cyclic Variation of the Swirling Flow in a Diesel Transparent Engine," *Experiments in Fluids*, Vol. 41, pp. 115-134, doi: 10.1007/s00348-006-0163-4, 2006.

51. Keane, R. D., and Adrian, R. J., "Optimization of Particle Image Velocimeters. Part II: Double Pulsed Systems," *Measurement Science and Technology*, Vol. 2, pp. 963-974, 1991.

52. Megerle, M., Sick, V., and Reuss, D. L., "Measurement of Digital Particle Image Velocimetry Precision Using Electro-Optically Created Particle-Image Displacements," *Measurement Science and Technology*, Vol. 13, pp. 997-1005, 2002.

53. Stanislas, M., Okamoto, K., Kahler, C. J., and Westerweel, J., "Main Results of the Second International PIV Challenge," *Experiments in Fluids*, Vol. 39, pp. 170-191, doi: 10.1007/s00348-005-0951-2, 2005.

54. Specialist Committee on Uncertainty, "Uncertainty Analysis: Particle Imaging Velocimetry," *25th ITCC-Recommended Procedures and Guidelines*, 7.5-01-03-03, 2008.

55. Luong, M., Zhang, R., Schulz, C., and Sick, V., "Toluene Laser-Induced Fluorescence for In-Cylinder Temperature Imaging in Internal Combustion Engines," *Applied Physics B*, Vol. 91, pp. 669-675, doi: 10.1007/s00340-008-2995-5, 2008.

56. Brübach, J., Zetterberg, J., Omrane, A., Li, Z. S., Alden, M., and Dreizler, A., "Determination of Surface Normal Temperature Gradients using Thermographic Phosphors and Filtered Rayleigh Scattering," *Applied Physics B*, Vol. 84, pp. 537-541, doi: 10.1007/s00340-006-2243-9, 2006.

57. Fajardo, C.M., Sick, V., "Development of a High-Speed UV Particle Image Velocimetry Technique and Application for Measurements in Internal Combustion Engines," *Experiments in Fluids*, Vol. 46, pp. 43-53, doi: 10.1007/s00348-008-0535-z, 2009.

58. Reuss, D. L., Megerle, M., and Sick, V., "Particle-Image Velocimetry Measurement Errors when Imaging Through a Transparent Engine Cylinder," *Measurement Science and Technology*, Vol. 13, pp. 1029-1035, pii: S0957-0233(02)31488-7, 2002.

59. Howell, S. B., *Handbook of CCD Astronomy*, Cambridge: Cambridge University Press, 2000.

60. Stitou, A., and Riethmuller, M. L., "Extension of PIV to Super Resolution using PTV," *Measurement Science and Technology*, Vol. 12, pp. 1398-1403, pii: S0957-0233(01)20955-2, 2001.

61. Fajardo, C. M., Sick, V., "Kinetic Energy and Dissipation Rate Spectra of High-and Low-Swirl Internal Combustion Engine Flows," *SAE*, 2009-01-0651, 2009.

62. Kim, J., Moin, P., and Moser, R., "Turbulence Statistics in Fully Developed Channel Flow at Low Reynolds Number," *Journal of Fluid Mechanics*, Vol. 177, pp. 133-166, 1987.

63. Spalart, P. R., "Direct Simulation of a Turbulent Boundary Layer up to Re = 1410," *Journal of Fluid Mechanics*, Vol. 187, pp. 61-98, 1988.